Coherent manipulation of single quantum systems in the solid state

A dissertation presented

by

Lilian Isabel Childress

to

The Department of Physics

in partial fulfillment of the requirements

for the degree of

Doctor of Philosophy

in the subject of

Physics

Harvard University

Cambridge, Massachusetts

March 2007

Thesis advisor

Mikhail D. Lukin

Author

Lilian Isabel Childress

Coherent manipulation of single quantum systems in the solid state

Abstract

The controlled, coherent manipulation of quantum-mechanical systems is an important challenge in modern science and engineering, with significant applications in quantum information science. Solid-state quantum systems such as electronic spins, nuclear spins, and superconducting islands are among the most promising candidates for realization of quantum bits (qubits). However, in contrast to isolated atomic systems, these solid-state qubits couple to a complex environment which often results in rapid loss of coherence, and, in general, is difficult to understand. Additionally, the strong interactions which make solid-state quantum systems attractive can typically only occur between neighboring systems, leading to difficulties in coupling arbitrary pairs of quantum bits.

This thesis presents experimental progress in understanding and controlling the complex environment of a solid-state quantum bit, and theoretical techniques for extending the distance over which certain quantum bits can interact coherently. Coherent manipulation of an individual electron spin associated with a nitrogen-vacancy center in diamond is used to gain insight into its mesoscopic environment. Furthermore, techniques for exploiting coherent interactions between the electron spin and a subset of the environment are developed and demonstrated, leading to controlled

interactions with single isolated nuclear spins. The quantum register thus formed by a coupled electron and nuclear spin provides the basis for a theoretical proposal for fault-tolerant long-distance quantum communication with minimal physical resource requirements. Finally, we consider a mechanism for long-distance coupling between quantum dots based on chip-scale cavity quantum electrodynamics.

Contents

Citations to Previously Published Work

A portion of Chapter 2 and most of Chapter 3 have appeared in the following paper and its supplementary online material:

> "Coherent dynamics of coupled electron and nuclear spin qubits in diamond", L. Childress, M.V.G. Dutt, J.M. Taylor, A.S. Zibrov, F. Jelezko, J. Wrachtrup, P.R. Hemmer, and MD Lukin, Science **314**, 281 (2006).

Chapter 5 has been slightly modified from results published in the following two papers:

> "Fault-tolerant quantum repeaters with minimal physical resources and implementations based on single-photon emitters", L. Childress, J.M. Taylor, A.S. Sørensen, and M.D. Lukin, Phys. Rev. A **72**, 052330 (2005)

> "Fault-tolerant quantum communication based on solid-state photon emitters", L. Childress, J.M. Taylor, A.S. Sørensen, and M.D. Lukin, Phys. Rev. Lett. **96**, 070504 (2006).

Chapter 6 has been published with minor changes as

> "Mesoscopic cavity quantum electrodynamics with quantum dots ", L. Childress, A.S. Sørensen, and M.D. Lukin, Phys. Rev. A **69**, 042302 (2004).

Acknowledgments

Graduate school has been tremendously challenging, demoralizing, exciting, and exhausting, and I have gotten through it only thanks to the support of my family, friends, advisor, and co-workers.

My family deserves first mention, having supported and comforted me through innumerable difficulties. My father has become familiar with the Chinatown bus schedule and even spent several days working in the corner of my lab keeping me company, while my mother occupied the desk next to mine for a week while I thrashed out the final version of our Science paper. My sister Lucy has encouraged me throughout.

I have been blessed with a remarkably understanding advisor, Misha Lukin, who gave me the freedom to pursue a variety of different projects, and encouraged me to think independently. Misha's long-time collaborator Sasha Zibrov has also been a wonderful influence, teaching me experimental tricks and Russian phrases with equal charm.

There are several other faculty members both at Harvard and elsewhere who have helped me pursue my studies. John Doyle generously gave us enough space in his laboratory to build the experiment which forms the bulk of this thesis. Phil Hemmer, from Texas A & M, assisted with every stage of the experiments, and gave us the knowledge we needed to start a research project in a new field. Fedor Jelezko, from Stuttgart University, shared the techniques he pioneered and helped us get our experiment running. I worked with Charlie Marcus for six months, and he has continued to take an interest in my research and well-being, as has Ron Walsworth. Finally, I would like to thank the members of my thesis committee, Misha Lukin, John Doyle, and Federico Capasso.

I have many friends and collaborators in the Harvard physics department whose advice and support have been invaluable. I would have left graduate school after my first year were it not for Stan Cotreau, who manages the student machine shop. He and several other staff members, especially Sheila Ferguson and Vickie Greene, made the physics department a welcoming environment. I have been lucky to work with many wonderful graduate students and postdocs, including Naomi Ginsberg, Heather Lynch, Leo DiCarlo, Matt Eisaman, Jake Taylor, Anders Sørensen, Gurudev Dutt, Aryesh Mukherjee, Emre Togan, Jero Maze, and Liang Jiang. My time here would not have been the same without my mid-day running-climbing-swimming-biking-drinking buddies Wes Campbell, Steve Maxwell, Dave Morin, and Dave Patterson, and my roommates, Naomi Ginsberg, Elissa Klinger, and Trygve Ristroph.

I have benefited from many scientific collaborations, which varied between the different projects which compose this thesis. The experimental work on the NV center was aided by collaboration with several scientists, most notably Dr. M.V. Gurudev Dutt, who shared equally in design, construction, and execution of the experiments, and Prof. M.D. Lukin, who guided our progress. These results would have been impossible without the generosity of Prof. John Doyle, who gave us space to conduct them in his laboratory. We also greatly benefited from the assistance of Prof. Philip Hemmer, Dr. Fedor Jelezko, Dr. Alexander Zibrov, and Prof. Jeorg Wrachtrup. Aryesh Mukherjee was responsible for isolation of single NV centers, and Emre Togan helped considerably with the material presented in Chapter 4, including writing much of our control software. Finally, our experimental efforts were complemented by theoretical work performed by Dr. Jacob Taylor, Liang Jiang, Jeronimo Maze, and

Amy Peng. The theoretical proposal for a realistic fault-tolerant quantum repeater was the result of a collaboration with Dr. Anders Sørensen, Prof. Mikhail Lukin, and Dr. Jacob Taylor. The theoretical investigation of CQED with quantum dots was conducted in collaboration with Dr. Anders Sørensen and Prof. Mikhail Lukin. My intuition for the system was also enhanced by my experience working with Heather Lynch and Leonardo DiCarlo on experiments with double quantum dots conducted in Prof. Charles Marcus' laboratory.

Dedicated to my parents Diana and Steve

Chapter 1

Introduction

1.1 Control of quantum systems

Control of quantum systems is an important topic in contemporary physics research, with many types of experiments aimed at applications ranging from metrology [1] to interferometry [2] to quantum computation [3, 4]. A variety of physical systems lend themselves to such investigations, and each offers a different set of opportunities and challenges. This thesis addresses several ways in which ideas developed in the context of atomic systems find application in the coherent manipulation of single solid state quantum systems.

1.1.1 Atomic systems

The internal electronic levels of neutral atoms and ions present a natural set of quantum states because their properties and interactions with the environment (typically formed by the vacuum modes of the radiation field) are generally well un-

derstood [5, 6]. The internal states can be manipulated using optical or microwave transitions. Owing to their weak interactions with the environment, different hyperfine states can exhibit extremely long coherence times (in excess of a few seconds [7]).

To control the quantum state of an atom, one must confine the atomic system and isolate its internal levels from its motional states; this presents one of the primary challenges in working with atoms and ions. Many approaches to this problem exist. For example, laser cooling and trapping of atoms [8, 9, 10] can be used to prepare an atom in its motional ground state [11]. By working with charged ions, one can use Coulomb repulsion to construct strong trapping potentials, and cool the ion using sideband transitions [12, 13]. Additionally, one can find ways to manipulate the internal states of atoms and ions independent of the motional state [14, 15]. For example, Doppler-free transitions between two collective states of an atomic ensemble allow coherent phenomena to be observed in room-temperature atomic systems [16]. The motional states of atoms and ions can thus be controlled or decoupled using a variety of techniques.

Because atoms interact so weakly with their surroundings, it can be difficult to realize strong, controllable interactions between atomic systems. The coupled motional states of several ions confined to a single trap provide an elegant means to engineer strong interactions [13], allowing remarkable progress in quantum manipulation of systems of several trapped ions [13, 17, 18, 19, 20, 21]. In the case of neutral atoms, many tricks and techniques have been explored to solve this problem of weak interactions, for example using the large dipole moment of Rydberg atoms [22, 23].

One means of controlling interactions between isolated atomic systems uses quan-

tum states of photons as an intermediary [24]. This approach allows interactions over very long distances, but requires finding a way to make each atomic system interact strongly with a single photon. By putting an atom in a high finesse, low volume cavity, its interaction with the cavity mode can be greatly enhanced, so that deterministic interactions between single atoms and single photons occur. This technique is known as cavity quantum electrodynamics (CQED), and has been extensively explored using photons in both the optical [25, 26] and microwave regime [27, 28]. Alternately, atomic ensembles can interact strongly with single photons via collective enhancement [29, 30].

Another approach to photon-mediated interactions gets rid of the requirement that each atomic system fully absorb an incoming photon. Instead, the interaction occurs probabilistically, using spontaneous emission to entangle atomic states with a photon, photon interference to couple two spontaneously emitting atoms, and photon measurement to introduce a nonlinearity in the interaction [31, 32]. Coupling each atom to a single photon thereby takes place through spontaneous emission instead of deterministic absorption. This technique is now being explored using atoms and ions [33, 30, 34, 35, 36], and could potentially be applied to any other system which exhibits radiatively broadened transitions and internal-state-dependent spontaneous photon emission. In particular, it plays an important role in a recent proposal for a quantum repeater based on atomic ensembles [32] and other quantum information processing schemes [37, 38, 39].

1.1.2 Solid-state systems

With such remarkable advances in quantum control of atomic systems, it may seem unnecessary to attempt similar experiments in the solid state. However, solid state devices offer both fundamental and practical advantages over some aspects of atomic systems. Fundamentally, solid state systems typically exhibit strong interactions because they can be located in close proximity to each other. Practically, their motional states are easier to control, leading to much simpler experiments which might be feasible to scale to larger numbers of quantum systems. Additionally, modern fabrication techniques enable design of the desired system, so that solid-state systems can be described by varied or tunable parameters [40, 41] and monolithically integrated with other systems such as cavities and resonators [42, 43] or classical circuitry.

Many of the ideas developed in the context of quantum control of atoms and ions carry over into solid-state systems. For example, many solid-state systems can be coupled to photons in a manner analogous to atoms, often with large dipole moments arising from the extended nature of the solid-state system [44, 42]. By integrating cavity construction with device fabrication, solid state systems have proven quite amenable to CQED experiments in both the optical [45] and microwave [43] regime. This thesis includes a theoretical proposal for solid-state CQED using quantum dots which could be used to observe maser-type phenomena on a chip. Integrated cavity design can also enhance the bit rates for probabilistic entanglement schemes modelled on probabilistic interactions between atomic systems [32], and Chapter 5 discusses how these ideas could be used to construct a solid-state quantum repeater.

The primary disadvantage of working with solid-state systems is that they typ-

ically couple strongly to a complex environment. As a consequence, the behaviour of each system will vary depending on its immediate environment; unlike atoms, two versions of the same solid-state system are not identical. More importantly, coherence times for solid-state systems are generally short, ranging from the ns scale [46] for charging states of double dots to μs for electron spin states [47, 48] to many seconds for weakly coupled nuclear spins treated with active dipolar decoupling techniques [49, 50]. In some cases, however, the surrounding environment can be viewed as a resource [51], or an interesting system in its own right [52, 53, 54]. A controllable quantum system can then be used as a coherent probe of the complex solid-state environment.

We take this approach in our study of the nitrogen-vacancy (NV) center in diamond. The NV center can be viewed as an "atom-like" solid state system, in that it has optical transitions which allow preparation and measurement of its ground state multiplet, and long coherence times $\sim 100\mu$s within the ground state multiplet. However, it couples to an environment dominated not by the vacuum modes of the radiation field but by the bath of ^{13}C nuclear spins randomly scattered through the diamond lattice. This environment behaves very differently from the Markovian environments typical of isolated atoms [5], exhibiting a long memory time and even coherent interactions between the NV center and a subset of the environment. By studying the mesoscopic environment of the NV center in detail, we are able to probe a single nuclear spin in the bath, in effect moving it from the undesirable environment into part of a controllable system.

1.2 Overview and structure

This thesis comprises three projects related to control of solid-state quantum systems. The first three chapters describe a set of experiments performed on the nitrogen-vacancy (NV) center in diamond. The next chapter presents a scheme for long-distance quantum communication which could be realized using the NV center. The final chapter discusses a proposal for CQED using gate-defined quantum dots coupled to a microwave resonator.

1.2.1 The nitrogen-vacancy center in diamond

Chapters 2-4 are devoted to experimental investigations of the NV center in diamond. Chapter 2 introduces the structure and properties of the NV center, and discusses the basic experimental techniques used to isolate and manipulate the electronic spin associated with single NV centers. Spin-echo spectroscopy of the NV electron spin is presented in Chapter 3, along with a detailed theory which explains the observed spin-echo modulation phenomena in terms of ^{13}C nuclear spins in the environment. In particular, we show that the electron spin couples coherently to individual, isolated ^{13}C spins in the bath. In Chapter 4, we use this coherent coupling to study a single nuclear spin. We investigate coherence properties of the nuclear spin, and show that the nuclear spin can be used as a quantum memory for electron spin states.

1.2.2 Future applications: long distance quantum communication

The coupled electron-nuclear spin system described in Chapter 4 forms a possible physical basis for a scheme for long-distance quantum communication presented in Chapter 5. Current quantum cryptography protocols are limited by the range over which single photons can be transmitted without significant attenuation [55]. Quantum cryptography can be extended to longer distances by means of a quantum repeater [56]. Chapter 5 describes a scheme which incorporates probabilistic entanglement generation [32] and error purification [57] to construct a fault-tolerant quantum repeater which has a minimal set of requirements on physical resources. The reduced physical resource requirements allow identification of several systems in which such a quantum repeater could be realized.

1.2.3 Cavity QED with double quantum dots

Chapter 6 describes a theoretical proposal for coupling double quantum dots via a superconducting stripline resonator. Although solid-state devices can couple strongly to nearest-neighbor systems [58], it can be difficult to design strong interactions between solid-state systems separated by macroscopic distances. Using CQED ideas developed in the context of atomic physics [27], we show that the solid-state analog of a microwave CQED system can be implemented on a chip using the charge or spin states of a double quantum dot as the atomic system and a lithographically defined microwave resonator as the cavity. Such a system could allow quantum dots to interact with each other over distances set by the microwave wavelength $\sim$ cm.

Recently, a similar system has been realized experimentally using the charge states of a superconducting Cooper pair box [43]. Our work on quantum dots, together with several recent proposals for coupling atomic and molecular systems to a microwave stripling [59, 60], points towards development of superconducting microwave resonators as a quantum data bus which could connect distinct quantum systems.

Chapter 2

Optical and spin spectroscopy of nitrogen-vacancy centers in diamond

2.1 Introduction

The nitrogen-vacancy (NV) center in diamond has been studied for many decades using a variety of techniques. Recently, there has been renewed interest in the NV center as a physical system for quantum information science in the solid state. The NV center is an attractive qubit candidate because it behaves a bit like an atom trapped in the diamond lattice: it has strong optical transitions, and an electron spin degree of freedom. In this chapter, we consider the basic structure of the NV center and present experimental techniques used to probe its spin and optical transitions.

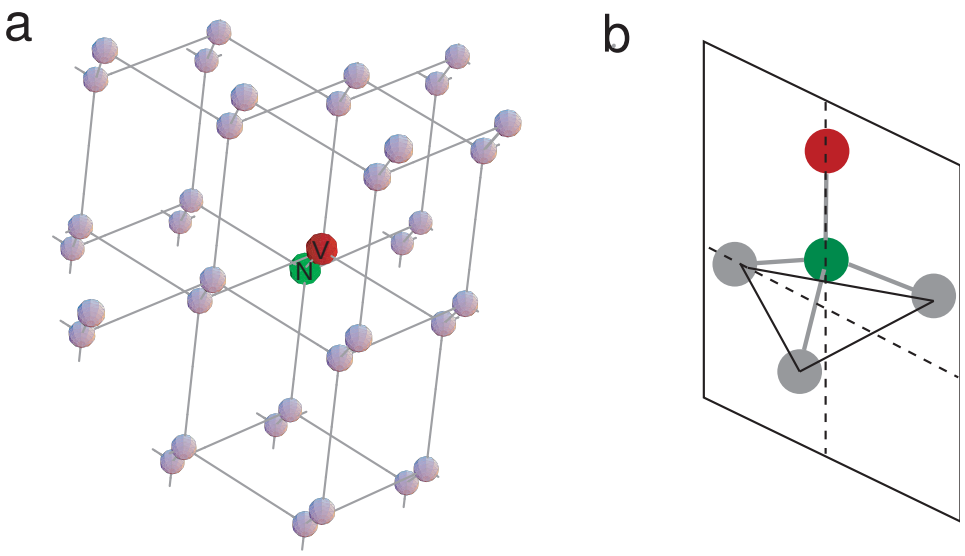

Figure 2.1: *(A) The nitrogen-vacancy center in diamond. (B) The symmetry operations for the C_{3v} group include rotations by $2\pi n/3$ around the vertical symmetry axis and reflections in the three planes containing the vertical symmetry axis and one of the nearest-neighbor carbon sites.*

2.2 The structure of the NV center

2.2.1 Physical structure

The NV center is formed by a missing carbon atom adjacent to a substitutional nitrogen impurity in the face-centered cubic (fcc) diamond lattice (see Fig. 2.1A). The physical structure of this defect – and the symmetries associated with it – determine the nature of its electronic states and the dipole-allowed transitions between them.

The symmetry properties of the NV center provide insight into the nature of its electronic states. Unlike atoms in free space, whose electronic states are governed by their rotational invariance, the NV center exhibits C_{3v} symmetry, as illustrated in Fig. 2.1B. Electronic states are thus characterized by how they transform under C_{3v} operations. A_1 energy levels consist of a single state which transforms into itself, with

no sign change, under all symmetry operations. A_2 levels are also non-degenerate, but the state picks up a negative sign under reflections. Finally, E levels consist of a pair of states, which transform into each other the way that the vectors $\hat{x}$ and $\hat{y}$ transform into each other under C_{3v} symmetry operations. For more details on C_{3v} symmetry and group theory, see Appendix A.

2.2.2 Electronic structure

Although a number of efforts have been made to elucidate the electronic structure of the NV center from first principles [61, 62, 63], it remains a topic of current research. Experimentally, it has been established that the NV center exists in two charge states, NV^0 and NV^-, with the neutral state exhibiting a zero-phonon line (ZPL) at 575nm [64] and the singly charged state at 637nm (1.945 eV) [65, 66]. In this work we consider exclusively NV^-, which is dominant in natural diamond, and will refer to it simply as the NV center. The extra negative charge adds to the five electrons associated with the three dangling carbon bonds and two valence electrons from the nitrogen, so that there are six electrons associated with the NV center.

Several experiments have established some facts about the NV center electronic structure. Uniaxial stress measurements [67] have determined that the NV center has C_{3v} symmetry, with the ZPL emission band associated with an A to E dipole transition. Hole-burning [68], electron spin resonance (ESR) [69, 70], optically detected magnetic resonance (ODMR) [71], and Raman heterodyne [72] experiments have established that the ground electronic state is a spin triplet $^3A_2$. This triplet is itself split by spin-spin interactions, yielding one S_z or $m_s = 0$ state with A_1 character and

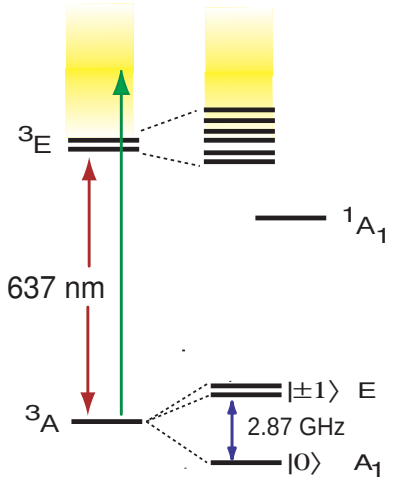

Figure 2.2: *The electronic structure of the NV center. The orbital states are indicated on the left hand side, and the spin-spin splitting of the ground state is indicated on the right hand side. After accounting for all spin-orbit, spin-spin, and strain perturbations, the structure of the six electronic excited states remains a topic of current research. Vibronic sideband transitions used in excitation are indicated by the yellow continuum.*

two $\{S_x, S_y\}$ or $m_s = \pm 1$ states with E character [63] which are 2.87 GHz higher in energy. Together with the 637nm ZPL, the 2.87 GHz zero-field ground-state splitting allows identification of a defect in diamond as an NV center.

The $S = 1$ ground state structure has been well established by many experiments, but the excited state structure is just beginning to be understood. Since the ZPL is associated with a $^3A_2$ to ^3E transition, there are six excited states which must be treated, corresponding to an $m_s = 0$ E level, and three levels A_1, A_2, and E with spin $m_s = \pm 1$ [63]. Additional perturbations, such as strain fields, may further shift and mix the levels. Furthermore, a metastable spin singlet A_1 state is postulated to play an important role in the dynamics of the NV center under optical illumination [73] (see Fig. 2.2).

In addition to the discrete electronic excited states which contribute to the ZPL,

there are a continuum of vibronic excited states which appear at higher frequencies in absorption and lower frequencies in emission. When the vibronic states are excited using above-band excitation (for example a 532nm laser), phonon relaxation brings the NV center quickly into one of the electronic excited states. The NV center then fluoresces primarily into the phonon sideband, which extends from 650-800nm. Even at low temperature, fluorescence into the ZPL accounts for only a few percent of the emitted light [74].

2.3 Confocal microscopy of NV centers

Many of the early experiments on NV centers looked at ensemble properties, averaging over orientation, strain, and other inhomogeneities. Recently, confocal microscopy techniques have enabled examination of single NV centers [75], permitting a variety of new experiments studying photon correlation statistics [76, 77], single optical transitions [78], coupling to nearby spins [79], and other effects difficult or impossible to observe in ensemble studies.

2.3.1 Experimental apparatus

To study NV centers in diamond, we have constructed a scanning confocal microscope incorporating magnetic field control and microwave coupling. The essential features of the apparatus are shown in Fig. 2.3.

The sample we use is a type IIa diamond specially selected for low nitrogen content ($\ll$ 1ppm). This low nitrogen content is critical for observing coherent processes of the NV spin degree of freedom, because the electron spin associated with nitrogen

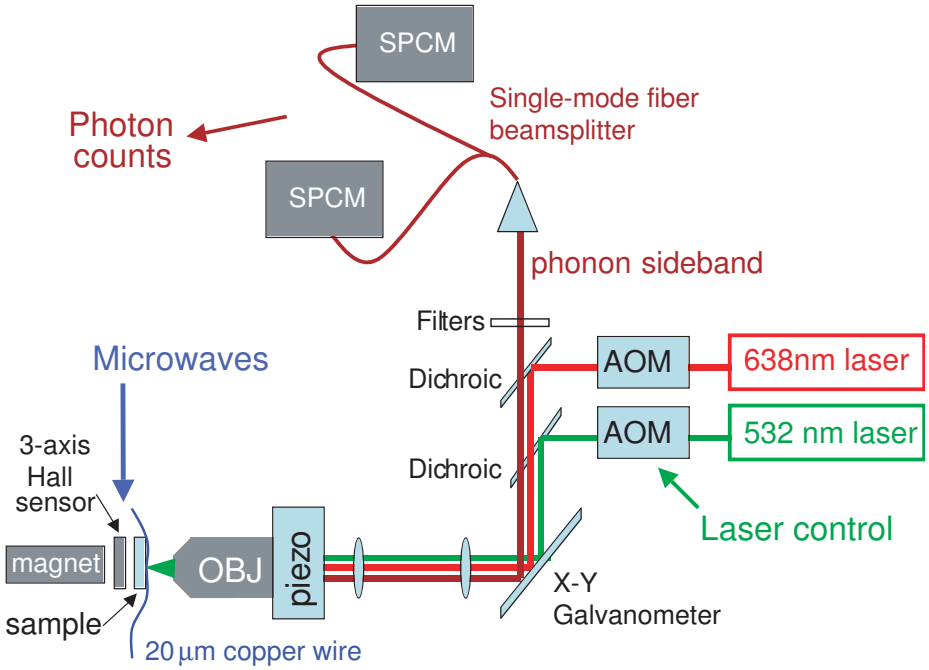

Figure 2.3: *Diagram of the experimental setup.*

donors interacts strongly with the NV center spin [80]. The sample has not been irradiated or annealed, so the NV centers we observe occur naturally.

Our measurements rely on optically exciting a single NV within the sample, and detecting its fluorescence. Excitation into the vibronic sideband of the NV center is performed using a 532nm doubled-YAG laser (Coherent Compass 315), while resonant excitation of the ZPL is achieved with a 637nm external cavity diode laser (Toptica DLL100) . The excitation beams pass through fast AOMs (rise time $\sim$ 25 ns), allowing pulsed excitation with widths of less than 100ns, and are focussed onto the sample with an oil immersion lens (Nikon Plan Fluor 100x N.A. 1.3).

To control the position of the focal spot on the sample we employ a closed-loop X-Y galvanometer (Cambridge Technology) combined with a piezo objective mount

(Physik Instrument PIFOC, open-loop) for focus adjustment. The mirrors forming the galvanometer are imaged onto the back of the objective, so that they vary the position of the focal spot without affecting the transmitted laser power. Scanning the galvanometer mirrors thus allows us to scan the focal spot over a plane in the sample, with a maximum scan range of approximation 100x100 μm.

Fluorescence from an NV center is collected by the same optical train, so that the detection spot is scanned along with the excitation spot. The fluorescence into the phonon sideband (650-800nm) passes through the dichroic mirrors (which combine the excitation lasers with the optical train), and a series of filters (532nm notch, 638nm notch, 650 long-pass) before being coupled into a single-mode fiber. In many confocal setups, the point source emission is imaged onto a pinhole for background rejection; in our setup, the single-mode fiber replaces the pinhole. Ideally, this constitutes mode-matching between the mode collected by the objective from the NV center point source and the mode of the fiber. The fiber is itself a beamsplitter, whose two outputs are connected to fiber-coupled single photon counting modules (SPCMs, Perkin-Elmer). Overall, the collection efficiency for fluorescence from the sample is just under 1%.

To apply strong microwaves to the NV center, the sample is mounted on a circuit board with a microwave stripline leading to and away from it. A 20 μm copper wire placed over the sample is soldered to the striplines. By looking at NV centers within $\sim 10\mu$m of the wire, we can achieve large amplitudes for the oscillating magnetic field without sending very much microwave power through the wire. Experimentally, we observe field strengths of order ~ 5 Gauss at 2.87 GHz using 1 Watt of power.

A static applied magnetic field can be varied using a permanent magnet mounted on a three axis translational stage and a rotational stage behind the sample. To measure the magnetic field, a three-axis Hall sensor (GMW) is mounted approximately one millimeter from the sample. In addition, the NV center itself can be used as a magnetometer to measure the $\hat{z}$ component of the magnetic field, since its g-factor has been measured in other experiments [81]. We find a $\sim 10\%$ discrepancy between the sensor reading and the B_z value inferred from spectroscopy which most likely arises from spatial variation in the magnetic field between the sensor and the sample.

2.3.2 Isolation of single NV centers

The small excitation and detection volume of our confocal microscope, combined with the low concentration of NV centers in the sample, allows us to image single NV centers. Scanning the focal spot of the microscope over the sample reveals scattered bright spots of similar intensity (see Fig. 2.4A). To verify that these are single quantum emitters, we position the focus on top of one of the bright spots and examine the photon statistics of its fluorescence.

Whereas thermal or coherent sources emit a distribution of photon numbers, a single quantum emitter is incapable of producing more than one photon at a time. In principle, one could observe this effect by histogramming the time interval between different photons, and examining the distribution close to zero delay. If the source was a single quantum emitter, the probability for a delay τ between successive photons should vanish as $\tau \to 0$.

Owing to dead-time effects for avalanche photodetectors, such as the SPCMs we

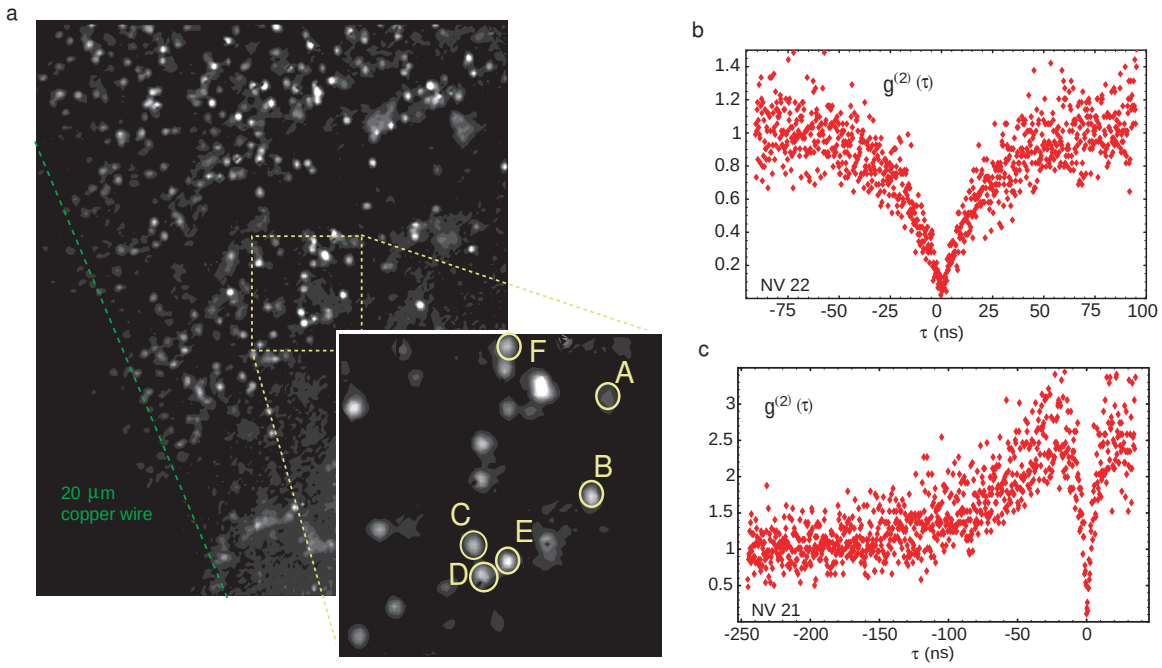

Figure 2.4: *(A) A scanning confocal microscope image of the sample, with a closeup of the sample region most closely studied. The green dashed line indicates the edge of the 20 µm copper wire used to deliver microwaves to the sample. (B) Second order photon correlation function for a single NV center under weak green illumination. The photon antibunching at delay $\tau = 0$ has $g^{(2)}(0) < 1/2$, indicating that we are observing a single NV center. (C) $g^{(2)}(\tau)$ under strong green illumination (for a different NV center). Note that the antibunching feature is surrounded on either sides by photon bunching, most likely from shelving in the metastable A_1 electronic state [73, 82, 83, 84].*

use, it is necessary to divide the emitted photons between two detectors, and measure the time interval τ between a click in one detector and a click in the second detector. In the limit of low count rates, this measurement yields the probability of measuring a photon at time τ conditional on detection of a photon at time 0, which corresponds to a two-time expectation value for the fluorescence intensity, $\langle I(\tau)I(0)\rangle$. Normalizing this quantity to the overall intensity $\langle I\rangle$ yields the second order correlation function

for a stationary process

$$g^{(2)}(\tau) = \frac{\langle I(\tau)I(0)\rangle}{|\langle I\rangle|^2}. \tag{2.1}$$

Ideally, we should observe $g^{(2)}(0) = 0$ for emission from a single quantum emitter, whereas classical sources must have $g^{(2)}(0) \geq 1$. Since a two-photon state has $g^{(2)} = 1/2$, observation of $g^{(2)}(0) < 1/2$ is sufficient to show that the photons are emitted one at a time by a single quantum system. In fact, the NV center has received considerable attention as a single photon source [76, 77, 85, 86] for quantum key distribution and other applications.

2.3.3 Optical spectra

The fluorescence and excitation spectra of the NV center are strongly influenced by the presence of phonons in the diamond crystal lattice. To investigate the optical properties of the NV center, it is important to cool the sample. For these low temperature experiments, the sample is mounted on the cold finger of a helium flow cryostat (Oxford Instruments, home-built cold finger and OVC) with a base temperature of 3.2K. The sample itself reaches a temperature between 6-10K depending on the design of the sample mount.

The fluorescence spectrum of an ensemble of NV centers has been observed at low temperatures (see Fig. 2.5A), and exhibits a sharp ZPL at 637nm with a broad phonon sideband, as expected from published observations [87]. The observed width of the inhomogeneously broadened ZPL is ~ 0.3 nm.

Within this inhomogeneous distribution, each NV center has a homogeneous linewidth associated with its optical transitions. We can measure this linewidth by

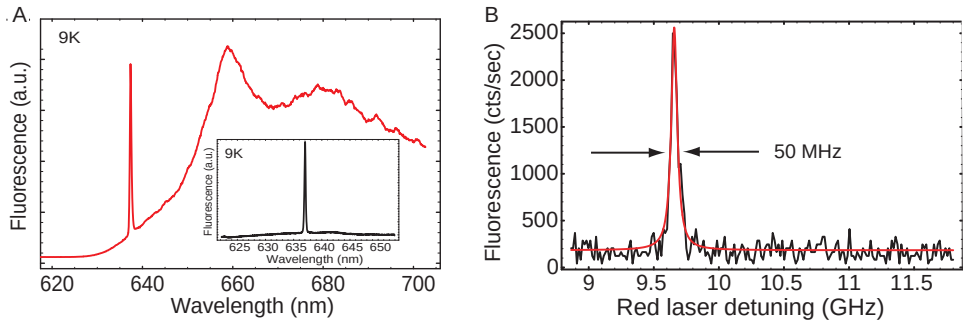

Figure 2.5: *(A) Fluorescence spectrum from bulk diamond containing NV centers at low temperature (9K). Inset shows a zoom in of the ZPL. (B)Fluorescence into the phonon sideband as a function of excitation frequency near 637.1 nm for a single NV center at low temperature ($\sim$ 6 K). The optical line is stable and exhibits a FWHM linewidth of 50 MHz.*

resonantly exciting a single NV center, and detecting the amount of fluorescence into the phonon sideband as a function of the excitation frequency. In between laser scans, we repump the NV center with 532nm light; this step appears to stabilize the optical transition frequency. Typically, we observe a single transition associated with each NV center, and its stability and linewidth vary between centers. Narrow, stable lines with homogeneous linewidths down to $\sim$ 50 MHz have been observed (see Fig. 2.5B). The natural lifetime of the NV center is $\approx$ 12 ns [88], corresponding to a radiatively broadened line with a 15 MHz width, so our measurements indicate that some NV centers can exhibit optical transitions which are about three times broader than the radiative linewidth. Recently, another group has observed radiatively broadened lines in certain samples at low (T = 1.8K) temperature [78].

We have also performed some preliminary spectroscopy of the optical transitions by combining resonant optical excitation with microwave excitation of the ground state spin transition. In the absence of microwaves, we see single, sharp lines from individual NV centers. Upon application of resonant microwaves, some NV centers

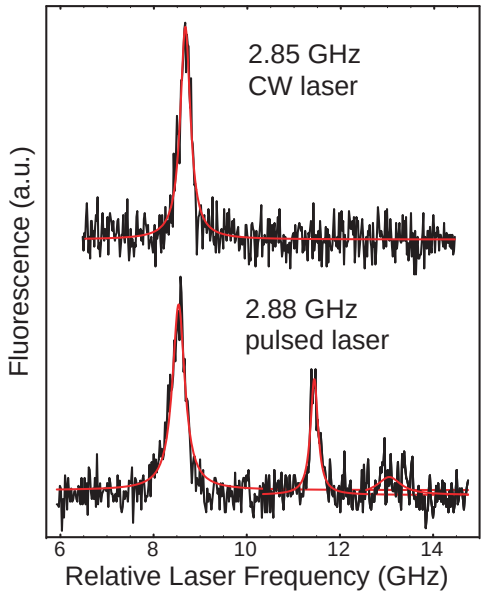

Figure 2.6: *Resonant optical and microwave excitation. The upper trace shows a the sideband fluorescence from a single NV center using continuous-wave resonant laser excitation and off-resonant microwave excitation. Under resonant microwave excitation, additional transitions become visible.*

show additional lines a few GHz from the original line. The splittings between the lines varied between NV centers without clear evidence of a pattern. We found that the secondary lines in the spectra became more intense if we alternated red and green optical excitation on a $\sim$ 200ns timescale. Sample traces with and without resonant microwave excitation are shown in Fig. 2.6.

These observations are consistent with the existence of a single, dominant S_z cycling transition augmented by other optical transitions which quickly cross over into the singlet state. By applying resonant microwaves, we shift some of the $m_s = 0$ population into $m_s = 1$, allowing us to see optical transitions for other spin states. Pulsing the laser limits our observation time to short times thereafter, when the system is less likely to have crossed into the A_1 singlet state. Our early experiments

were limited by low collection efficiency and mechanical instability, and we plan to pursue this spectroscopy in greater detail in a new cryostat with integrated optics.

2.4 Spin properties of optical transitions in the NV center

While discussing the electronic structure of the NV center, we have already touched upon the existence of a $S = 1$ spin degree of freedom in the ground and excited states. In this section, we will consider in greater detail the interplay between optical transitions and the spin degree of freedom.

Optically induced spin polarization

Early experiments [89] established that the NV center spin shows a finite polarization under optical illlumination. Over the years, it has been determined that optical excitation causes the ground $m_s = 0$ state to become occupied with $> 80\%$ probability [87, 90, 91], and recent data indicates that full polarization may occur [48]. Nevertheless, the precise mechanism for optically induced spin polarization remains a subject of controversy [63, 92].

Current models for spin polarization invoke the existence of a singlet electronic state whose energy level lies between the ground and excited state triplets (see Fig. 2.7). Transitions into this singlet state occur primarily from $m_s = \pm 1$ states, whereas decay from the singlet leads primarily to the $m_s = 0$ ground state [1]. If

[1] There is some disagreement in the literature over how population is transferred out of the singlet. Early models suggested that thermal repopulation of the excited triplet states played a role [73] or

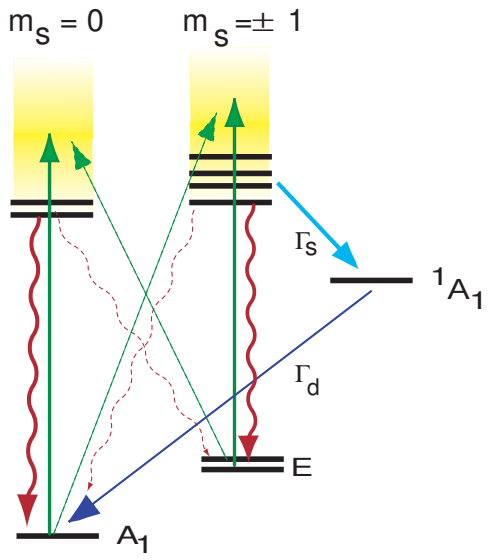

Figure 2.7: *A model used to explain optical spin polarization in the NV center [63, 92]. States on the left hand side have spin projection $m_s = 0$ (S_z states) whereas those on the right side have $m_s = \pm 1$ (S_x, S_y states). Solid arrows indicate strongly allowed transitions, whereas dotted arrows indicate weak or forbidden transitions. Γ_s is the intersystem crossing rate into the singlet $^1A_1$, which occurs primarily from $m_s = \pm 1$ states. Γ_d is the rate of nonradiative decay from the singlet state, which occurs primarily into the $m_s = 0$ state.*

the remaining optical transitions are spin-preserving, this mechanism should fully polarize the NV center into the $m_s = 0$ ground state. Simulations based on this model are discussed in Appendix B, and they provide a reasonable agreement with our experimental data.

Although the NV center optical transitions appear to be mostly spin-conserving [92], the detailed selection rules are a topic of current research. Resonant excitation of a stable optical line [87] indicates that there is an $m_s = 0$ optical transition where

that decay into the $m_s = \pm 1$ ground states can occur [84]. The model presented here is based on the most recent explanation [63], which provides an adequate explanation of our observations. According to this model, transitions between the triplet and singlet states occur via the spin-orbit interaction [63], which mixes states of the same irreducible representation. The excited state intersystem crossing favors the $m_s = \pm 1$ states because (in the absence of strain) there is an A_1 excited state with S_x, S_y character. Conversely, the decay from the singlet leads to the A_1 ground state, which has spin projection $m_s = 0$.

$\sim 10^5$ optical cycles can occur before the spin flips. Hole-burning spectra [68], however, show features at the ground state splitting (2.88 GHz) that are a signature of lambda transitions. Recent studies of coherent population trapping [93, 94] and Stark shifts [78] indicate that local strain fields in diamond can mix the excited state spin projections, leading to optical transitions that do not preserve spin. On the whole, a picture of the NV center is emerging in which some of the optical transitions preserve spin, while (depending on the degree of strain in the crystal) others do not.

Spin-dependent fluorescence

Most current research on the NV center in diamond relies on optical detection of its ground state spin. Experimentally, an NV center prepared in the $m_s = 0$ state fluoresces more strongly than an NV center prepared in the $m_s = 1$ state [75] [2]. At room temperature, this allows for efficient detection of the average spin population; using resonant excitation at low temperature, the effect is more pronounced, and single-shot readout is possible [87].

At room temperature, the same mechanism which leads to optical spin polarization provides the means to optically detect the spin state. Non-resonant excitation (at e.g. 532 nm) excites both the $m_s = 0$ and $m_s = \pm 1$ optical transitions. However, because the intersystem crossing occurs primarily from the $m_s = \pm 1$ excited state, population in $m_s = \pm 1$ ground state undergoes fewer fluorescence cycles before shelving in the singlet state. The $m_s = \pm 1$ states thus fluoresce less than the $m_s = 0$ state, with a difference in initial fluorescence of $\sim 20 - 40\%$[75, 63, 96]. Under continued optical

[2] Optically detected magnetic resonance in the NV center was observed first at low temperature in ensemble studies [71, 95]

illumination, the spin eventually polarizes into the $m_s = 0$ state, so the effect is transient.

At low temperature, a slightly different mechanism is used: the excitation laser is tuned into resonance with an $m_s = 0$ cycling transition, so that the center will only fluoresce if it is in the $m_s = 0$ state. The upper $m_s = 0$ transition can cycle $\sim 10^5$ times before flipping spin or crossing over into the shelving state, permitting single-shot readout with 95% fidelity [92].

It is worth noting that the $20\% - 40\%$ contrast in room-temperature optically detected magnetic resonance (ODMR) experiments arises from a combination of imperfect polarization and imperfect readout. The finite contrast can be treated as a calibration of the measurement technique only if one assumes that the polarization step is perfect. Imperfection in spin polarization expected from current models is discussed in Appendix B.

2.5 Single spin magnetic resonance

The electron spin of an NV center can be polarized and measured using optical excitation, as discussed above. By tuning an applied microwave field in resonance with its transitions, the spin can also be readily manipulated. Although it is difficult to address a single spin with microwaves, one can prepare and observe a single spin by confining the optical excitation volume to a single NV center. These ingredients provide a straightforward means to prepare, manipulate, and measure a single electron spin in the solid state at room temperature[87].

Our observations of the NV electron spin can be roughly divided into continuous-

wave (CW) and pulsed experiments. In both cases, we isolate a single spin using confocal microscopy and apply microwaves to it using a 20μm copper wire drawn over the surface of the sample (Fig. 2.4, Fig. 2.3).

2.5.1 Continuous-wave experiments

For continuous-wave (CW) measurements, microwave and optical excitation was applied at constant power to the NV center, and the fluorescence intensity into the phonon sideband was measured as a function of microwave frequency. The continuous 532nm excitation polarizes the electron spin into the brighter $m_s = 0$ state; when the microwave frequency is resonant with one of the spin transitions $m_s = 0 \rightarrow m_s = \pm 1$, the population is redistributed between the two levels, and the fluorescence level decreases. In the absence of an applied magnetic field, the electron spin resonance (ESR) signal occurs at 2.87 GHz (see Fig. 2.8), while in a finite magnetic field the two transitions are shifted apart by $\sim m_s \cdot$ 2.8 MHz/Gauss.

Close examination of a single $m_s = 0 \rightarrow m_s = -1$ transition reveals hyperfine structure associated with the nitrogen forming the NV center (Fig. 2.8B). The $I = 1$ ^{14}N nuclear spin has a hyperfine structure (Fig. 2.8C) which is governed by the Hamiltonian[98]

$$H^{(N)} = A_{||}^{(N)} S_z I_z^{(N)} + A_{\perp}^{(N)} \left(S_x I_x^{(N)} + S_y I_y^{(N)} \right) + P \left((I_z^{(N)})^2 - \frac{1}{3} (I^{(N)})^2 \right), \qquad (2.2)$$

where $I^{(N)}$ is the nitrogen nuclear spin and S is the NV center electron spin. A strong quadrupole interaction splits the $m_N = \pm 1$ states off from the $m_N = 0$ state by $P \approx -5$ MHz [99], effectively freezing the orientation of the nitrogen nuclear spin for magnetic fields $\ll 1$ Tesla. In addition, the ^{14}N nuclear spin I_N interacts with

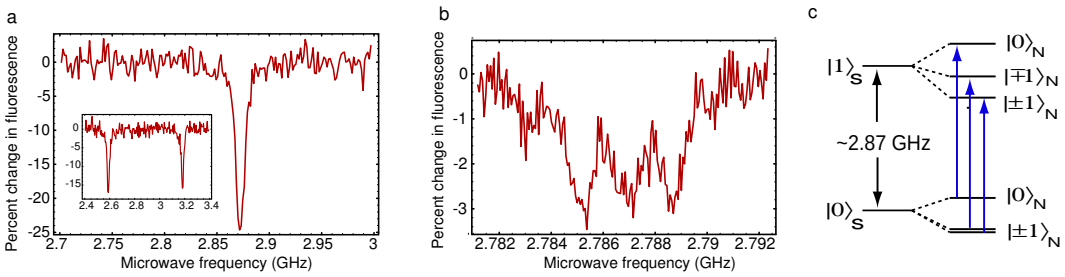

Figure 2.8: *Continuous-wave optically detected magnetic resonance. (A) Fluorescence intensity of a single NV center as a function of microwave frequency, under strong continuous-wave (CW) microwave and optical excitation. The fluorescence is normalized to the fluorescence in the absence of microwave excitation. A strong resonance occurs at 2.87 GHz, the zero-field splitting. (inset) In an applied magnetic field* $B_z \sim 100$ *Gauss, the* $m_s = \pm 1$ *levels are split by Zeeman shifts, leading to two resonances. (B) A closeup of the* $m_s = -1$ *transition (in a small magnetic field) under weak CW microwave and optical excitation. The resonances correspond to the three nitrogen-14 nuclear spin sublevels. (C) Hyperfine structure for the NV electron spin coupled to the host* ^{14}N *nuclear spin[81, 97].*

the electron spin S, so that in the electron spin excited state $m_s = 1$, the $m_N = \pm 1$ states are split from the $m_N = 0$ state by $P + A_{||}^{(N)}$ and $P - A_{||}^{(N)}$. Since the electron spin resonance transitions cannot change the nuclear spin state, the three allowed transitions (illustrated by blue arrows in Fig. 2.8C) are separated by $A_{||}^{(N)} \approx 2.2MHz$.

These CW measurements served primarily as a means to calibrate the frequency of microwave excitation appropriate for pulsed experiments. However, the ^{14}N hyperfine structure illustrates that CW measurements can also be useful for determining interaction strengths between the NV electron spin and other nearby spins.

2.5.2 Pulsed microwave experiments

Continuous-wave spectroscopy provides a means to measure the energy levels of the NV spin system. To observe the spin dynamics, we must move to the time do-

main, and apply pulses of resonant microwaves. The excitation sequence for pulsed microwave experiments is illustrated in Fig. 2.9A. All experiments begin with electron spin polarization and end with electron spin measurement, both of which are accomplished using 532nm excitation. In between, different microwave pulse sequences can be applied to manipulate the electron spin.

Rabi nutations

In a small applied magnetic field, the $m_s = 0$ to $m_s = 1$ spin transition of the NV center constitutes an effective two-level system. Driving this transition with resonant microwave excitation will thus induce population oscillations between the ground $m_s = 0$ and excited $m_s = 1$ states; these are known as Rabi nutations [5]. To observe Rabi nutations, we drive the transition with a resonant microwave pulse of varying duration t and measure the population remaining in $m_s = 0$. Fig. 2.9B shows a typical Rabi signal.

For resonant microwave excitation, Rabi oscillations correspond to complete state transfer between $m_s = 0$ and $m_s = 1$. This allows us to calibrate our measurement tool in terms of the population p in the $m_s = 0$ state. As shown in Fig. 2.9A, we can identify the minimum in fluorescence with $p = 0$ and the maximum with $p = 1$. For weak or off-resonant microwave fields we employ a more careful analysis, which fits the data to a multi-level model including all of the hyperfine structure associated with the ^{14}N nuclear spin and any other nearby spins. In either case, we can present data from more complicated pulsed experiments in units of $m_s = 0$ population p obtained from fits to Rabi nutations observed under the same conditions.

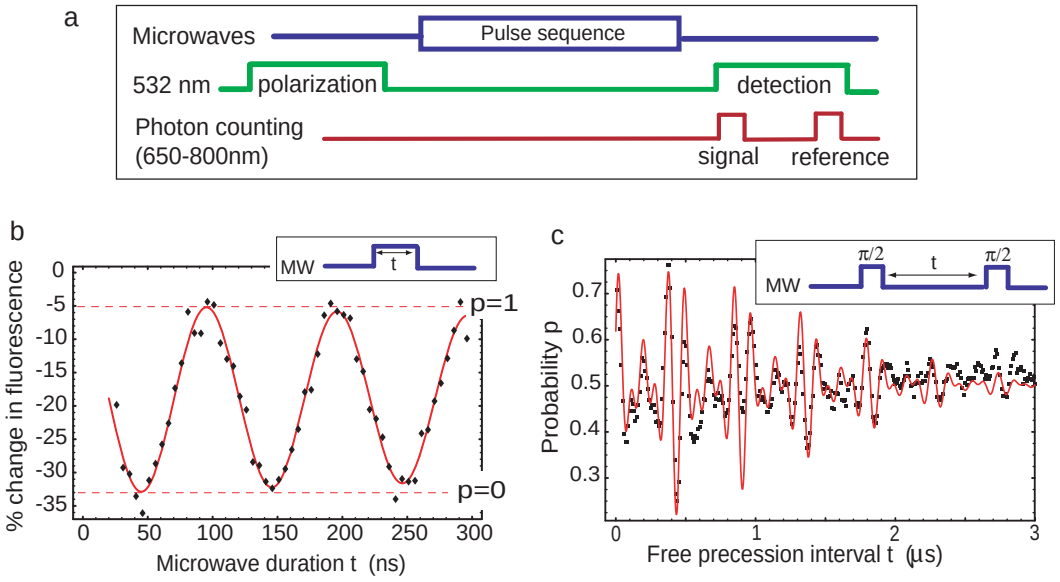

Figure 2.9: *Pulsed electron spin resonance. (A) Experimental procedure. (B) Rabi nutations. (C) Ramsey fringes.*

The frequency Ω of the Rabi nutations depends on the microwave power I_{MW} as $\Omega \propto \sqrt{I_{MW}}$. For a given microwave power, we observe Rabi nutations to calibrate the pulse length required to flip the spin from $m_s = 0$ to $m_s = 1$; this is known as a π pulse, because it corresponds to half of the Rabi period. Shorter and longer pulses create superpositions of the spin eigenstates; in particular, a microwave θ pulse (i.e. of duration $\tau = \theta/\Omega$) sends the $m_s = 0$ state $|0\rangle$ into the superposition $\cos\theta\,|0\rangle + i\sin\theta\,|1\rangle$. This corresponds to rotating the effective spin-1/2 system $\{|0\rangle, |1\rangle\}$ by θ about an axis in the $\hat{x} - \hat{y}$ plane. The relative phase of the two components (or, equivalently, the orientation of the axis in the $\hat{x} - \hat{y}$ plane) is set by the phase of the microwave excitation. For a single pulse, this phase does not matter (it could equally well be incorporated into a redefinition of $|1\rangle$), but composite pulse sequences often make use of shifts in the microwave phase. As an example, a pulse A of duration

θ_A followed by a 90 degree phase shifted pulse B of duration θ_B would correspond to rotating the spin by θ_A around the $\hat{x}$ axis followed by a rotation by θ_B around the $\hat{y}$ axis.

Ramsey fringes

Rabi nutations correspond to driven spin dynamics. We can also observe the free (undriven) spin dynamics by generating a superposition of the spin eigenstates $m_s = 0$ and $m_s = 1$, letting it evolve freely, and then converting the phase between the two eigenstates into a measurable population difference. This is accomplished using a Ramsey technique [5], which consists of the microwave pulse sequence $\pi/2 - \tau - \pi/2$ as illustrated in the inset to Fig. 2.9C. For a simple two-level system, the Ramsey sequence leads to population oscillations with a frequency equal to the microwave detuning δ. Because of the ^{14}N hyperfine structure, we observe a signal from three independent two-level systems, which oscillate at $\delta, \delta + 2.2$ MHz, and $\delta - 2.2$MHz. These three signals beat together, producing the complicated pattern shown in Fig. 2.9C. The data is shown with a fit to three superposed cosines (red), corresponding to the three hyperfine transitions driven by microwaves detuned by 8 MHz.

The fit to the Ramsey data includes a Gaussian envelope $e^{(-\tau/T_2^*)^2}$, which decays on a timescale $T_2^* = 1.7 \pm 0.2\mu$s known as the electron spin dephasing time. The dephasing time is the timescale on which the two spin states $m_s = 0$ and $m_s = 1$ accumulate random phase shifts relative to one another. For the NV center, these random phase shifts arise primarily from the effective magnetic field created by a complicated but slowly-varying nuclear spin environment. To understand this envi-

ronment in greater detail, it is necessary to employ more complicated pulse sequences which eliminate the phase shifts associated with the static ^{14}N spin and quasi-static effects of the environment. This is addressed in the following chapter.

Chapter 3

The mesoscopic environment of a single electron spin in diamond

3.1 Introduction

Spin-echo spectroscopy of a single NV center has allowed us to gain remarkable insight into its mesoscopic solid-state environment. In particular, we find that NV centers in a high-purity diamond sample have electron spin coherence properties that are determined by ^{13}C nuclear spins. These isotopic impurities form a spin bath for the NV "central spin" [100]. Furthermore, the set of proximal ^{13}C spins in the immediate vicinity of the NV center forms a mesoscopic component of the environment. Most importantly, these individual, proximal ^{13}C spins can couple coherently to the NV electron spin. Although each NV center has its own set of proximal nuclear spins, and thus its own specific dynamics, there are well-defined general features of the coupled electron-nuclear spin systems. By selecting an NV center with a desired nearby

^{13}C nucleus, and adjusting the external magnetic field, we can effectively control the coupled electron-nuclear spin system. Our results show that it is possible to coherently address individual, isolated nuclei in the solid state, and manipulate them via a nearby electron spin. Due to the long coherence times of isolated nuclear spins [50], this is an important element of many solid-state quantum information approaches, from quantum computing [49, 101] to quantum repeaters [102, 96, 103].

3.2 Spin-echo spectroscopy

Spin echo is widely used in bulk electron spin resonance (ESR) experiments to study interactions and determine the structure of complex molecules [104]. Likewise, spin-echo spectroscopy provides a useful tool for understanding the complex mesoscopic environment of a single NV center: by observing the spin-echo signal under varying conditions, we can indirectly determine the response of the environment, and from this glean details about the environment itself.

As discussed in Chapter 3, Ramsey spectroscopy of a single NV center is complicated by hyperfine ^{14}N level shifts and quasi-static frequency shifts from a slowly-changing environment. These frequency shifts can be eliminated by using a spin-echo (or Hahn echo) technique [105]. It consists of the sequence $\pi/2 - \tau - \pi - \tau' - \pi/2$ (see Fig. 3.1a), where π represents a microwave pulse of sufficient duration to flip the electron spin from $m_s = 0$ to $m_s = 1$, and τ, τ' are durations of free precession intervals. As with the Ramsey sequence, the Hahn sequence begins by preparing a superposition of electron spin states $1/\sqrt{2}\,(|0\rangle + i\,|1\rangle)$ using a $\pi/2$ microwave pulse. This superposition precesses freely for a time τ, so that, for example, the

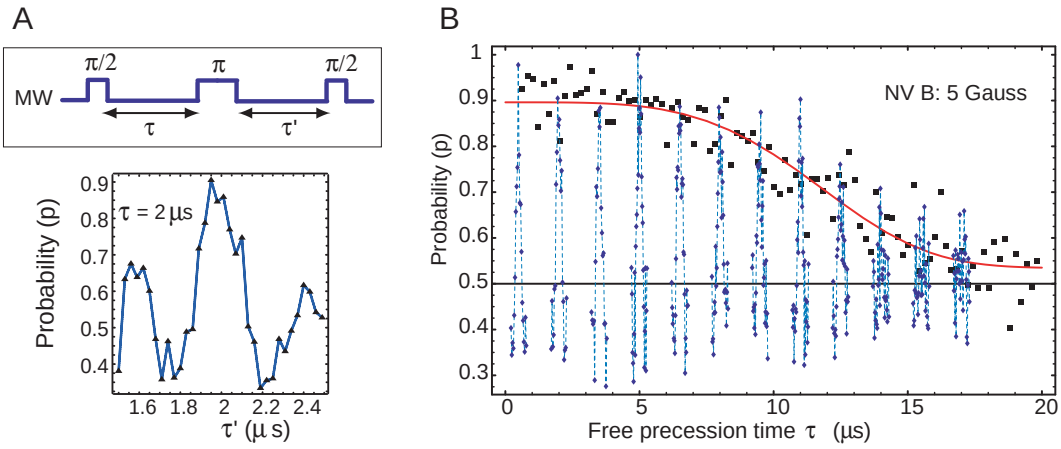

Figure 3.1: **A**, Spin echo. The spin-echo pulse sequence (left) is shown along with a representative time-resolved spin-echo (right) from NV B. A single spin-echo is observed by holding τ fixed and varying τ'. **B** Spin echo decay for NV B in a small magnetic field (B $\sim$ 5 G). Individual echo peaks are mapped out by scanning τ' for several values of τ (blue curves). The envelope for the spin echoes (black squares), which we refer to as the spin-echo signal, maps out the peaks of the spin echoes. It is obtained by varying τ and τ' simultaneously, so that $\tau = \tau'$ for each data point. The spin-echo signal is fitted to $\exp(-(\tau/\tau_C)^4)$ (red curve) to obtain the estimated coherence time $\tau_C = 13 \pm 0.5\mu$s .

$|1\rangle$ component picks up a phase shift $\delta\tau$ relative to the $|0\rangle$ component, yielding $1/\sqrt{2}\left(|0\rangle + ie^{i\delta\tau}|1\rangle\right)$. The π pulse in the middle of the spin-echo sequence flips the spin, resulting in the state $1/\sqrt{2}\left(i|1\rangle - ie^{i\delta\tau}|0\rangle\right)$. Assuming that the environment has not changed since the first free precession interval, the $|1\rangle$ component will pick up the phase $\delta\tau'$ during the second free precession interval, leaving the system in the state $1/\sqrt{2}\left(ie^{i\delta\tau'}|1\rangle - ie^{i\delta\tau}|0\rangle\right)$. When the two wait times are precisely equal, $\tau = \tau'$, the random phase shift factors out, so the final $\pi/2$ pulse puts all of the population back into $|0\rangle$. When the wait times are unequal, the Hahn sequence behaves like a Ramsey sequence with a delay $\tau - \tau'$.

Typical Hahn echo data are shown in Fig. 3.1. One type of signal, which we refer to as an "echo peak", is obtained by holding the first free precession interval τ constant

and changing the second free precession interval τ'. This yields a characteristic peak when $\tau = \tau'$, i.e. when the static phase shifts from the two precession intervals precisely cancel, as shown in Fig. 3.1a. The height of this peak can change for different values of τ. For example, Fig. 3.1b shows a series of spin-echo peaks (blue lines) taken for different values of τ, and the peak height decays on the timescale of $\tau \sim 10\mu$s. We can map out this peak height by changing the two precession intervals in tandem, $\tau = \tau'$, which yields what we call the "spin-echo signal" $p(\tau = \tau')$ shown in Fig. 3.1b by black squares. If the environment were completely static, the spin-echo signal would be unity regardless of τ: a non-trivial spin-echo signal means that the environment must be evolving on a timescale faster than τ.

3.3 Spin bath dynamics: spin echo collapse and revival

3.3.1 Experimental observations

Spin echo decay

The spin-echo signal shown in Fig. 3.1b decays on a timescale τ_C which is much longer than the dephasing time T_2^* found by Ramsey spectroscopy: $\tau_C \approx 13 \pm 0.5\mu$s $\gg T_2^*/2$. This indicates a long correlation (memory) time associated with the electron spin environment.

We found that the decay time τ_C depends strongly on the magnetic field: the spin-echo signal collapses more quickly as the magnetic field is increased (see Fig. 3.2.

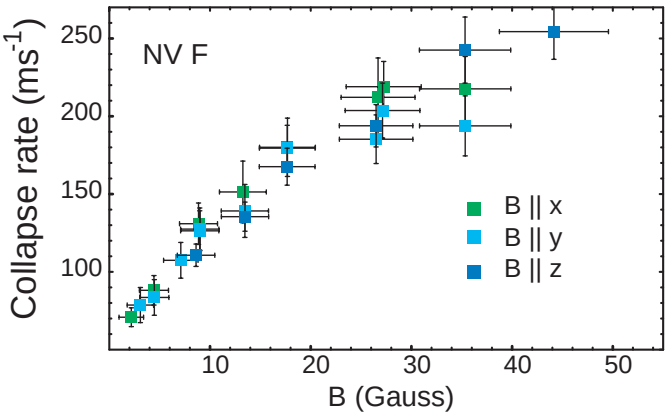

Figure 3.2: Initial decay rate of the spin-echo signal $1/\tau_C$ as a function of magnetic field, for three perpendicular orientations of the magnetic field.

This magnetic field dependence was observed for several centers, though the precise rate of collapse varied slightly from center to center.

Spin echo revivals

The spin-echo signal exhibits a further dependence on magnetic field, which becomes apparent when we extend the observation time τ well beyond the collapse time τ_C. In particular, at $\tau = \tau_{\mathbf{R}} > \tau_C$, the spin echo revives. Fig. 3.3 shows the spin-echo signal from NV center B in four different magnetic fields (each oriented along $\hat{z}$). We find that the initial collapse of the signal is followed by periodic revivals extending out to $2\tau \sim 200$ μs, and the revivals become more frequent with increasing magnetic field. The revivals indicate that the collapse time τ_C is not a good indication of the electron spin coherence time. Fitting the peaks of the revivals allows us to extract a value for electron spin coherence time $T_2 = 242 \pm 13\mu$s (see Fig.3.6 for fit).

We find that the revival rate $1/\tau_{\mathbf{R}}$ by fitting the data to a periodic quartic ex-

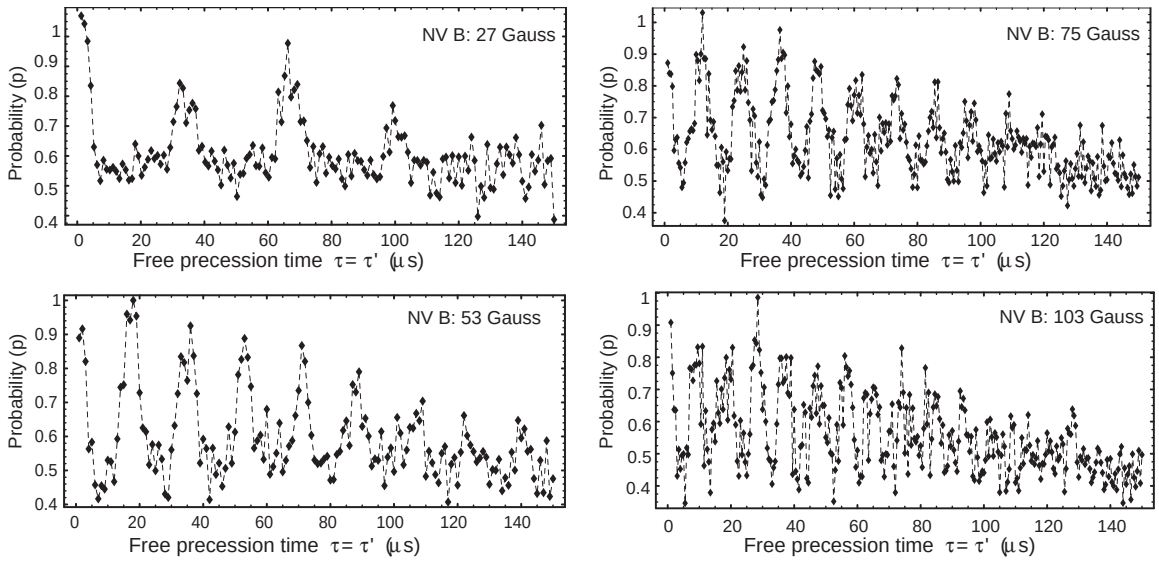

Figure 3.3: Spin-echo signal for NV B for four values of the magnetic field $||\hat{z}$.

ponential, $\sum_j A_j e^{(t-j\tau_R)^4/\tau_C^4}$. The resulting revival rate precisely matches the Larmor precession frequency for ^{13}C nuclear spins of 1.071 kHz/G (Fig. 3.4A). This result indicates that the dominant environment of the NV electron spin is a nuclear spin bath formed by the spin-1/2 ^{13}C isotope, which exists in 1.1% abundance in the otherwise spinless ^{12}C diamond lattice. The ^{13}C precession induces periodic decorrelation and rephasing of the nuclear spin bath, which leads to collapses and revivals of the electron spin echo signal shown in Fig. 3.3.

Interpretation

These results can be understood qualitatively by considering a single NV spin in a pure natural diamond lattice, which consists of 98.9% spinless ^{12}C atoms interspersed with 1.1% spin-1/2 ^{13}C nuclei (Fig. 3.4B). Each ^{13}C nuclear spin $I^{(j)}$ interacts with

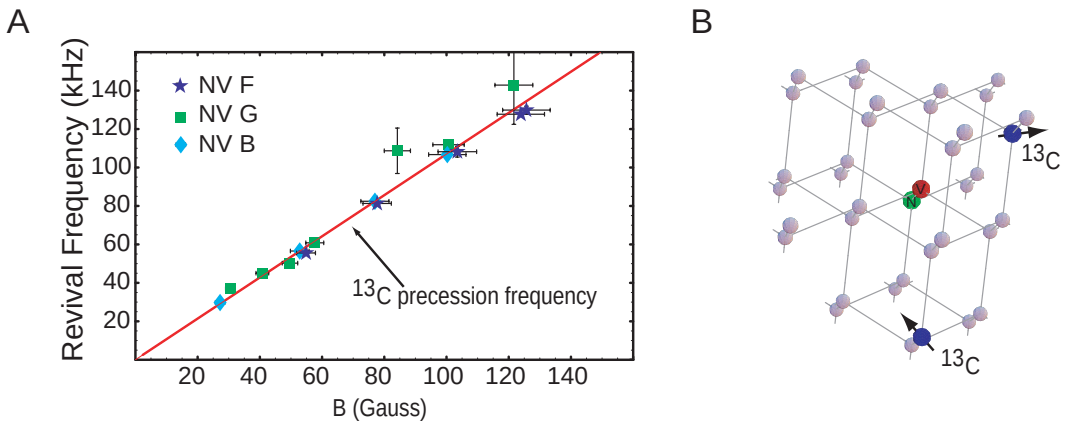

Figure 3.4: (A) Revival rate, shown along with the Larmor precession frequency for ^{13}C nuclear spins. (B) Illustration of an NV center in the diamond lattice, which interacts with the random set of ^{13}C nuclear spins in the surrounding lattice sites.

the electron spin S via the hyperfine interaction, contributing to an effective magnetic field at the site of the NV center. In an external magnetic field, the large 2.87 GHz zero-field splitting inhibits electron spin transitions, but the spin-1/2 nuclear spins are free to precess at the Larmor frequency $g_n\mu_n B$, where $g_n\mu_n = 1.071$ kHz/G. Consequently, the effective magnetic field experienced by the NV center oscillates with the ^{13}C Larmor frequency. When the free precession interval τ is precisely equal to an integer multiple of the oscillation period, then the (time-dependent) magnetic field behaves identically during the two free precession intervals, and the two random phase shifts cancel. This leads to the observed oscillations in the spin-echo signal as a function of τ.

3.3.2 Modelling the spin-bath environment

To understand our results quantitatively, we must examine the interaction between the NV electron spin all of the ^{13}C nuclear spins in the lattice. As a first

approximation, we assume that the ^{13}C spins do not interact with each other, so that we only need to understand how the NV spin S interacts with a single ^{13}C spin I^j at an arbitrary location r^j. The total interaction is then given by a sum over all of the ^{13}C nuclear spins in the lattice.

Hyperfine interactions

We begin by considering an NV electronic spin S interacting with a single ^{13}C nucleus $\mathbf{I}^{(j)}$ located a distance r_j in the direction $\mathbf{n}_j$ from the NV spin. This ^{13}C spin couples to the electron spin via the hyperfine interaction[106, 104]:

$$V^{(j)} = -\mu_e\mu_n\frac{8\pi|\psi_e(r_j)|^2}{3}\mathbf{S}\cdot\mathbf{I}^{(j)} + \left\langle\frac{\mu_e\mu_n}{r_j^3}\left(\mathbf{S}\cdot\mathbf{I}^{(\mathbf{j})} - 3(\mathbf{n}_j\cdot\mathbf{S})(\mathbf{n}_j\cdot\mathbf{I}^{(j)})\right)\right\rangle, \qquad (3.1)$$

where μ_e and μ_n are the electron and nuclear magnetic moments respectively, $|\psi_e(r_j)|^2$ is the electron spin density at the site of the nuclear spin, and brackets <> denote an average over the electron wavefunction $\psi_e(r)$. The essence of this Hamiltonian, which can be represented as $V^{(j)} = \mathbf{B}^{(j)}_{m_s}\cdot\mathbf{I}^{(j)}$, is that the nuclear spin experiences an effective magnetic field $\mathbf{B}^{(j)}_{m_s}$ which depends on the electron spin state m_s.

Because the $S = 1$ electron spin has a large zero-field splitting, it does not precess significantly in moderate magnetic fields. The dynamics of the coupled system can therefore be most easily understood by examining the evolution of the $I = 1/2$ ^{13}C spin conditional on the state m_s of the electron spin. The resulting four-level system is shown in Figure 3.5, where we have chosen the ^{13}C spin axis to diagonalize the hyperfine interaction in the $m_s = 1$ manifold. In the excited state manifold $m_s = 1$, the nuclear spin states are split by $\omega_{j,1}$, but do not evolve into each other. In the ground state manifold, however, the nuclear spin states are coupled to each

other, and precess at rate $\omega_{j,0}$ around the axis of the effective magnetic field $B_{0,j}$

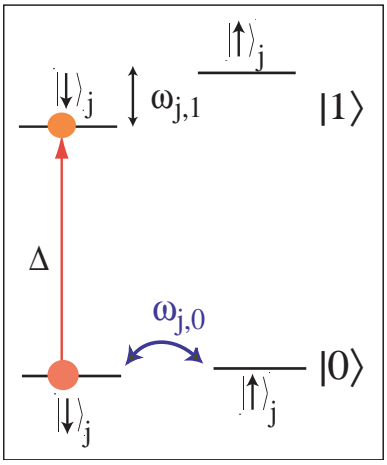

Figure 3.5: Level diagram for the NV electron spin coupled to the j^{th} ^{13}C nuclear spin.

It is worth noting that we are neglecting any influence of the ^{14}N hyperfine structure. This is valid because the ^{14}N nuclear spin has a large quadrupolar splitting $P \sim 5.1$ MHz [107, 97, 99], which suppresses transitions between the ^{14}N nuclear spin levels. For magnetic fields $B \ll P/(g_n\beta_n) \sim 1.64$ T, the orientation of the ^{14}N nuclear spin is fixed by the quadrupole axis, and it does not precess. Consequently, for our measurements the host ^{14}N nucleus can be treated a static spin which can only introduce a level shift on the NV spin microwave transition. Since static level shifts are cancelled by a spin-echo sequence for $\tau = \tau'$, our spin-echo measurements are unaffected by the presence of the ^{14}N nuclear spin. To simplify our analysis, we therefore neglect entirely the ^{14}N hyperfine structure.

Calculation of the spin-echo signal arising from a coupled electron-nuclear spin system

The hyperfine interaction between the electron spin and a single ^{13}C nuclear spin has a dramatic effect on the spin-echo signal. After the initial $\pi/2$ pulse in the spin-echo sequence, the electron spin state $\left(|m_s = 0\rangle + |m_s = 1\rangle\right)/\sqrt{2}$ becomes entangled with the nuclear spin state at a rate determined by $\mathbf{B}_0^{(j)}$ and $\mathbf{B}_1^{(j)}$. As the electron spin becomes entangled with the nuclear spin, the spin echo signal diminishes; when it gets disentangled, the signal revives. The resulting spin-echo signal thus exhibits periodic reductions in amplitude, with modulation frequencies $\omega_{j,ms}$ associated with each spin-dependent field $\mathbf{B}_{m_s}^{(j)}$. By considering the unitary evolution associated with the dipole Hamiltonian, (see e.g. [108] for derivation), we obtain a simple expression for the spin echo signal $p_j = (S_j + 1)/2$, with pseudospin S_j given by

$$S_j(\tau) = 1 - \frac{2|\mathbf{B}_0^{(j)} \times \mathbf{B}_1^{(j)}|^2}{|B_0^{(j)}|^2 |B_1^{(j)}|^2} \sin^2(\omega_{j,0}\tau/2) \sin^2(\omega_{j,1}\tau/2). \tag{3.2}$$

Furthermore, we include multiple ^{13}C nuclei in our description by taking a sum over the dipole interactions $V = \sum_j V^{(j)}$; the corresponding unitary evolution yields the echo signal $p = (S + 1)/2$ with $S = \prod_j S_j$.

Simulation of an ensemble of ^{13}C nuclear spins

The total spin-echo signal which we observe in experiments is calculated by taking a product of the spin-echo signals from each nuclear spin, $S = \prod_j S_j$. Qualitatively, we expect that each nuclear spin will experience a different dipole field from the $m_s = 1$ electron spin state, and therefore a different oscillation frequency $\omega_{j,1}$ will emerge its contribution to the spin-echo. When the electron spin is in the $m_s = 0$ state, however,

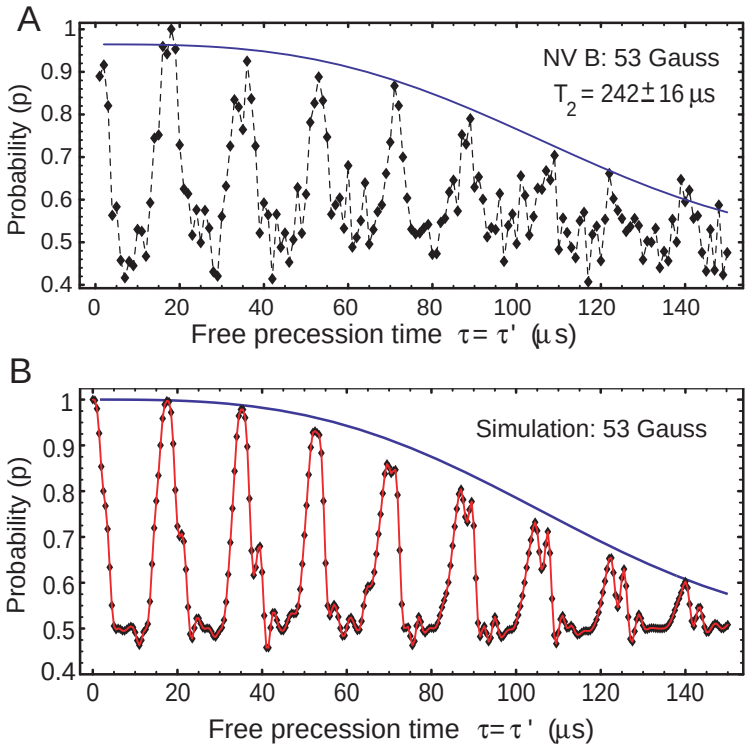

Figure 3.6: **A**, Collapse and revival of the spin-echo signal from NV B in a moderate magnetic field (53 Gauss). The decay of the revivals (blue curve) is found by fitting the height of each revival to $\exp(-(2\tau/T_2)^3)$, as would be expected from ^{13}C dipole-dipole induced dephasing [48, 106], with $T_2 \approx 242 \pm 16\mu$s. **B** Simulation of collapse and revival for an NV center in 53 Gauss applied magnetic field, surrounded by a random distribution of 1.1% ^{13}C spins. Additional structure in the simulation arises from coherent interactions with the nearest ^{13}C in the lattice, via the same mechanism shown in Fig. 3.7. The phenomenological decay is added to the simulation for comparison with experimental data.

the electron spin dipole field vanishes, and we expect that each nuclear spin should experience roughly the same magnetic field $B_{j,0} = B_0$, set by the external magnetic field. Consequently, we expect that the spin-echo signal should decay as the different $\omega_{j,1}$ frequencies beat against each other, but revive when $\tau = 2\pi/\omega_0$.

We can put this intuition on more formal footing by making a secular approximation[104] to the dipole Hamiltonian Eq. 3.1. This approximation neglects the terms propor-

tional to S_x, S_y because they are suppressed by the large electron spin splitting $\Delta \approx 2.87$ GHz. In this model (Fig. 3.5) the $m_s = 1$ nuclear spin states have a fixed hyperfine splitting $\omega_{j,1} \sim \mu_e\mu_n(< 1/r_j^3 > +8\pi|\Psi_e(r_j)|^2/3)$, whereas the degenerate $m_s = 0$ nuclear spin states can precess in a small applied magnetic field at the bare ^{13}C Larmor frequency $\omega_{j,0} = \omega_0$. When we include many nuclear spins in the echo signal, the fast echo modulations $\omega_{j,1}$ interfere with each other, causing initial decay of the signal as $\exp -(\tau/\tau_C)^4$. However, when $\tau = \tau' = 2\pi/\omega_0$, $S_j = 1$ for all j, and the spin-echo signal revives.

To compare this theory to our experimental results, we have performed simulations based on Eqs. (3.1 and 3.2). Approximately 1000 ^{13}C spins were placed randomly in a lattice around the NV center with an appropriate volume to give a 1.1% concentration of ^{13}C . For each spin, the effective magnetic fields B_{j,m_s} were calculated from the full hyperfine interaction (including non-secular terms), assuming that an electron spin corresponds to a point dipole located on the vacancy. These effective magnetic fields were then used to calculate the spin-echo signal S_j, as given by Eq. (3.2). The total spin-echo signal is then $S = \prod_j S_j$, from which the expected probability to be in the $m_s = 0$ state $p = (1 + S)/2$ may be found.

Each random set of ^{13}C spin locations was considered as a single "center"; accordingly, no disorder averaging was performed. However, a population of such centers could then be compared to the experimental data. Such simulations yield good qualitative agreement with experimental data. However, the point dipole moment approximation underestimates the collapse rate by about 20-40%. This is consistent with the picture we obtain from analysis of echo modulation data (see following sections),

and indicates that the finite extent of the electron wavefunction plays an important role even for fairly remote nuclear spins.

3.4 Spin-echo modulation

Every NV center studied exhibited spin-echo collapse and revival on long time scales, but many also showed more complicated evolution on short time scales. As an example, the signal from the center E is shown in Fig. 3.7A. The oscillating signal has slow and fast components at ~ 0.6 MHz and ~ 9 MHz respectively. The fast component (referred to as the modulation frequency) is relatively insensitive to the magnetic field (Fig. 3.7B), but the slow component (envelope frequency) varies dramatically with the magnetic field amplitude and orientation (see Fig. 3.7C,D). These observations indicate the electron spin gets periodically entangled and disentangled with an isolated system, until the spin echo finally collapses from interactions with the precessing bulk spin bath. Some NV centers, for example NV C, exhibit several envelope and modulation frequencies, indicating that the electron spin interacts coherently with multiple ^{13}C nuclei (Fig. 3.8). Other centers, for example NV F, show no evidence of proximal ^{13}C spins.

The spin-echo modulation signal closely resembles the form for the spin-echo contribution S_j from an isolated nuclear spin I^j. Indeed, the experimental data is well fit by the expected functional form $\exp(-(\tau/\tau_C)^4)\left(a - b\ \sin\left(\omega_0\tau/2\right)^2 \sin\left(\omega_1\tau/2\right)^2\right)$, where $\omega_{0,1}$ is the nuclear spin precession frequency in the $m_s = 0, 1$ manifold respectively. The fast modulation frequency might be expected for a nuclear spin located close to the NV center electron spin. However, the observed $m_s = 0$ precession

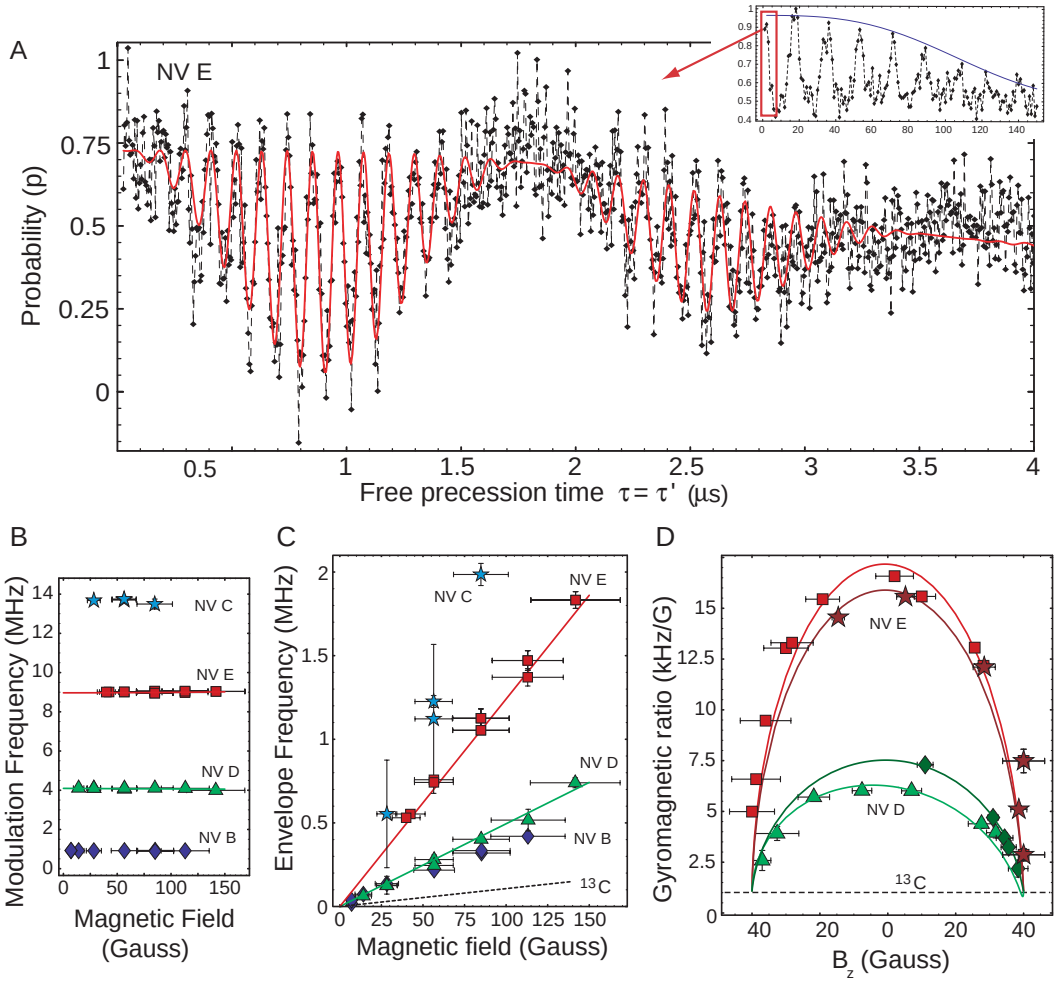

Figure 3.7: **A**, Spin echo modulation as observed for NV E with B = 42 ±6 Gauss $||-\hat{x}+\hat{z}$. The red curve represents a theoretical fit with the expected functional form $\exp(-(\tau/\tau_C)^4)\left(a - b\ \sin(\omega_0\tau/2)^2 \sin(\omega_1\tau/2)^2\right)$, yielding the modulation frequency $\omega_0 \sim 2\pi$ 9 MHz and envelope frequency $\omega_1 \sim 2\pi$ 0.6 MHz. **B**, Modulation frequency for NV B-E as a function of magnetic field B $||-\hat{x}+\hat{z}$. **C**, Envelope frequency (same conditions as **B**). The envelope frequencies are different for each center, but they all exceed the bare ^{13}C Larmor precession frequency (dashed line). **D**, Effective gyromagnetic ratio (envelope frequency / magnetic field), versus magnetic field orientation for NV D and E. The amplitude of the magnetic field is fixed at 40 ± 4 Gauss. The magnetic field is varied in the x-z plane for NV D (red boxes) and NV E (green triangles) and y-z plane for NV D (dark red stars) and NV E (dark green diamonds) . Six free parameters which describe the interaction with the nearest ^{13}C spin were fit to the envelope and modulation frequency data [109], yielding the solid curves shown in (**B**, **C**, **D**).

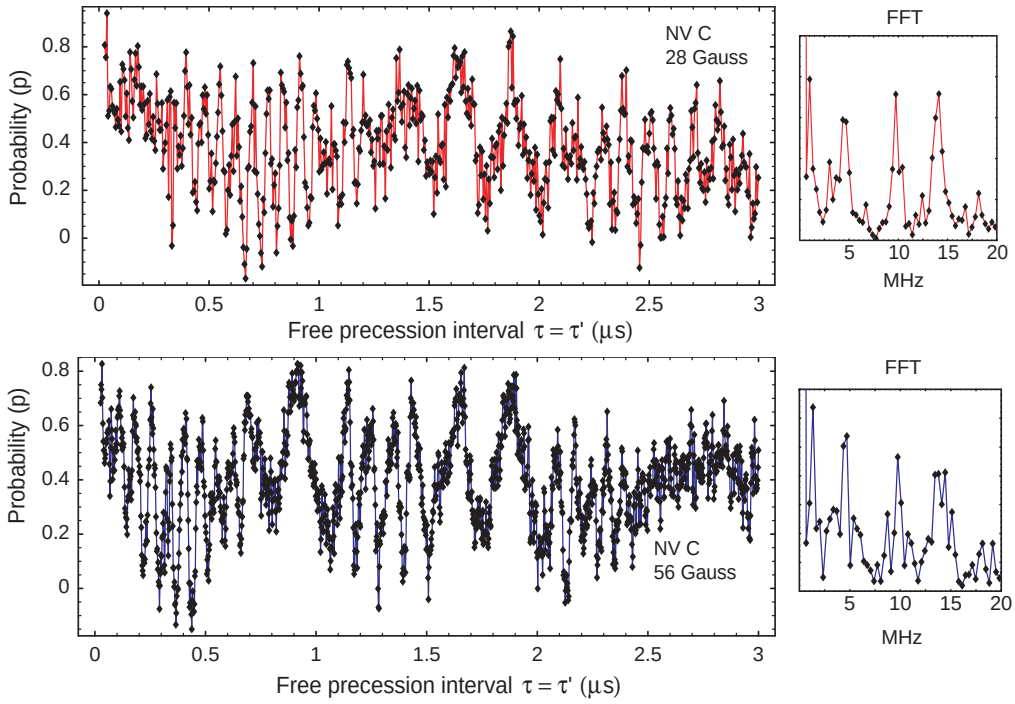

Figure 3.8: Spin-echo modulation for NV26 in two magnetic fields, including a fourier transform of the data. The same three echo modulation frequencies show up in both magnetic fields, but the envelope frequencies change, indicating that there are three nearby ^{13}C nuclei interacting with the NV center spin.

frequency ω_0 far exceeds the bare Larmor frequency of a ^{13}C nuclear spin.

3.5 Understanding the origin of spin-echo modulation

3.5.1 Enhancement of the nuclear gyromagnetic ratio

The simple picture that gave us insight into spin-echo collapse and revival cannot explain the observed echo modulation. In the secular approximation, where each nuclear spin precesses at the bare Larmor frequency in the $m_s = 0$ manifold, our theory

predicts that the spin-echo signal should collapse before coherent interactions with individual ^{13}C spins become visible. In fact, the nonsecular terms in the Zeeman and dipole interactions play a crucial role in isolating proximal nuclei from the spin bath. The nonsecular terms slightly mix the electron spin levels, introducing some electronic character to the nearby nuclear spin levels, and thus augmenting their magnetic moment by $\sim \mu_e(\omega_{j,1}/\Delta)$. Since $\mu_e \gg \mu_n$, this greatly enhances the nuclear Larmor precession rate for nearby spins. Furthermore, the enhancement is anisotropic: it is strongest when the external field is oriented perpendicular to the NV axis, corresponding to the largest degree of mixing. For a properly oriented magnetic field, proximal nuclei can thereby entangle and disentangle with the NV spin on timescales much faster than the bare ^{13}C Larmor period.

3.5.2 Comparison of experimental results to first-principles theory

We have seen that the nuclear spin evolution which leads to spin-echo modulation is governed by two effects of the hyperfine interaction: First, the secular terms in the hyperfine interaction cause an m_s-dependent energy splitting of the ^{13}C nuclear spin states, which can be interpreted as the dipole field produced by the electron spin. Second, the non-secular terms in the hyperfine interaction alter the g-tensor for a nearby nuclear spin, so that the effect of an external magnetic field is magnified by the electron spin [1]. Starting from the hyperfine interaction, we will derive the electron spin dipole field and the effective g-tensor for the nuclear spin. In addition

[1] This is termed the "pseudo-nuclear Zeeman" effect in the NMR literature, see e.g. [104].

to providing a qualitative understanding of our data, the resulting expressions allow us to extract the components of the hyperfine interaction between NV D and E and their nearest ^{13}C spins.

The hyperfine interaction tensor

Physically, the hyperfine interaction between the NV electron spin S and the j^{th} nuclear spin $I^{(j)}$ arises from the dipolar and contact terms presented in Eq.(1) of the main text. Mathematically, it is convenient to write this interaction in terms of a symmetric tensor $\alpha^{(j)}_{\mu\nu}$ where

$$H^{(j)}_{\text{dip}} = \sum_{\mu,\nu=x,y,z} S_\mu \alpha^{(j)}_{\mu\nu} I^{(j)}_\nu \ . \tag{3.3}$$

If the electron spin has a wavefunction $\psi(\mathbf{r})$, and the nuclear spin is located at a position $\mathbf{r}_j$, then the components of this tensor are given by

$$\alpha^{(j)}_{\mu\nu} = \mu_e \mu_n \left[\left(-\frac{8\pi}{3} |\psi(\mathbf{r}^j)|^2 + \left\langle \frac{1}{|\mathbf{r}-\mathbf{r}_j|^3} \right\rangle \right) \delta_{\mu\nu} - 3 \left\langle \frac{n^j_\mu n^j_\nu}{|\mathbf{r}-\mathbf{r}_j|^3} \right\rangle \right] \tag{3.4}$$

where $\mathbf{n}^j$ is a unit vector along the $\mathbf{r}-\mathbf{r}^j$ axis, and $\delta_{\mu\nu}$ is the Kronecker delta. The overall strength of the interaction can be quantified by a root mean square average of the diagonal components, $A_j = \sqrt{\text{Tr}[\alpha^{(\mathbf{j})^2}]/3}$.

For spins sufficiently far away from the NV center (such that $\langle 1/|\mathbf{r}-\mathbf{r}^j|^3\rangle \approx 1/\left\langle |\mathbf{r}-\mathbf{r}^j| \right\rangle^3$ and $|\psi(\mathbf{r}^j)|^2 \approx 0$), the full hyperfine interaction reduces to an effective point-dipole coupling, which has only three independent parameters. In particular, in the point-dipole model $\alpha^{(j)}_{\mu\nu}$ can be written in terms of the strength A_j and a unit vector along polar angle θ and azimuthal angle ϕ which characterizes the angular orientation of the two spins.

For closer spins, the finite extent of the electron wavefunction can significantly enhance the interaction strength. The enhancement comes from both a finite contact term $|\psi(\mathbf{r}^j)|^2 > 0$ and the averaged dipolar term $\langle 1/|\mathbf{r}-\mathbf{r}^j|^3\rangle \gg 1/\langle|\mathbf{r}-\mathbf{r}^j|\rangle^3$. Furthermore, the angular averages do not necessarily factorize, i.e. $\left\langle n_\mu^j n_\nu^j\right\rangle \neq \left\langle n_\mu^j\right\rangle \langle n_\nu^j\rangle$, so we must keep track of four angular terms instead of two. In total, six parameters (which correspond to the six independent components of a symmetric tensor $\alpha^{(\mathbf{j})}$) are necessary to describe the interaction with a proximal nuclear spin.

Inclusion of the non-secular terms to lowest order in $1/\Delta$

To calculate the electron spin dipole field and the effective nuclear spin g-tensor, we must consider the full Hamiltonian describing the electron spin $\mathbf{S}$ coupled to the j^{th} nuclear spin $\mathbf{I}^j$. We write this Hamiltonian in a coordinate system which takes $\hat{z}$ along the NV axis, which lies along the [111] crystal axis, while $\hat{x}$ and $\hat{y}$ are fixed arbitrarily by taking $\hat{x}$ to lie in a horizontal plane with respect to laboratory coordinates. We thus obtain

$$H^{(j)} = H_{NV}^{(||)} + H_{NV}^{(\perp)} + H_B + H_{\rm dip}^{(||)} + H_{\rm dip}^{(\perp)}, \tag{3.5}$$

where the secular $(||)$ and non-secular $(\perp)$ terms are given by:

$$H_{NV}^{(||)} = \Delta S_z^2 - \mu_e B_z S_z \tag{3.6}$$

$$H_{NV}^{(\perp)} = -\mu_e \left(B_x S_x + B_y S_y\right) \tag{3.7}$$

$$H_B = -\mu_n \mathbf{B}\cdot\mathbf{I}^j \tag{3.8}$$

$$H_{\rm dip}^{(||)} = S_z \sum_\nu \alpha_{z\nu} I_\nu^j \tag{3.9}$$

$$H_{\rm dip}^{(\perp)} = \sum_\nu (S_x\alpha_{x\nu} + S_y\alpha_{y\nu}) I_\nu^j, \tag{3.10}$$

where $\Delta \approx 2.87$ GHz is the NV spin zero-field splitting, and we note that $\mu_e < 0, \mu_n > 0$.

The expression for the g-tensor and the hyperfine field can in principle be derived directly from this Hamiltonian, but a considerably simpler form may be obtained by finding an appropriate approximation. When Δ is the largest energy scale in the problem, as it is for all experimental conditions considered in this Report, the subspaces $|m_s\rangle$ with fixed electron spin projection along $\hat{z}$ are separated by energy gaps of order Δ. This allows us to write an effective Hamiltonian in a $1/\Delta$ series. The zeroth order term is the secular Hamiltonian, containing only those terms commuting with ΔS_z^2:

$$H_0 = H_{NV}^{(||)} + H_B + H_{\text{dip}}^{(||)}. \tag{3.11}$$

The next order correction arises from virtual transitions between m_s sublevels driven by either a transverse external magnetic field (B_x or B_y components) or by the hyperfine field of a nearby nuclear spin. The total perturbation is

$$U = H_{NV}^{(\perp)} + H_{\text{dip}}^{(\perp)}. \tag{3.12}$$

Within each m_s subspace, the first-order Hamiltonian $P_{m_s} H_0 + H_1^{m_s}$ can be found by using second order perturbation theory:

$$H_1^{m_s} = P_{m_s} U \frac{1}{E_{m_s} - (\hat{1} - P_{m_s}) H_0 (\hat{1} - P_{m_s})} U P_{m_s} \tag{3.13}$$

where $\hat{1}$ is the identity operator, P_{m_s} is the projector into the subspace with electron spin projection m_s along the $\hat{z}$ axis, and $E_{m_s} = \Delta m_s^2 - \mu_e B_z m_s$ is the zeroth-order energy of the electron spin under $H_{NV}^{(||)}$. Using this formalism, we obtain three effective nuclear spin Hamiltonians corresponding to the three m_s electron spin manifolds.

The first-order correction to the secular Hamiltonian can play an important role under certain circumstances. In particular, when virtual transitions between m_s states are driven by a transverse external field *and* the hyperfine interaction, the nuclear spin feels an effective field from the electron spin which depends on the external magnetic field. This effective field is larger than the applied magnetic field by a factor of order $\xi_j = |A_j|/\Delta \times |\mu_e/\mu_n|$. While $|A_j|/\Delta \ll 1$, $|\mu_e/\mu_n| \gg 1$, and the effect can be strong.

The effective g-tensor

We can characterize this enhancement of the applied magnetic field by defining an effective g-tensor for nuclear spin j. For each m_s manifold, the $\{\mu, \nu\}$ component of this g-tensor can be found from the perturbative form of the Hamiltonian

$$\mathbf{g}^j(m_s)_{\mu,\nu} = \left[\frac{d}{dB_\mu}\left(P_{m_s}H_0 + H_1^{m_s}\right)\right]_\nu . \tag{3.14}$$

This calculation gives us the bare g-tensor plus a correction:

$$\mathbf{g}^j(m_s) = \begin{pmatrix} 1 & & \\ & 1 & \\ & & 1 \end{pmatrix} - \frac{\mu_e}{\mu_n \Delta}(2 - 3|m_s|) \begin{pmatrix} \alpha_{xx}^{(j)} & \alpha_{xy}^{(j)} & \alpha_{xz}^{(j)} \\ \alpha_{xy}^{(j)} & \alpha_{yy}^{(j)} & \alpha_{yz}^{(j)} \\ 0 & 0 & 0 \end{pmatrix} \tag{3.15}$$

The effective g-tensor immediately gives us the enhanced ^{13}C Larmor precession frequency $\omega_{j,0} = |\mu_n \, \mathbf{B} \cdot \mathbf{g}^j(0)|$, which we identify as the envelope frequency we observe in spin-echo modulation. This envelope frequency depends on both the magnitude and the orientation of the applied magnetic field $\mathbf{B}$, and different orientations of the applied magnetic field are enhanced by different components of the effective g-tensor. By fitting the observed envelope frequencies under varying magnetic field orientations, we can thus extract five of the six components of the hyperfine interaction tensor $\alpha^{(\mathbf{j})}$.

The electron spin dipole field

To measure the remaining term, $\alpha_{zz}^{(j)}$, we must consider the second effect of the hyperfine interaction: each nuclear spin j experiences a dipole field from the electron spin regardless of the applied magnetic field. To calculate this dipole field, we could use the terms in the perturbative Hamiltonian which do not depend on external magnetic field. However, since the μ_e/μ_n enhancement does not occur here, it remains a valid approximation to use the bare dipole field:

$$\mathbf{B}_{\text{dip}}^{j} = \frac{1}{-\mu_n} \begin{pmatrix} \alpha_{xz}^{(j)} \\ \alpha_{yz}^{(j)} \\ \alpha_{zz}^{(j)} \end{pmatrix}. \tag{3.16}$$

For each m_s value, we can now compute the effective magnetic field B_{eff}^{j} experienced by nuclear spin j:

$$\mathbf{B}_{m_s}^{j} = \mathbf{B} \cdot \mathbf{g}^{j}(m_s) + m_s \mathbf{B}_{\text{dip}}^{j}. \tag{3.17}$$

In particular, this formula furnishes the effective magnetic fields $\mathbf{B}_0^{(j)}$ and $\mathbf{B}_1^{(j)}$ required to calculate the spin echo signal given in Equation (2) of the main text. We may also calculate the modulation frequency ($|\mu_n \mathbf{B}_1^{(j)}/\hbar|$) and find the remaining unknown term α_{zz} of the interaction tensor.

Fitting the data

The theoretical fits to the envelope and modulation frequencies shown in Fig. 3.7(B,C,D) are calculated from the following hyperfine interaction tensors. For NV E our fits are

derived from (in MHz):

$$\alpha^{(E)} = \begin{pmatrix} 5 & -6.3 & -2.9 \\ -6.3 & 4.2 & -2.3 \\ -2.9 & -2.3 & 8.2 \end{pmatrix}. \tag{3.18}$$

This hyperfine tensor implies a contact term

$$\mathrm{Tr}[\alpha^{(E)}]/3 = -\mu_e \mu_n 8\pi |\psi(\mathbf{r}^E)|^2/3 \approx 5.8 \text{ MHz} \tag{3.19}$$

which contributes significantly to the overall interaction strength $A_E = \sqrt{\mathrm{Tr}[(\alpha^{(E)})^2]/3} \approx$ 8.5 MHz. For NV D, our fits are calculated from (in MHz)

$$\alpha^{(D)} = \begin{pmatrix} 0.4 & -2.2 & -2.1 \\ -2.2 & 2.6 & -0.4 \\ -2.1 & -0.4 & 3.5 \end{pmatrix}. \tag{3.20}$$

Of this, contact provides

$$\mathrm{Tr}[\alpha^{(D)}]/3 = -\mu_e \mu_n 8\pi |\psi(r^j)|^2/3 = 2.2\text{MHz} \tag{3.21}$$

compared to $A_D \approx 3.6$ MHz.

Taking the above values for the hyperfine interaction tensor furnishes excellent fits to our data, indicating that our model can explain the phenomena we observe. However, the six parameters which characterize the hyperfine interaction tensor are highly covariant, and our data is insufficient to fully constrain all of them, i.e. good fits to our data can be obtained in a few distinct regions of parameter space. To obtain better constraints on the hyperfine interaction, a more detailed experimental study of the dependence of the envelope and modulation frequencies on magnetic field

orientation is necessary. With angular dependence in three dimensions, this technique should allow accurate determination of the full hyperfine interaction between the single NV center and a proximal ^{13}C spin.

Despite these considerations, our data does allow us to draw qualitative conclusions regarding the contributions of dipolar and contact terms to the hyperfine interaction. Pure point-dipole interactions between the electron and nuclear spin cannot account for our observations: assuming that the proximal ^{13}C spin must lie at least two lattice sites from the electron spin, the point-dipole model underestimates the observed interaction strength by a factor of $\sim$4. Conversely, the anisotropy in our data taken with the magnetic field in the $\hat{x} - \hat{z}$ vs $\hat{y} - \hat{z}$ planes cannot be explained by purely isotropic contact interactions. The two components must therefore both contribute to the total hyperfine interaction.

Chapter 4

Coherent manipulation of coupled single electron and nuclear spins

4.1 Introduction

Coherent manipulation of quantum solid state systems has been a subject of intense research in recent years. Despite the complex and often noisy environment in solid state devices, remarkable advances have been achieved in a variety of systems, ranging from superconducting islands[110] to quantum dots [47, 111, 112]. Single spin degrees of freedom [49, 107] present one of the most promising candidates because they can exhibit long coherence times even at room temperature [48, 113]. Here, we investigate a coupled spin system formed by a single electron spin and a nearby single nuclear spin in diamond. The nuclear spin provides a more stable qubit than the electron spin: It can survive long free precession intervals $\sim 500\mu$s or optical excitation, both of which dephase the electron spin. Using the coherent dipole interactions

between the spins, we show that electron spin states can be stored and retrieved from the nuclear spin. This robust quantum memory represents an important element of many quantum information schemes.

4.2 The coupled electron-nuclear spin system

The electron spin we observe is the spin triplet associated with a single nitrogen-vacancy (NV) defect in diamond. In the surrounding diamond lattice, 1.1% of the lattice sites are occupied by a spin-1/2 ^{13}C nucleus, which can couple to the NV electron spin via the spatially-dependent dipole interaction [106]. A sufficiently nearby ^{13}C nucleus can exhibit coherent interactions with the NV spin, creating the coupled electron-nuclear spin system we study.

A single NV center was isolated by a confocal microscope which excited the color center with 532nm light and detected its fluorescence into 650-800 nm (Fig. 4.1A). This optical excitation provides the means for both preparing and measuring the NV spin: 532nm light polarizes the electron spin into its ground state $|0\rangle$ on the time scale of $\tau_P \sim$ few hundred nanoseconds [90, 48]. On shorter timescales $t < \tau_P$, the fluorescence intensity depends on the spin state, with the states $|\pm 1\rangle$ fluorescing $\sim 20 - 40\%$ less than the ground state $|0\rangle$[107, 63]. We thus measure the spin state by comparing the short-time fluorescence intensity to the intensity observed for a polarized spin.

The NV electron spin can be readily manipulated by driving its spin transitions with near-resonant microwave excitation. In zero field, the ground state $|0\rangle$ is split off by 2.87 GHz, and application of a small magnetic field splits the states $|\pm 1\rangle$,

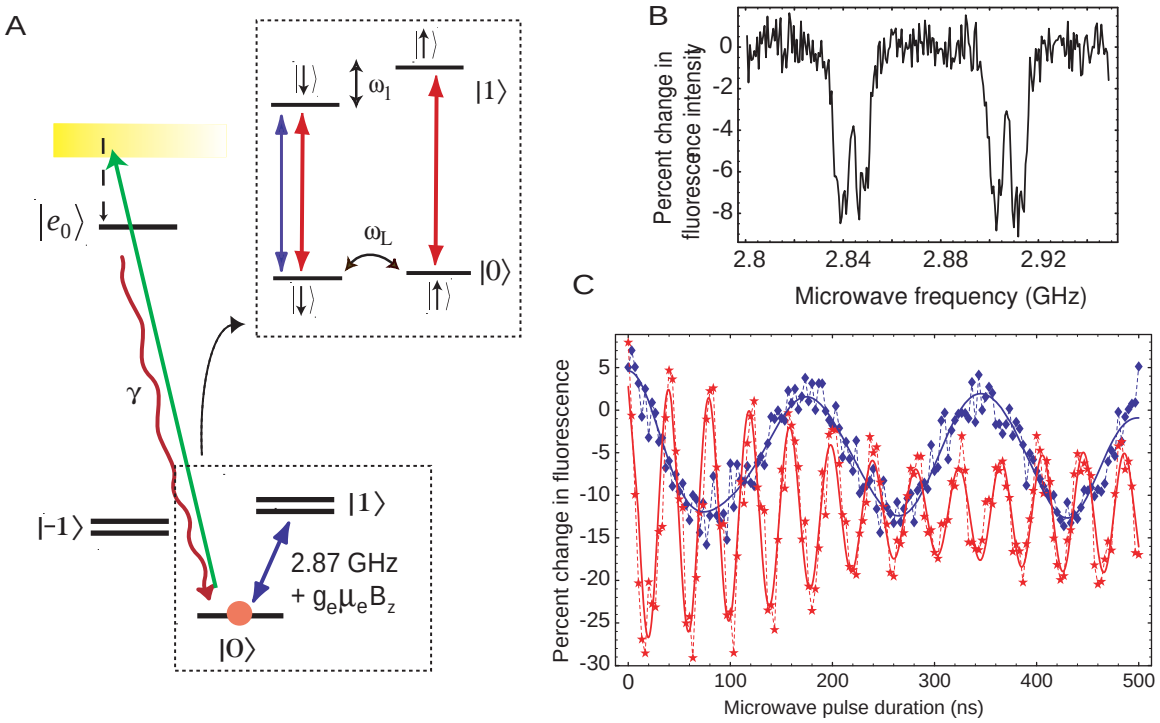

Figure 4.1: The coupled spin system formed by the NV electron spin and a nearby ^{13}C nuclear spin. (A) Level diagram for the coupled NV center - nuclear spin system. Optical transitions of the NV center are used to polarize and measure the electron spin state of the NV. A single electron spin transition $|0\rangle$ to $|1\rangle$ is addressed with resonant microwaves (blue arrow), and hyperfine structure associated with the ^{13}C spin states $|\uparrow\rangle, |\downarrow\rangle$ can be resolved within this transition. (Inset) Strong microwaves drive both hyperfine transitions (red arrows) whereas only one transition is driven by a weak microwave field (blue arrow) tuned to the lower hyperfine transition. (B) Optically detected magnetic resonance spectrum of spin transitions, including hyperfine structure. The ^{13}C nuclear spin splits the two ESR lines by 9 MHz. Within each ^{13}C hyperfine transition, a triplet is just barely resolved, which is associated with the 2.2 MHz hyperfine interaction with the $I = 1$ ^{14}N nuclear spin. (C) Electron spin nutations induced by weak (blue) and strong (red) microwaves have Rabi frequencies of 5.5 GHz and 24.6 GHz respectively.

allowing isolation of a single electron spin transition, $|0\rangle \rightarrow |1\rangle$. For the NV center studied, we observed a hyperfine structure within this transition, associated with spin states $|\uparrow\rangle, |\downarrow\rangle$ of a nearby ^{13}C nucleus (Fig. 4.1A, inset and Fig. 4.1B). This hyperfine splitting comes from the dipole field of the NV spin in its $|1\rangle$ state, and defines the quantization axis $\hat{n}$ of the nuclear spin. In the $|0\rangle$ state, the nuclear spin precesses around the weak external magnetic field, which is applied along a direction nearly perpendicular to $\hat{n}$. We note that a finer structure from the I = 1 ^{14}N host nuclear spin can also be observed in the spectrum. Since the ^{14}N spin orientation is pinned by a large quadrupole splitting [99], it contributes only a static level shift and does not qualitatively affect the system dynamics.

The applied microwave fields only excite electron spin transitions, leaving the nuclear spin state unchanged. Nevertheless, we can obtain some control over the system by selectively exciting the electron spin conditional on the state of the nuclear spin; this task is accomplished using weak microwave excitation, tuned to one of the hyperfine transitions. The resulting oscillations in the electron spin show only $\sim 1/2$ contrast, since half of the population is in the nuclear spin state unaffected by the microwaves. Driving both hyperfine transitions requires a strong microwave field with a Rabi frequency Ω_R greater than the hyperfine splitting ω_1; sufficiently strong microwave fields can drive full electron spin oscillations. In either case, we fit the Rabi nutation data to a model including both ^{13}C transitions and the weaker ^{14}N hyperfine structure (see Fig. 4.1C). This allows us to calibrate the fluorescence levels associated with $|0\rangle$ and $|1\rangle$, if we can assume that the initial optical polarization into $m_s = 0$ is perfect. All subsequent data is shown in units of p (where $p = 0$ and

$p = 1$ correspond to the $|1\rangle$ and $|0\rangle$ fluorescence levels respectively) obtained from Rabi nutations observed under the same conditions. Although these units may be considered as the population in $|0\rangle$, a more accurate interpretation is the population relative to the degree of polarization of the electron spin obtained under optical illumination.

4.3 Manipulating a single nuclear spin

We can effectively prepare, manipulate, and measure the electron spin using microwave and optical excitation. A similar level of control over the nuclear spin requires both manipulating the electron spin and using the hyperfine interaction to map between electron and nuclear spin states. For example, whereas we can polarize the electron spin into the state $|0\rangle$ by applying 532nm laser light, the nuclear spin starts out in an incoherent mixture of the states $|\uparrow\rangle, |\downarrow\rangle$. To polarize the nuclear spin, we must first map the nuclear spin state onto the electron spin, and then repolarize the electron spin (Fig 2A).

The pulse sequences used to control the electron-nuclear spin system rely on two effects: First, the hyperfine interaction introduces a splitting $\omega_1 \approx 9$ MHz between the nuclear spin states in the $m_s = 1$ manifold $\{|1,\downarrow\rangle, |1,\uparrow\rangle\}$, so we can selectively flip the electron spin state conditional on the nuclear spin. Second, if we apply a weak magnetic field perpendicular to the nuclear spin axis (as defined by diagonalizing the hyperfine interaction in $|1\rangle$), the nuclear spin precesses at the Larmor frequency ω_L when the electron spin is in $|0\rangle$, but remains frozen when the electron spin is in $|1\rangle$. The most frequently used pulse sequence, referred to as gate M, consists of a

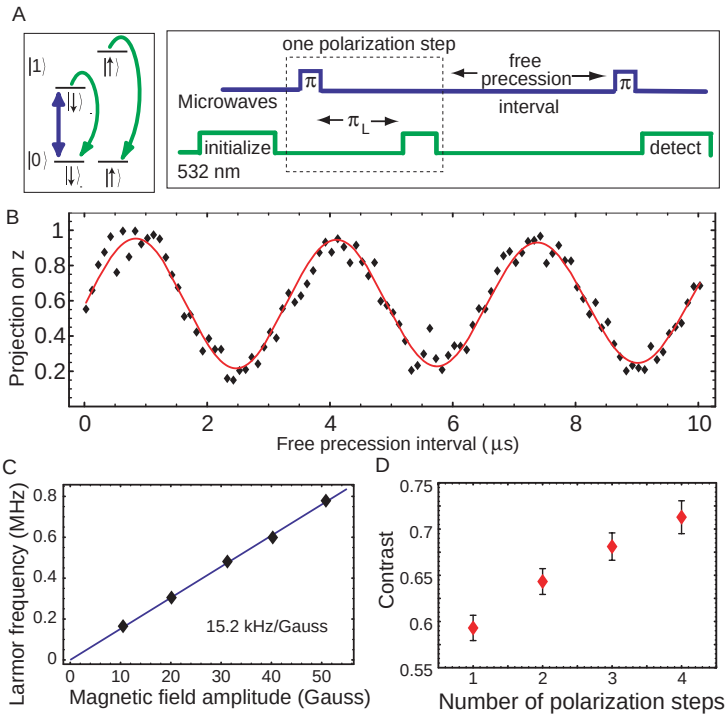

Figure 4.2: Free precession of a single nuclear spin. (A) Level diagram and pulse sequence used to prepare and measure the nuclear spin. The nuclear spin initially starts in a mixture of the states $|\uparrow\rangle, |\downarrow\rangle$, and the electron spin is initialized into the state $|0\rangle$. By mapping the nuclear spin state onto the electron spin state and optically pumping the electron spin back into $|0\rangle$, we create a nuclear spin polarization in $|\downarrow\rangle$. After a variable free precession interval, the nuclear spin is mapped back onto the electron spin state, and we measure the electron spin. (B) Nuclear free precession. In a ~ 20 Gauss magnetic field oriented perpendicular to the NV axis, the nuclear spin oscillates between $|\uparrow\rangle$ and $|\downarrow\rangle$ every 3.3μ s. (C) Observed nuclear spin precession frequency (Larmor frequency) as a function of magnetic field, approximately oriented along $\hat{x} - \hat{z}/4$, where $\hat{z}$ is the NV axis. (D) By increasing the number of polarization steps (dash-boxed pulse sequency in (A)), a higher contrast for the nuclear free precession signal is obtained. Four polarization steps were used for the data shown in (B).

microwave π pulse followed by a waiting time $\tau = \pi/\omega_L$ (abbreviated π_L). This gate has the effect of mapping a nuclear spin superposition $|0\rangle \otimes (\alpha\,|\downarrow\rangle + \beta\,|\uparrow\rangle)$ onto an electron spin superposition $|\downarrow\rangle \otimes (\alpha\,|1\rangle + \beta\,|0\rangle)$. The weak microwave π pulse is tuned to one hyperfine transition, mapping $|0,\downarrow\rangle \rightarrow |1,\downarrow\rangle$ while leaving $|0,\uparrow\rangle$ unaffected. Waiting for half of a Larmor period, π_L, swaps the states $|0,\uparrow\rangle$ and $|0,\downarrow\rangle$ while leaving the nuclear spin in $|1\rangle$ unaffected.

4.3.1 Nuclear free precession

By combining the mapping gate with electron spin polarization and measurement, we have observed free precession of a single nuclear spin (Fig. 4.2B). The nuclear spin is prepared in the state $|0,\downarrow\rangle$ by repeated application of the polarization sequence, M-G, where M is the mapping gate and G is a pulse of 532nm light sufficient to repolarize the electron spin into $|0\rangle$. After a variable precession time, the nuclear spin state is again mapped onto the electron spin, and the electron spin state is measured via its state-selective fluorescence. The Larmor precession frequency of the nuclear spin (Fig. 4.2C) is enhanced above its bare value of 1.07 kHz/G by interactions with the electron spin, as discussed in the previous chapter[113]. The contrast of the free precession signal increases with the number of polarization steps, and the observed contrast of $\sim 70\%$ indicates that we prepare the nuclear spin state with a fidelity greater than 85%.

4.3.2 Phase rotations

The free precession signal shows oscillations between $|\uparrow\rangle$ and $|\downarrow\rangle$ arising from rotations of the nuclear spin around the applied magnetic field (which is nearly perpendicular to the nuclear spin quantization axis $\hat{n}$). Complete control of the nuclear spin state can only be achieved if we can also manipulate the phase between the nuclear spin states $|\uparrow\rangle$ and $|\downarrow\rangle$. This can be done by exciting the electron spin into the $m_s = 1$ manifold and waiting for a time τ, during which the nuclear spin state $|\uparrow\rangle$ picks up a phase $e^{-\omega_1 \tau}$ with respect to $|\downarrow\rangle$. To perform this Z-rotation (so named because it corresponds to a rotation around the nuclear spin axis), we must apply a strong, unselective π pulse (designated π_U) that excites both nuclear spin states to the $m_s = 1$ manifold, wait for a time τ, and apply another strong π_U pulse to return the system to the $m_s = 0$ manifold.

We have observed phase rotations of the nuclear spin, as shown in Fig. 4.4. For these experiments, we prepare the system in $|\downarrow\rangle|0\rangle$ using the polarization sequence M-G, and then wait for a time $\pi_L/2$ during which the nuclear spin precesses into the state $\frac{1}{\sqrt{2}}(|\downarrow\rangle + i|\uparrow\rangle)|0\rangle$. Application of the Z-rotation sequence $\pi_U - \tau - \pi_U$ adds a phase to $|\uparrow\rangle$, leaving the system in $\frac{1}{\sqrt{2}}(|\downarrow\rangle + ie^{-i\omega_1\tau}|\uparrow\rangle)|0\rangle$. Waiting for $\pi_L/2$ converts the phase into nuclear spin population, so the system ends up in the state $\frac{1}{2}((1 - e^{-i\omega_1\tau})|\downarrow\rangle + i(1 + e^{-i\omega_1\tau})|\uparrow\rangle)|0\rangle$. Finally, by mapping the nuclear spin state onto the electron spin (with a weak, selective microwave π pulse), we can observe oscillations at the hyperfine frequency ω_1.

This technique allows us to indirectly drive nuclear spin transitions between the $m_s = 0$ eigenstates $|\pm\rangle \approx \frac{1}{\sqrt{2}}(|\downarrow\rangle \pm |\uparrow\rangle)$. In particular, by performing a Z-rotation

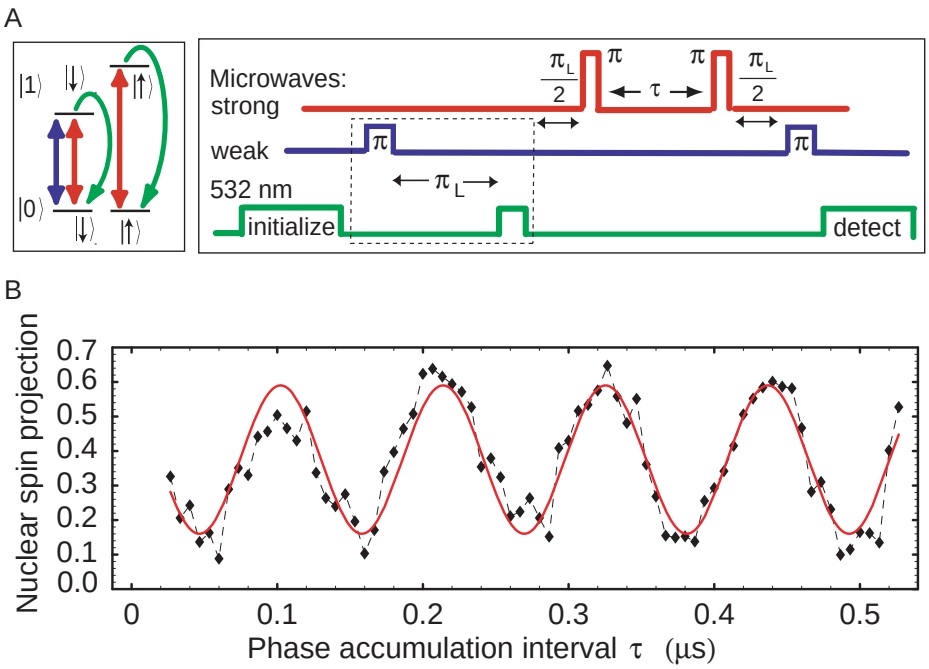

Figure 4.3: Z-rotations for the nuclear spin. (A) Pulse sequence used to observe Z-rotations. Weak (blue) and microwaves are used for nuclear spin polarization and measurements, whereas strong (red) microwave pulses are used to implement Z-rotations. Both microwave sources are resonant with the $|0,\downarrow\rangle \rightarrow |1,\downarrow\rangle$ transition, and they have Rabi frequencies of ≈ 6 and ≈ 20 MHz respectively. (B) Nuclear spin projection showing oscillations at the hyperfine frequency $\omega_1 = (2\pi)$ 9 MHz.

with delay $\tau = \pi/\omega_1$, we can implement a π_n-pulse between these eigenstates, allowing us to perform spin-echo experiments on the nuclear spin.

For both the nuclear spin Z-rotations and nuclear spin echo experiments, the observed contrast decreases relative to the nuclear spin free precession signal. Typical data show $\sim 40\%$ contrast for Z-rotations and nuclear spin echo. The reduced contrast arises from several sources, including incomplete population transfer from $m_s = 0$ to $m_s = 1$ and accidental excitation of the $m_s = -1$ manifold during the strong microwave π_U pulses, an applied magnetic field which is not completely perpendicular

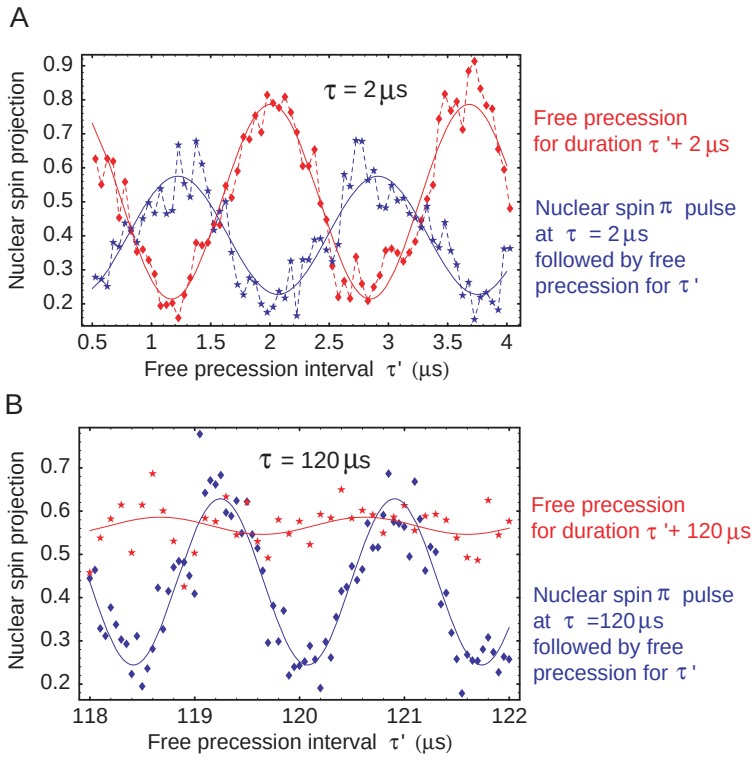

Figure 4.4: Spin-echo for the nuclear spin. The red trace shows free precession during time interval $\tau + \tau'$, whereas the blue trace shows the spin echo obtained by applying a nuclear spin π_n pulse after time $\tau = 2\mu$s and then scanning τ'. Note that the spin-echo signal at $\tau = \tau'$ shows a minimum in the nuclear spin projection. For this data, the time $\tau = 2\mu$s is chosen so that the nuclear π_n pulse reverses the orientation of the nuclear spin.

to the $\hat{n}$ nuclear axis, and timing errors generated by the 3.3ns minimum pulse width and 21ns minimum delay in our pulse generator. Although the low contrast precludes high-fidelity manipulation of the nuclear spin phase, it is sufficient to perform spin-echo experiments, for which only the relative contrast at different delays matters.

4.4 Coherence properties of the nuclear spin

4.4.1 Nuclear spin dephasing

In comparison with the electron spin, which dephases on a timescale $T_{2e}^{*} \sim 2\mu$s, the nuclear spin free precession signal persists out to nearly a millisecond; a fit to Gaussian decay yields a dephasing time $T_{2n}^{*} = 495 \pm 30\mu$s (Fig. 4.5). The enhancement in T_2^{*} is consistent with the ratio of the electron and nuclear gyromagnetic ratios, $\gamma_e/\gamma_n \sim 200$, suggesting that a similar improvement may be expected for the coherence times. Since the electron spin coherence time is more than 100x its dephasing time, a nuclear spin coherence time ~ 10 ms may thus be possible.

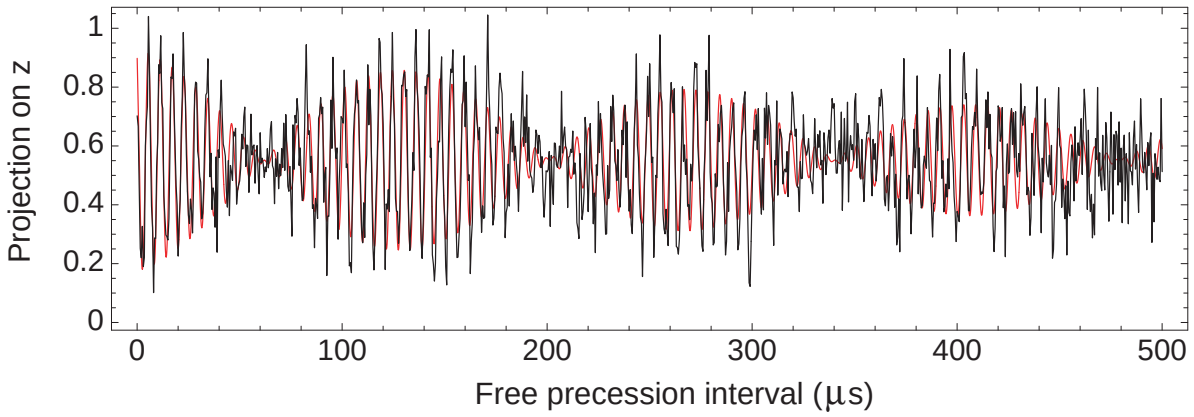

Figure 4.5: Free precession of a single nuclear spin out to 0.5 ms, showing beating and decay. The Gaussian decay time is $\sim 490 \pm 30\mu$s, while modulation with a period of $277 \pm 2\mu$s shows that the nuclear spin interacts coherently with another quantum system.

4.4.2 Nuclear spin-echo

Using the Z-rotation sequence, we can perform spin-echo experiments on a single nuclear spin to determine its coherence time T_{2n}. Because of the way in which we map the nuclear spin back onto the electron spin for measurement (see Fig. 4.6A), the spin-echo creates a minimum in the observed fluorescence when the two free precession periods are equal $\tau = \tau'$. We have measured the nuclear spin-echo out to $\tau + \tau' = 2$ms, as shown in Fig. 4.6, and see no observable decay.

Because the signal-to-noise ratio in our experiments is fairly low, we need to average $\sim 100,000$ runs of the experiment to obtain typical data sets. While this requirement presents no difficulty for short experiments, such as Rabi nutations, it becomes increasingly difficult to measure time dependences past ~ 1 ms, where $100,000$ runs requires 100 seconds per point. Measurement of the nuclear spin T_2 will thus require qualitative changes in our experimental setup, either by using better fluorescence collection techniques (for example a solid immersion lens or cavity) or by working at low temperatures, where single-shot readout of the spin state is possible [87].

4.4.3 Interactions with other nuclear spins in the bath

The free precession signal shown in Fig. 4.5 exhibits a characteristic beating behaviour, and the Fourier transform of the precession signal shows two components split by ~ 3.6 kHz. In contrast, no oscillations show up in the spin-echo signal (Fig. 4.6B), and this is confirmed by the Fourier transform of the echo shown in Fig. 4.7.

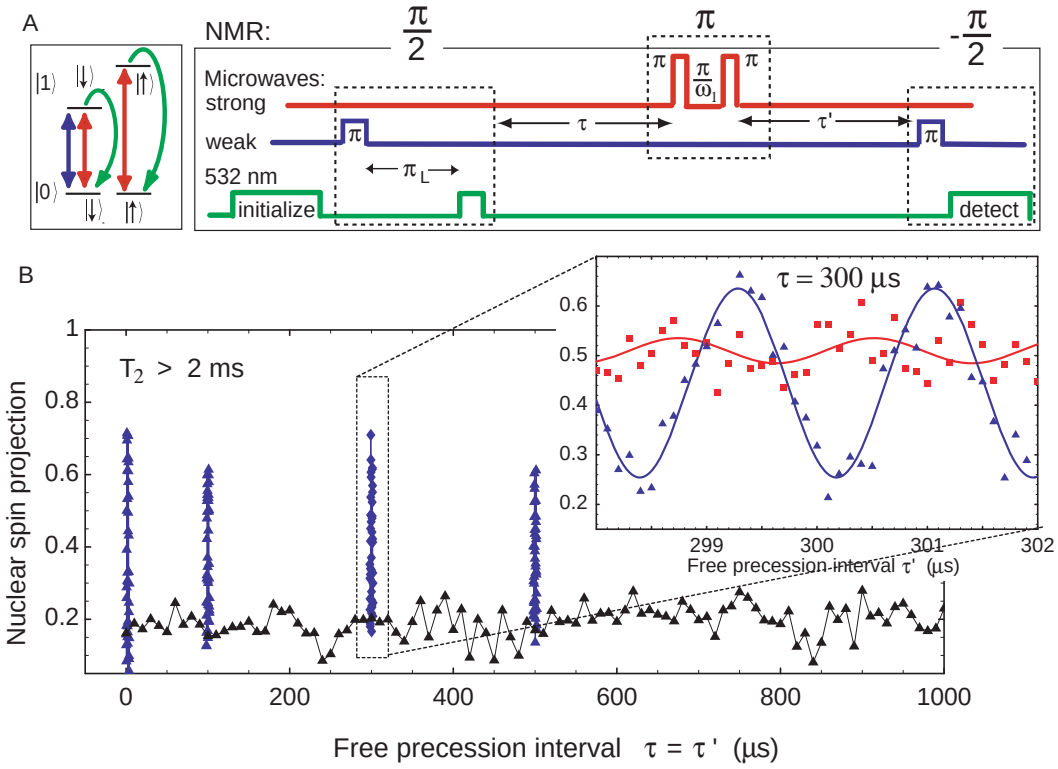

Figure 4.6: Spin-echo for a single nuclear spin. (A) The pulse sequence used to implement nuclear spin echo. (B) The nuclear spin-echo signal obtained by scanning $\tau = \tau'$ simultaneously, mapping out the minimum in the spin-echo, shows no decay out to $\tau + \tau' = 2$ ms. (Inset) A sample nuclear spin-echo (blue) taken for $\tau = 300\mu$s with τ' scanned from 298μs to 302μs. The red curve shows the free precession signal obtained by eliminating the nuclear π pulse in the sequence shown in (A).

The beating in the free precession signal can be explained by coupling of the nuclear spin I to another ^{13}C nuclear spin J in the diamond lattice. The strength of the coupling ~ 3.6 kHz is much stronger than the bare dipole-dipole interaction strength ($\sim$ 1.7kHz for nearest neighbors), indicating that the nuclear spin interactions are mediated by the presence of the NV electronic spin. However, for the data shown in Fig. 4.5, the nuclear coupling is weaker than the Zeeman splitting for even a bare

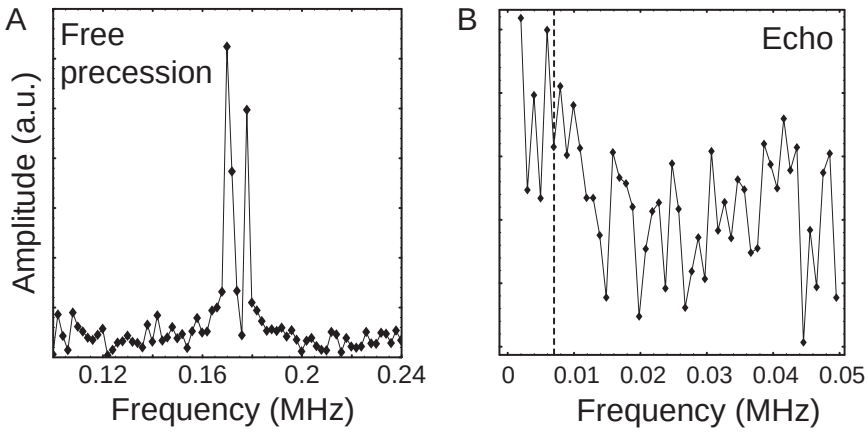

Figure 4.7: (A) Fourier transform of the nuclear free precession curve shown in Fig. 4.5. (B) Fourier transform of the $\tau = \tau'$ echo signal shown in black in Fig. 4.6B. The dotted line shows the location of the 3.6 kHz splitting observed in (A).

^{13}C nuclear spin $g_n \mu_n B \sim 11$ kHz, so the interactions cannot flip either nuclear spin. Weak coupling to a second nuclear spin thus only introduces a static splitting in the level structure of the first nuclear spin I, which disappears upon application of a spin-echo sequence. The second nuclear spin J must lie relatively far from the NV spin, since it does not show up in CW or spin-echo spectroscopy of the NV electron spin. This weak coupling to the NV spin does not lead to significant evolution of spin J during the π pulse on spin I, so the spin-echo pulse sequence succeeds in reversing the effect of spin J on the evolution of nuclear spin I. Consequently we do not observe any oscillations in the spin-echo signal from nuclear spin I.

4.5 Storage and retrieval of electron spin states

The nuclear spin exhibits a slow dephasing rate, which can be extended with an echo sequence, making it a robust quantum bit. To show that the nuclear spin can also serve as a quantum memory, we have stored and retrieved electron spin states (Fig. 4.8). After polarizing the nuclear spin, we create an electron spin state in one of three bases, $\{X_\pm = 1/\sqrt{2}\left(|0\rangle \pm |1\rangle\right), Y_\pm = 1/\sqrt{2}\left(|0\rangle \pm i\,|1\rangle\right), Z_{0,1} = \{|0\rangle, |1\rangle\}\}$. The electron spin is then stored in the nuclear spin using M^{-1}, where it is allowed to remain for a time $(2N+1)\pi_L$ before retrieval via M. We then observe the remaining coherence (for X or Y storage) or population (for Z storage) by driving electron spin nutations and recording their contrast relative to nutations of a fully polarized electron spin. For data shown in Fig. 4.8B, N = 0, corresponding to a total time of $3\pi_L \sim 2.4\mu\text{s} > T_{2e}^*$ between creation of the electron spin state and measurement. The overall fidelity of the memory is $F = (1+\langle C\rangle)/2$, where $\langle C\rangle$ is the average contrast for the six measurements; we find $F = 75 \pm 1.3\%$, which exceeds the limit for a classical memory of $F_c = 2/3$[1].

At first glance it may appear impossible to store an electron spin state using a mapping gate which takes a time π_L that is similar to the electron spin dephasing time T_{2e}^*. In fact, the pulse sequence used for storage and retrieval corrects for electron spin dephasing during the mapping gates. Because different components of the state are put into electron spin excited state $|1\rangle$ in the storage and retrieval steps (see Fig. 4.8A), both components pick up the same random phase associated with the

[1]It is worth noting that the fidelity for the memory is not affected by imperfect polarization of the electron spin. Even if we do not prepare a perfect electron spin state initially, the relative contrast of Rabi oscillations before and after storage reveals the fidelity of the memory.

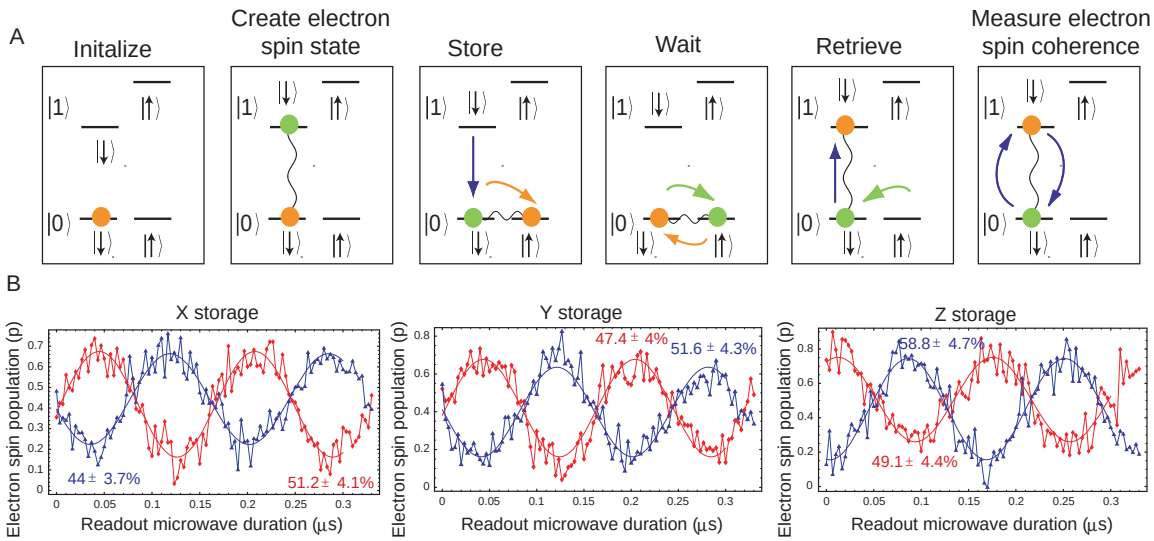

Figure 4.8: Storage of electron spin coherence in a single nuclear spin. (A) Experimental sequence. The system is polarized into a single nuclear spin state, and an electron spin state is created by appopriate microwave pulses. The electron spin state is then mapped onto the nuclear spin, where it precesses at the nuclear Larmor frequency before it is mapped back to the electron spin. The remaining population and coherence in the electron spin state is read out by driving microwave transitions. (B) Observed electron spin nutations after storage of different electron spin states. X storage refers to storage of the electron spin state $1/\sqrt{2}(|0\rangle \pm |1\rangle)$, Y storage is $1/\sqrt{2}(|0\rangle \pm i\,|1\rangle)$, and Z storage measures the population storage, $\{|0\rangle, |1\rangle\}$.

quasi-static environment of the electron spin. Relying on equal random phases means that the retrieval step will only work if the environment is in the same state as it was during the storage step, limiting the overall storage time to the electron spin coherence time $T_2 \sim 240\mu$s. This is not, however, a fundamental limit: we could eliminate the random phase entirely by working with a stronger magnetic field with $\pi_L \ll T_{2e}^*$. In practice, such an approach could only work with a pulsed magnetic field, as discussed below.

The observed memory fidelity is limited by several factors which could be greatly

improved by dynamic magnetic field control and other technical improvements. Errors in the mapping gate arise from additional hyperfine structure associated with ^{14}N nuclear spin and undesired Larmor precession of the ^{13}C spin during the microwave pulse. Further error is introduced by nuclear spin precession and bright decay during the optical illumination step G. Finally, the effective magnetic field experienced by the nuclear spin in the $|0\rangle$ state is not precisely perpendicular to the effective field in the $|1\rangle$ state because of misalignment and residual effects of the applied field in the $|1\rangle$ state. The first two sources of error could be eliminated by turning the magnetic field off during microwave and optical excitation, and using microwave pulse-shaping techniques to drive all three ^{14}N transitions. Although it could likely be improved by careful field alignment, the final source of error has a fundamental limit set by the ratio of the effective applied magnetic field to the electron spin dipolar field. For our experiments this ratio is $\sim 1 - 5\%$, depending on the magnetic field. Further improvements would require either working at lower magnetic fields, using a more strongly coupled NV-^{13}C pair, or both.

4.6 Dephasing in the presence of laser light

The nuclear spin becomes a particularly powerful tool for quantum memory if it is possible to couple the electron spin to light without affecting the nuclear spin. For example, the solid-state quantum repeater scheme discussed in Chapter 5 relies on a quantum memory which is robust enough to survive many attempts to probabilistically entangle the electron spin with a photon state. Although we have not yet attempted spin-photon entanglement, we can obtain some measure of the robustness

of the nuclear spin qubit by observing its dephasing during optical polarization of the electron spin, which is a necessary ingredient of any probabilistic spin-photon entanglement scheme.

To investigate the dephasing of the nuclear spin in the presence of laser light, we have observed how the contrast of the free precession signal decays after light pulses of increasing duration. We find that, under optical illumination, the nuclear spin dephases much more slowly than the electron spin polarizes (Fig. 4.9A). Furthermore, this illuminated decay rate depends on the magnetic field (Fig. 4.9B), indicating that greater control over the nuclear spin dephasing rates may be possible in systems with switchable magnetic fields.

The dependence of the bright decay rate on the magnetic field can be qualitatively understood as arising from different Larmor precession rates in the ground and optically excited states. The nuclear gyromagnetic ratio is strongly enhanced by hyperfine interactions with the electron spin, and the strength of this enhancement depends on the electron spin spatial distribution. Orbitally excited electron states, which have different wavefunctions, thus have different nuclear gyromagnetic ratios. Under optical illumination the nuclear spin makes transitions between electron spin states with different precession rates, and dephases at a rate proportional to the change in precession frequency. In high magnetic fields, it requires less time for the difference in precession rates to become apparent and dephase the nuclear spin; by moving to lower magnetic fields, the dephasing can be reduced.

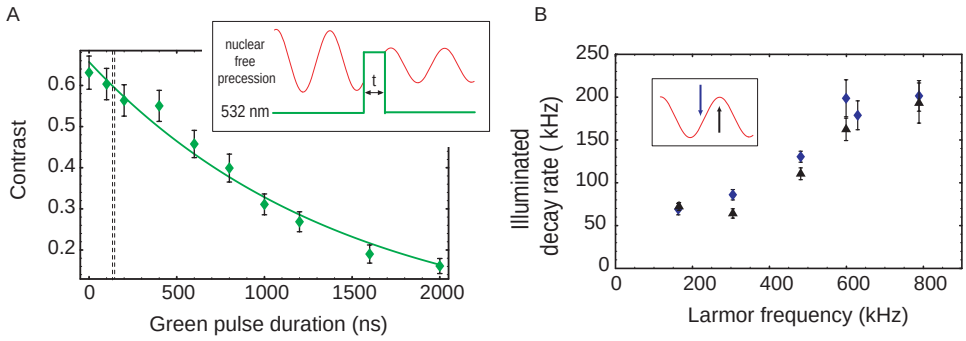

Figure 4.9: Bright dephasing of single nuclear spin free precession. (A) Bright decay. Application of 532nm light during the nuclear free precession interval (illustration in inset) reduces the contrast of the free precession signal. When illuminated by 320μW (approximately half the saturation intensity for the NV optical transition), the nuclear spin signal decays on a timescale of $1.5 \pm 0.1\mu$s. This data is taken in a magnetic field of $\sim$ 30 G, corresponding to a Larmor period of $\sim$ 2.1μs. For comparison, the polarization rate for the electron spin (under the same conditions) is 140 ± 6ns, shown by the dashed lines. (B) Bright decay vs magnetic field. Bright decay rates were found for several magnetic fields, showing that the decay rate scales with the Larmor precession frequency for the nuclear spin. 320μW light was used for all data sets. The decay rate does not depend strongly on whether we apply green light when the nuclear spin is in its polarized state $|\downarrow\rangle$ (black points) or in a superposition state $1/\sqrt{2}(|\uparrow\rangle + |\downarrow\rangle)$ (blue points), as illustrated in the inset.

4.7 Conclusion

We have observed a single isolated ^{13}C nuclear spin in the vicinity of a single NV center in diamond, demonstrating that it represents a robust quantum memory for information encoded in the NV electron spin. Such a robust quantum memory may provide an integral component for optical connections between quantum nodes, which play an important role in many scalable quantum information and quantum communication schemes. One such scheme is discussed in the following chapter.

Chapter 5

Long distance quantum communication with minimal physical resources

The previous chapters dealt with optical and spin properties of the nitrogen-vacancy center in diamond. This chapter discusses a possible application for the nitrogen-vacancy center – or any other system possessing similar properties – in long-distance quantum communication. Three aspects of the NV center make it attractive as a candidate for a quantum repeater node: first, it has a spin degree of freedom with a long coherence time; second, its spin degree of freedom can be coupled to an auxiliary (nuclear) spin; third, it is a single photon emitter with promise of spin-dependent optical transitions. This relatively simple physical system forms the basis for a new scheme for fault-tolerant quantum communication with minimal requirements on physical resources.

5.1 Introduction

Quantum communication holds promise for transmitting secure messages via quantum cryptography, and for distributing quantum information [55]. However, exponential attenuation in optical fibers fundamentally limits the range of direct quantum communication techniques [114], and extending them to long distances remains a conceptual and technological challenge.

In principle, the limit set by photon losses can be overcome by introducing intermediate quantum nodes and utilizing a so-called quantum repeater protocol [56]. Such a repeater creates quantum entanglement over long distances by building a backbone of entangled pairs between closely-spaced quantum nodes. Performing an entanglement swap at each intermediate node [115] leaves the outer two nodes entangled, and this long-distance entanglement can be used to teleport quantum information [116, 117] or transmit secret messages via quantum key distribution [118]. Even though quantum operations are subject to errors, by incorporating entanglement purification [119, 120] at each step, one can extend entanglement generation to arbitrary distances without loss of fidelity in a time that scales polynomially with distance [56]. This should be compared to direct communication, which scales exponentially, making it impractical for long distances.

Several approaches for physical implementation of a quantum repeater protocol have been proposed. Early work was based on systems of several atoms trapped in high finesse optical cavities [121, 38, 34]. Such systems can form a quantum network with several quantum bits (qubits) per node, and are particularly suitable for efficient implementation of the pioneering proposal of Ref. [56]. In this approach,

quantum communication over thousand kilometer distances requires approximately seven quantum bits per node, which must be coherently coupled to perform local quantum logic operations, i.e. a seven qubit quantum computer. The specific implementation of these early ideas involved the techniques of cavity QED for interfacing stationary and photonic qubits and for performing the necessary quantum logic operations [122, 123]. Recent related work pointed out that long-distance entanglement can be implemented via probabilistic techniques without the use of ultra-high finesse cavities [38, 34], while local operations can be accomplished via short-range interactions involving e.g. interacting trapped ions. However, few-qubit registers are still technically very difficult to construct, and the difficulty increases drastically with the number of qubits involved. At the same time, a novel approach based on photon storage in atomic ensembles [32] and probabilistic entanglement is also being actively explored. In comparison with systems based on many-qubit nodes, this approach offers less error tolerance and requires a longer communication time. Realization of a robust, practical system that can tolerate all expected errors remains therefore a challenging task.

In a recent paper [96] we proposed a quantum repeater protocol which could be implemented using the electronic and nuclear degrees of freedom in single photon emitters. Here we present further details of the proposal described in Ref. [96], and we compare our methods to alternative strategies. We show that our repeater protocol requires only two effective quantum bits at each node. This is the minimum requirement on physical resources which still allows active error correction. As a specific implementation, we consider nodes formed by a single quantum emitter with two in-

ternal degrees of freedom. A pair of electronic spin sublevels allows for state-selective optical excitation (see inset in Figure 1a), and a proximal nuclear spin provides an auxiliary memory. State-selective fluorescence is used for probabilistic entanglement generation between electronic spin degrees of freedom. We analyze in detail and compare several approaches for probabilistic entanglement generation, focussing on the feasibility of their implementation using realistic photon emitters. Once electronic spin entanglement is generated, the coupled electron and nuclear spin at each node can be used to efficiently implement entanglement swapping and purification. We show that these techniques can be combined to generate high-fidelity entanglement over arbitrarily long distances. We present a specific protocol that functions in polynomial time and tolerates percent-level errors in entanglement fidelity and local operations.

Our approach is stimulated by recent experimental progress in single photon generation by means of single quantum emitters, including atoms and ions as well as impurities and nanostructures in solid state devices. Although our approach is relevant to atomic systems, such as single atoms trapped in a cavity [25] or single trapped ions [34], it is particularly suitable for implementation with solid-state emitters, for example impurity color centers [76, 77] and quantum dots [124, 42]. These devices offer many attractive features including optically accessible electronic and nuclear spin degrees of freedom, potential opto-electronic integrability, and fast operation.

The chapter is organized as follows. First, we will discuss techniques for entanglement generation. For clarity, we will present our results in the context of nitrogen-vacancy (NV) centers in diamond, and discuss alternative implementations at the end.

Realistic imperfections, such as homogeneous broadening and limited selection rules, motivate a novel entanglement generation scheme based on state-selective Rayleigh scattering and interferometry. We calculate the success probability and entanglement fidelity for this scheme as implemented in NV centers, and compare this scheme to alternative schemes based on Raman scattering or optical π pulses, with success conditioned on detection of one or two photons. Next, we will show how hyperfine coupling between the electron spin and proximal nuclei permits entanglement swapping and purification. Performing these operations in parallel and employing a nesting scheme, we calculate the fidelity obtained and the time required to generate it as a function of distance. In addition, we compare this scheme to the pioneering proposals [56, 32] for fault-tolerant quantum repeaters. Finally, we quantitatively discuss the feasibility of implementing a quantum repeater using NV centers, and elucidate alternative material systems which satisfy the requirements of our technique.

5.2 Entanglement generation

The initial step in our scheme is entanglement generation between the electron spins of two emitters separated by a distance L_0. In principle, entanglement can be generated probabilistically by a variety of means, e.g., Raman scattering [31, 122, 125] or polarization-dependent fluorescence [34]. However, solid-state emitters often do not exhibit appropriate selection rules, and for our repeater protocol it is essential that the optical transition be independent of the nuclear spin state. Specifically, as illustrated below, solid state emitters do not always allow Raman scattering or polarization-dependent fluorescence which fulfills the latter requirement. We therefore consider

an entanglement mechanism based on state-selective elastic light scattering as shown in Figure 1. Elastic light scattering places few restrictions on selection rules, and permits nuclear-spin-independent fluorescence as we discuss below.

5.2.1 Properties of single color centers

Our entanglement generation scheme is applicable to a wide variety of physical systems, requiring only the simple level structure illustrated in Fig. 5.1a. For clarity, we will present it first using a concrete example: the nitrogen-vacancy (NV) center in diamond, which has the specific level structure shown in Fig. 5.2. This example illustrates many generic features common to other solid-state emitters.

NV centers represent a promising physical system because of their strong optical transition around 637 nm and optically accessible electron spin states. In particular, the ground state (A_1 symmetry class of the C_{3v} group) has three electronic spin-states which we label $|-1\rangle$, $|0\rangle$ and $|1\rangle$ according to their spin angular momentum along the symmetry axis of the defect (M_s). Spin-orbit and spin-spin effects lead to a splitting of $|0\rangle$ from $|\pm 1\rangle$ by 2.87 GHz. Since we only require two electronic spin states, $|0\rangle$ and $|1\rangle$, we isolate these two states from the $|-1\rangle$ state by either adding a small magnetic field to shift the energy of the $|\pm 1\rangle$ state, or by using appropriately polarised ESR-pulses. As spin-orbit and spin-spin effects are substantially different for the optically excited state (E symmetry class), the strong transition from the $M_s = 0$ sublevel of the ground orbital state can be excited independently of the other M_s states. Although there is evidence for photo-bleaching at low temperatures, current models indicate that crossover into the dark metastable state occurs primarily from

the $M_s = \pm 1$ excited states [84, 63]. Furthermore, crossover into the trapping state is a detectable error. In the repeater protocol described below we perform a series of measurements on the electronic spin. During these measurements, the dark state will not produce any fluorescence, revealing the error. Shelving into the metastable state will thus influence the time (see Appendix C) but not the fidelity associated with the repeater protocol. Consequently, we assume that we are only near resonance with a single state $|e\rangle$ which has $M_s = 0$, and neglect photo-bleaching effects.

The electron spin degree of freedom suffices to generate entanglement between adjacent NV centers. To propagate entanglement to longer distances, we will make use of an auxiliary nuclear degree of freedom $\{|\uparrow\rangle, |\downarrow\rangle\}$ which will be used for storage of quantum information during the repeater protocol. In NV centers, this nuclear degree of freedom can arise from a nearby carbon-13 impurity or directly from a nitrogen-15 isotope forming the center. The large energy separation between the $|0\rangle$ and $|\pm 1\rangle$ states exceeds the hyperfine interaction by an order of magnitude, decoupling the nuclear and electronic spins. The energy levels can thus be described by product states of the two degrees of freedom. Furthermore, in states with $M_s = 0$, the energy is independent of the nuclear state, resulting in the optical transition between $|0\rangle$ and $|e\rangle$ being disentangled from the nuclear spin state. In the $|1\rangle$ state there is a strong hyperfine interaction between the electronic and nuclear spin state. By multiplexing two ESR pulses of different frequencies when doing the operations on the electronic spin and using RF-NMR pulses for the manipulation of nuclear spin states, see Figure 5.2, the hyperfine splitting can be compensated for by going to a rotating frame. Consequently, the nuclear spin can be used to store entanglement

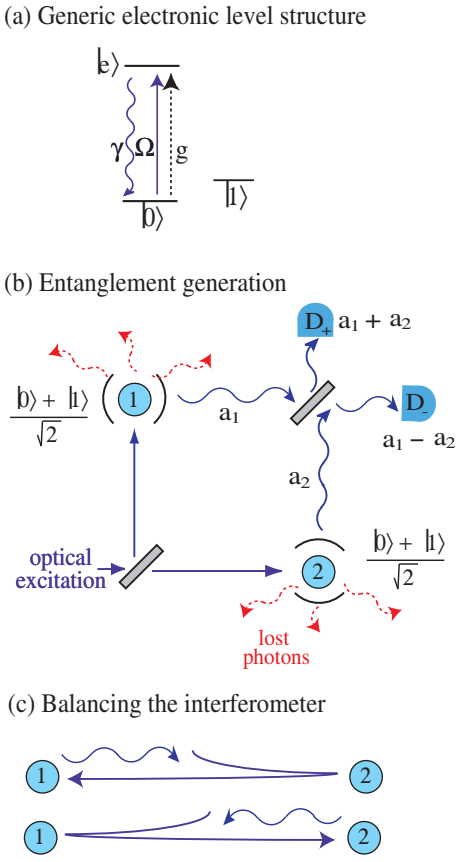

Figure 5.1: *(a) Generic level structure showing the state-selective optical transitions and electronic spin sublevels required for entanglement generation. (b) Setup used to create entanglement. The two emitters act as state dependent mirrors in an interferometer. The outputs of the cavities (a_1 and a_2) are combined on a beamsplitter. By proper alignment of the interferometer the photons always exit through the $(a_1+a_2)/\sqrt{2}$ port if both centers are in the scattering state $|0\rangle$. A detection of a photon in the $(a_1 - a_2)/\sqrt{2}$ mode thus leads to an entangled state. (c) Scheme for balancing the interferometer. Each node is optically excited by a laser pulse which first reflects off the other node, so that the optical path lengths for the two excitation/emission paths are identical.*

while the $|0\rangle - |e\rangle$ transition is used to generate another entangled pair of electron spins.

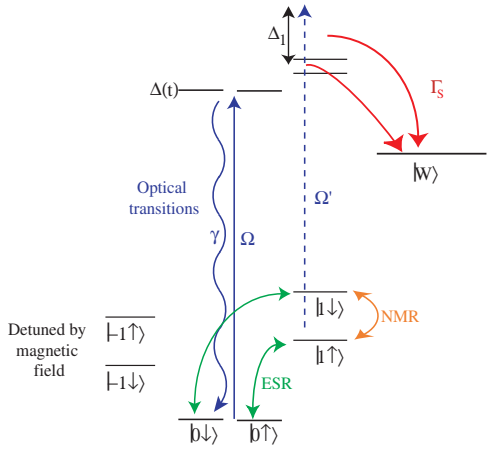

Figure 5.2: *The relevant electronic and nuclear states of the coupled NV center and* ^{13}C *impurity nuclear spin. The electron spin states can be coupled by ESR microwave fields near* 2.87 *GHz, while the nuclear spin states can be addressed by NMR pulses on the* 130 *MHz hyperfine transition. A laser applied on resonance with the* $M_s = 0$ *optical transition produces strong fluorescence for the entanglement scheme; but it only weakly excites the* $M_s = \pm 1$ *transitions, because of the large detuning* Δ_1*. The optically excited* $|M_s = 0\rangle$ *state decays at a rate* γ *and the optical transition has an inhomogeneous broadening* Γ *caused by fluctuations* $\Delta(t)$ *in the energy of the excited state. In our model we also assume that only the* $M_s = \pm 1$ *states decay to the shelving state* $|W\rangle$ *at rate* Γ_S*.*

5.2.2 Entanglement protocol

To implement the entanglement scheme, each NV center is placed inside a photonic cavity, whose output is coupled to a single-mode photonic fiber (note, however, that cavities are not essential for this proposal, see below). Fibers from adjacent NV centers enter two ports of a beamsplitter, and entangled electron spin pairs are obtained conditional on detection of a photon in an outgoing arm of the beamsplitter

(see Figure 1b).

Specifically, our protocol for entanglement generation relies on scattering on the closed optical transition between $|0\rangle$ and $|e\rangle$. This scattering does not change the state of the NV center; the centers essentially act as mirrors reflecting the light only if they are in the state $|0\rangle$. We assume that each of the centers is initially prepared in the state $(|0\rangle + |1\rangle)/\sqrt{2}$, so that the total state is

$$|\Psi_{\text{ini}}\rangle = \frac{1}{2}(|00\rangle + |11\rangle) + \frac{1}{2}(|01\rangle + |10\rangle). \tag{5.1}$$

Since there is no light scattering from state $|1\rangle$, we can exclude the $|11\rangle$ component if we detect any scattered photons. In state $|00\rangle$, both centers act as mirrors, so that by balancing the interferometer in Fig. 5.1 (b) we can arrange for the photons to leave through a specific port D_+ . A photon detection in the opposite port D_- can thus only arise from the $|01\rangle$ and $|10\rangle$ states and produces an entangled superposition of these two states.

Balancing and stabilizing an interferometer over tens of kilometers as required for the implementation of this protocol represents a considerable challenge, but recent experiments have demonstrated stabilization beyond the requirements of the present proposal [126, 127]. Alternatively, by using a method analogous to the plug-and-play system used in quantum key distribution [128], we can reduce this requirement to stabilization of a small interferometer locally at each detector. Suppose that we wish to generate entanglement between repeater nodes R_1 and R_2. Employing fast optical switches, we excite R_1 by sending a pulse of light toward R_2, where the light is reflected and sent past the detector to R_1. Light emitted from R_1 follows the same path back to the detector. Similarly, we excite R_2 by sending a pulse of light toward a

fast switch at R_1. The two paths thus cover the same path length between the nodes and we are insensitive to fluctuations in the path lengths as long as these fluctuations happen on a time scale which is longer than the time it takes for the pulses to travel between the stations. Alternatively one could change to a protocol which relies on the detection of two photons instead of one. In such protocols the sensitivity to changes in the path lengths can be reduced considerably [129, 130, 131].

5.2.3 Entanglement fidelity in the presence of homogeneous broadening

We now describe this process mathematically, calculating the fidelity of the entangled pair produced by our protocol, as well as the probability for it to succeed. Our analysis incorporates dominant sources of error in solid-state systems; in particular, we account for effects of broadening of the optical transition. Such broadening can be divided into two part: an inhomogeneous broadening representing different mean energy splittings between different centers, and a homogeneous broadening representing the fluctuations of the energy splitting in time. The inhomogeneous broadening can be removed by carefully choosing center with similar properties or by tuning the resonance frequency with external fields. Below we shall therefore only consider the homogeneous broadening.

Our model assumes that the NV centers are excited by a weak driving field applied between the states $|0\rangle$ and $|e\rangle$ with Rabi frequency Ω and the excited states decays with a rate γ. To describe the effect of an additional broadening Γ on the optical transition, we assume that the energy of the excited level fluctuates with a charac-

teristic time which is slow compared to the optical frequency and much shorter than the lifetime of the excited state. In this approximation the broadening can be described by including a time-dependent detuning $\Delta(t)$ with white-noise characteristics: $\langle\Delta(t)\rangle = 0, \langle\Delta(t)\Delta(t')\rangle = \Gamma\delta(t-t')$. Below we shall be working in the limit of weak driving $\Omega \ll \gamma + \Gamma$. In this limit the light emitted from a center consists of two contributions: (i) a coherent part centered around the frequency of the driving laser with a width given by the width of the driving laser, and (ii) an incoherent part centered around the frequency of the transition with a frequency width of $\gamma + \Gamma$. The relative weight of these two contributions is $\gamma : \Gamma$. With considerable broadening of the optical transition $\Gamma \gtrsim \gamma$ it is therefore essential to filter out the incoherent scattered light with a frequency filter to get a high fidelity. To filter out the incoherent light and obtain a high collection efficiency we assume that the centers interact with an optical cavity with a coupling constant g and a decay rate κ. We emphasize, however, that good cavities are not essential for our proposal: we only require sufficient collection efficiency and frequency selectivity, which could also be obtained by collecting the light with a lens and sending it through a narrow frequency filter. In general the weak drive may be detuned from the excited state, which would simplify the filtering of coherent from incoherent light. However, off-resonant excitation would require a stronger driving field, making it harder to avoid stray light reaching the detectors. For simplicity we only discuss the situation where, on average, the driving field and cavity mode are resonant with the center.

The combined NV-center cavity system is then described by the Hamiltonian

$$H = \Delta(t)|e\rangle\langle e| + \frac{\Omega}{2}(|0\rangle\langle e| + |e\rangle\langle 0|) + g\hat{c}^\dagger|0\rangle\langle e| + g|e\rangle\langle 0|\hat{c}, \tag{5.2}$$

where $\hat{c}$ is the photon annihilation operator for the field in the cavity. In the Heisenberg picture, decay terms can be included by considering the quantum Langevin equations of motion for the atomic operators $\hat{\sigma}_{ij} = |i\rangle\langle j|$,

$$\frac{d\hat{c}}{dt} = -\frac{\kappa}{2}\hat{c} - ig\hat{\sigma}_{0e} + \hat{F}_c \tag{5.3}$$

$$\frac{d\hat{\sigma}_{0e}}{dt} = \left(-\frac{\gamma}{2} - i\Delta(t)\right)\hat{\sigma}_{0e} + i\left(g\hat{c} + \frac{\Omega}{2}\right)(\hat{\sigma}_{ee} - \hat{\sigma}_{00}) + \hat{F}_{0e} \tag{5.4}$$

$$\frac{d\hat{\sigma}_{ee}}{dt} = -\gamma\hat{\sigma}_{ee} + \left(i(\frac{\Omega}{2} + g\hat{c}^\dagger)\hat{\sigma}_{0e} + \text{h.c.}\right) + \hat{F}_{ee} \tag{5.5}$$

where the noise $\hat{F}_c$ is the incoming vacuum noise leading to cavity decay at rate κ and the other noise operators $\hat{F}_{0e}, \hat{F}_{ee}$ represent the effect of other optical modes that lead to decay.

We obtain an appropriate solution to the quantum Langevin equations by noting that, in the limit of weak driving, $\Omega \ll \gamma$, there is virtually no population of the excited state, $\hat{\sigma}_{00} - \hat{\sigma}_{ee} \approx \hat{\sigma}_{00}$. The solution can then be written in the form $\hat{c} = \alpha\hat{\sigma}_{00}$+noise and $\hat{\sigma}_{0e} = \beta\hat{\sigma}_{00}$+noise, but the equations for the proportionality constants α and β are complicated due to the noise $\Delta(t)$. By averaging the Langevin equations over the noise one can, find simple equations for the steady state moments of α and β:

$$\overline{\alpha} = \frac{-2g\Omega}{\kappa(\gamma+\Gamma)(1+4g^2/\kappa(\gamma+\Gamma))} \tag{5.6}$$

$$\overline{|\alpha|^2} = \frac{\frac{4g^2\Omega^2}{\kappa^2(\gamma+\Gamma)^2}}{\left(1+\frac{4g^2}{\kappa(\gamma+\Gamma)}\right)\left(1-\frac{\Gamma\kappa}{(\gamma+\Gamma)(\gamma+\kappa)}+\frac{4g^2}{\kappa(\gamma+\Gamma)}\right)} \tag{5.7}$$

$$\overline{\beta} = \frac{-i\Omega}{(\gamma+\Gamma)(1+4g^2/\kappa(\gamma+\Gamma))}. \tag{5.8}$$

Note that in the presence of homogeneous broadening $\Gamma \neq 0$, the moments do not

factor, $\overline{|\alpha|^2} \neq |\overline{\alpha}|^2$, signifying incoherent scattering of light into the cavity.

We now apply the entanglement generation protocol, and use our mathematical model to predict the average density matrix components of the NV center electron spins. In our scheme, we combine the output of the two cavities on a beamsplitter and select the desired entangled state by conditioning on a click in detector D_-, described by the photon annihilation operator $\hat{d}_- = \sqrt{\zeta\kappa/2}(\hat{c}_1 - \hat{c}_2)$. Here, subscripts one and two refer to the two NV-centers we are trying to entangle, ζ is the total collection and detection efficiency for photons leaving the cavity, and we have omitted the contribution from vacuum noise operators. To describe the effect of the detection, we use the quantum jump formalism[132]. If the system starts out in state $|\Psi_{\text{init}}\rangle$, the density matrix element $\rho_{i,j}$ at time t can be found by

$$\rho_{i,j}(t) = \langle\Psi_{\text{init}}|\hat{d}_-(t)^\dagger|j\rangle\langle i|\hat{d}_-(t)|\Psi_{\text{init}}\rangle\delta t/\delta P, \tag{5.9}$$

where the time argument t is included to emphasise the time dependent Heisenberg operators, and where δP is the probability to have a click during a time δt,

$$\delta P = \langle\Psi_{\text{init}}|\hat{d}_-(t)^\dagger\hat{d}_-(t)|\Psi_{\text{init}}\rangle\delta t. \tag{5.10}$$

Our entanglement generation scheme relies on interference to eliminate D_- detection events coming from the initial state $|00\rangle$. However, according to our formalism, if we start out in an initial state $|00\rangle$ the probability to have a click is given by

$$\begin{aligned} \delta P &= \delta t\langle 00|\overline{\hat{d}_-^\dagger\hat{d}_-}|00\rangle \\ &= \kappa\zeta\delta t\Big(\overline{|\alpha|^2} - |\overline{\alpha}|^2\Big), \end{aligned} \tag{5.11}$$

where we assume the noise is independent for the two centers. This expression vanishes only for coherent scattering of light into the cavity, i.e. $\overline{|\alpha|^2} = |\overline{\alpha}|^2$ or $\Gamma = 0$.

In the presence of broadening, there is a finite probability that light will be detected from the $|00\rangle$ state. Similarly, $\Gamma > 0$ leads to a finite probability for incoherent scattering from $|01\rangle$ and $|10\rangle$. Homogeneous broadening thus reduces the fidelity ($F = \langle\Psi_{\rm ideal}|\rho|\Psi_{\rm ideal}\rangle$, (where $|\Psi_{\rm ideal}\rangle$ denotes the ideal entangled state) by

$$\begin{aligned} 1 - F &= \frac{3}{2}\left(1 - \frac{|\overline{\alpha}|^2}{\overline{|\alpha|^2}}\right) \\ &= \frac{3}{2}\frac{\Gamma}{\gamma+\Gamma}\frac{\kappa}{\gamma+\kappa}\frac{1}{1+4g^2/\kappa(\gamma+\Gamma)}. \end{aligned} \tag{5.12}$$

Here we are interested in the limit where the fidelity is close to unity and we shall therefore assume $\overline{|\alpha|^2} \approx |\overline{\alpha}|^2$ in the calculation of other noise sources below.

5.2.4 Other errors

In addition to the error caused by homogeneous broadening, there is also a reduction in fidelity caused by multiple emission events from the centers. This fidelity can conveniently be expressed in terms of the total emission probability

$$P_{em} = \frac{t_0\Omega^2}{(\gamma+\Gamma)[1+4g^2/\kappa(\gamma+\Gamma)]}, \tag{5.13}$$

where t_0 is the duration of the applied laser pulse. In the absence of homogeneous broadening, multiple excitations result in a fidelity

$$F = \frac{1}{2} + \frac{{\rm e}^{-P_{em}(1-\epsilon/2)}}{2} \tag{5.14}$$

and success probability

$$P = (1 - \exp(-\epsilon P_{em}/2))/2. \tag{5.15}$$

The total collection efficiency can be expressed as $\epsilon = \zeta P_{\rm cav}$ with the probability to emit into the cavity given by

$$P_{\rm cav} = \frac{4g^2/\kappa(\gamma+\Gamma)}{1+4g^2/\kappa(\gamma+\Gamma)}. \tag{5.16}$$

This treatment has neglected the possibility of distinguishing multiple photon detection events. If our detector can resolve the photon number, we can use the information to improve our protocol. In particular, a detection in the mode described by $\hat{d}_+ = \sqrt{\zeta\kappa/2}(\hat{c}_1+\hat{c}_2)$+noise has no effect on the component of Eq. (5.1) that we are interested in, since $d_+(|01\rangle + |10\rangle) \propto (|01\rangle + |10\rangle)$. Furthermore, a detection in this plus mode contains contributions from $|00\rangle$, so it yields no useful information. On the other hand, detection events in the mode described by $\hat{d}_-$ change the sign of the superposition state, since $\hat{d}_-(|01\rangle+|10\rangle) \propto (|01\rangle-|10\rangle)$, and $\hat{d}_-(|01\rangle-|10\rangle) \propto (|01\rangle+|10\rangle)$. Consequently, the optimal strategy is to change the phase of the entangled state when an even number of photons is detected. The resulting fidelity is

$$F = \frac{1}{2} + \frac{{\rm e}^{-P_{em}(1-\epsilon)}}{2}. \tag{5.17}$$

Finally, we must include the effect of two other sources of noise: dark counts and electron spin dephasing. In the limit of small success probability P, the dark count introduces an incoherent admixture of the initial state into the resulting density matrix and thus leads to a reduction in fidelity by $P_{\rm dark}/P$, where $P_{\rm dark} = \gamma_{dc} t_0$ is the dark count probability. Electron spin dephasing makes the state decay towards a state with fidelity 1/2 at a rate $2\gamma_e$, yielding a reduction in the fidelity of γ_e times the total time of the experiments. Typically, this total time will be dominated by the classical communication time between nodes, t_c.

Putting these considerations together, we find that the entanglement scheme succeeds with probability $P = (1/2)\left(1 - e^{-P_{\rm em}\epsilon/2}\right) \approx \epsilon P_{\rm em}/4$, producing the state $|\Psi_-\rangle = (|01\rangle - |10\rangle)/\sqrt{2}$ in time $T_0 \approx (t_0 + t_c)/P$ with fidelity

$$\begin{aligned} F_0 &= \frac{1}{2}\left(1 + e^{-P_{\rm em}(1-\epsilon)}\right) - \gamma_e(t_0 + t_c) \\ &\quad -\gamma_{dc}\frac{t_0}{P} - \frac{3}{2}\frac{\Gamma}{\Gamma+\gamma}\frac{\kappa}{\kappa+\gamma}\frac{1}{1+4g^2/\kappa(\gamma+\Gamma)}. \end{aligned} \tag{5.18}$$

For realistic emitters placed into a cavity with either a narrow linewidth $\kappa \ll \gamma$ or a large Purcell factor $4g^2/(\kappa(\gamma+\Gamma)) \gg 1$, the first two terms should dominate the error.

5.3 Comparison to other entanglement generation schemes

The entanglement generation scheme that we have presented so far is the scheme that we believe to be best suited to NV centers. For other systems, this may not be the case. In particular, the presented scheme has two primary drawbacks: (1) it relies on resonant scattering, making it difficult to filter fluorescence photons from the applied laser field; (2) to avoid loss of fidelity from incoherent scattering, one must detect only a narrow frequency interval in the scattered light. Other entanglement methods present different problems which may prove easier to resolve or other methods may be better suited for different physical systems. Consequently, we now briefly compare the resonant scattering scheme presented above to alternate techniques.

5.3.1 Raman transitions

One of the first schemes considered for probabilistic entanglement generation [31, 122, 125] used Raman transitions in three level atoms. In such schemes, an electron spin flip between non-degenerate ground states $|0\rangle$ and $|1\rangle$ is associated with absorption of a laser photon and emission of a frequency shifted Raman photon. After interfering the emission from two atoms, detection of a Raman photon projects the two-atom state onto a state sharing at least one flipped spin. To avoid the possibility that both atoms emitted a Raman photon, the emission probability must be quite small $P_{\rm em} \ll 1$. In this limit, a photon detection event in detector $D_\pm$ results in an entangled spin state $|\Psi_\pm\rangle = (|01\rangle \pm |10\rangle)/\sqrt{2}$.

The Raman scheme can be implemented using either a weak drive between states $|1\rangle$ and $|e\rangle$ or with a short strong pulse which puts a small fraction of the population into $|e\rangle$. Since the latter is equivalent to the single detection π-pulse scheme discussed below, here we consider only weak driving. The system can now be treated using the quantum Langevin-quantum jump approach formulated above. As before, homogeneous broadening on the optical transition leads to an incoherent contribution to the Raman scattered light, which reduces the entanglement fidelity in a manner similar to Eq. (5.12). Again, for optimal fidelity the coherent part should be isolated with a narrow frequency filter. If we assume perfect filtering and a small collection efficiency $\epsilon \ll 1$ the fidelity conditioned on a click is given by

$$F = 1 - P_{\rm em} \tag{5.19}$$

with success probability $P = P_{\rm em}\epsilon$.

In the limit of large fidelity $F \approx 1$, the Raman scheme has a success probability

which is a factor of 4 higher than for our interferometric scheme. Furthermore, the Raman scheme has the advantage that stray light may be spectrally filtered from the Raman photons. Nevertheless, because of the hyperfine interaction in state $|1\rangle$, the transition frequency from $|1\rangle$ to $|0\rangle$ depends on the nuclear spin state. The associated detrimental effect on the nuclear coherence could potentially be avoided by using simultaneous transitions from $|1\rangle|\uparrow\rangle$ and $|-1\rangle|\downarrow\rangle$, which are degenerate. To our knowledge, however, fluorescence between $|e\rangle$ and $|1\rangle$ has not be observed, making it uncertain whether the Raman scheme can be implemented for the NV-centers [1].

5.3.2 π pulses

Time-gated detection offers an alternate method for distinguishing scattered photons from stray incident light. If an atom or NV center is excited by a sufficiently short, strong laser pulse, its population is coherently driven into the excited state. The excited state $|e\rangle$ then decays on a time scale $1/\gamma$. When the decay time is much longer than the incident pulse length, the excitation light and the photon emitted from the atom are separated in time, and can thus be distinguished. Entanglement is then generated conditional on the detection of one or two photons, as elucidated below.

[1] Raman transitions have been observed in a strong magnetic field by using the hyperfine interaction to mix the $|0\rangle$ and $|1\rangle$ states, but since such mixing involves the nuclear degree of freedom it is not applicable in the present context.

Single detection

One particularly simple method for generating entanglement using π-pulses begins with each atom in a state

$$\cos(\phi)|1\rangle + \sin(\phi)|0\rangle. \tag{5.20}$$

The incident π-pulse excites the optically active state $|0\rangle$ to $|e\rangle$ with unit probability, and the spontaneously emitted photons are interfered on a beamsplitter and subsequently measured (as for the Raman scheme above). Provided $\phi \ll 1$ we can ignore the possibility that both atoms are in state $|0\rangle$. A photon detection in $D_\pm$ excludes the state $|11\rangle$, preparing the system in $|\Psi_\pm\rangle$.

As with other entanglement schemes, high-fidelity entanglement generation requires filtering the incoherent scattering caused by homogeneous broadening of the optical transition. In previous sections, we have proposed to use a frequency filter to separate the narrow peak (in frequency) of coherent scattered light from the broad incoherent background. In the present case, filtering can be done in the time domain. In the excitation process a coherence is established between $|1\rangle$ and $|e\rangle$, and following the excitation this coherence (the off-diagonal density matrix element) decays at a rate $\Gamma/2$. By only conditioning on photons emitted a very short time after the excitation, during which the coherence has not had time to decay, a high quality entangled pair is produced.

To describe this process mathematically, we again assume that the atom is placed inside an optical cavity. In contrast to our previous calculations, we assume that the cavity has a broad linewidth to ensure that generated photons leave the system as fast as possible. In the limit $\kappa \gg g$, γ, and Γ we can adiabatically eliminate the

cavity by setting $d\hat{c}/dt = 0$ in Eq. (5.3) so that if we omit the noise we obtain

$$\hat{c}(t) = \frac{2ig}{\kappa}\hat{\sigma}_{0e}. \tag{5.21}$$

Inserting this expression into Eqs. (5.4) and (5.4) we find

$$\overline{\hat{\sigma}_{0e}}(t) = \hat{\sigma}_{0e}(t=0)\exp\left(-\frac{\gamma_{\text{eff}}+\Gamma}{2}t\right) \tag{5.22}$$

$$\overline{\hat{\sigma}_{ee}}(t) = \hat{\sigma}_{ee}(t=0)\exp\left(-\gamma_{\text{eff}}t\right), \tag{5.23}$$

where the effective decay rate γ_{eff} is the decay rate enhanced by the Purcell effect

$$\gamma_{\text{eff}} = \gamma\left(1+\frac{4g^2}{\kappa\gamma}\right). \tag{5.24}$$

To find the fidelity of the entangled state created with this method we again use Eqs. (5.9) and (5.10). For simplicity we only work in the limit of small collection efficiency $\epsilon \ll 1$. Conditioned on a click at time t after the excitation, the fidelity of the entangled state is

$$F = \cos^2(\phi)\left(\frac{1}{2}+\frac{1}{2}\mathrm{e}^{-\Gamma t}\right) \tag{5.25}$$

and the probability to have a click during the short time interval from t to $t+\delta t$ is

$$\delta P = 2\epsilon\gamma_{\text{eff}}\delta t\sin^2(\phi)\mathrm{e}^{-\gamma_{\text{eff}}t}, \tag{5.26}$$

where the collection efficiency $\epsilon = \zeta P_{\text{cav}}$ is again given by the collection efficiency for the light leaving the cavity ζ, and the probability to emit into the cavity is now given by

$$P_{\text{cav}} = \frac{4g^2/\kappa\gamma}{1+4g^2/\kappa\gamma}. \tag{5.27}$$

The success probability for a given fidelity now depends on the ratio between the broadening and the effective decay rate $\Gamma/\gamma_{\text{eff}}$. For $\Gamma = 0$, the procedure of initially

transferring population from $|1\rangle$ to $|0\rangle$ and then applying a π-pulse between $|0\rangle$ and $|e\rangle$ is equivalent to a Raman transition, and Eqs. (5.25,5.26) indeed reproduces the same relation between success probability and fidelity given in Eq. (5.19). In the limit of small broadening, $\Gamma \ll \gamma_{\rm eff}$, the π-pulse scheme is advantageous over the interferometric scheme presented first. In particular, for a fixed fidelity $F \approx 1$ the success probability is a factor of 4 higher.

In the presence of broadening, however, the situation is different. To obtain a high fidelity we should detect only photons emitted within a short time T following the excitation. The average fidelity will then depend on two parameters ϕ and T. By optimizing these two parameters we find that for $F \approx 1$ the fidelity is

$$F = 1 - \sqrt{\frac{\Gamma}{8\gamma_{\rm eff}}}\sqrt{\frac{P}{\epsilon}}. \tag{5.28}$$

Since previous expressions (5.14) and (5.19) for $1-F$ depended linearly on P, this represents a much faster decrease in the fidelity. The $\pi-$pulse scheme is thus less attractive for homogeneously broadened emitters.

Double detection

If the collection efficiency is very high, it may be an advantage to rely on the detection of two photons instead of one [133, 134, 129, 130]. In this scheme, both atoms are initially prepared in $(|0\rangle+|1\rangle)/\sqrt{2}$ and a π-pulse is applied between $|0\rangle$ and $|e\rangle$. Following a detection in $D_\pm$ the populations in states $|0\rangle$ and $|1\rangle$ are interchanged and another π-pulse is applied between $|0\rangle$ and $|e\rangle$. Conditioned on clicks following both π pulses we can exclude the possibility that the atoms were initially in the same state and we are left with $|\Psi_\pm\rangle$ conditioned on appropriate detector clicks. In the

absence of homogeneous broadening, this protocol produces an entangled state with fidelity F=1 with probability $P = \epsilon^2/2$. The double-detection scheme thus avoids the multiple photon emission errors inherent in the single-detection schemes.

With broadening of the optical transition, this is no longer the case. For $F \approx 1$, the relation between fidelity and success probability is now given by

$$F = 1 - \frac{\Gamma}{\gamma_{\text{eff}}\epsilon}\sqrt{2P}. \tag{5.29}$$

Again the fidelity decreases more rapidly with the success probability than for the Raman and resonant scattering scheme, making it less useful for our purpose.

5.3.3 Summary

The best choice of scheme depends on the specific physical situation. The two π-pulse schemes are advantageous if the broadening is negligible. In particular in the limit where we can ignore all errors except the photon attenuation, the double detection scheme results in the highest fidelity entangled pair. With low collection efficiency or large distances between emitters, the double detection will have a very small success probability because of the ϵ^2 factor, and it may be advantageous to rely on a single detection scheme.

The π-pulse schemes are less attractive if we are limited by homogeneous broadening of the optical transition because the fidelity decreases rapidly with the success probability. Better results are obtained for the resonant scattering or Raman schemes. When possible, the Raman scheme offers the best solution. The frequency-shifted Raman scattering allows frequency filtering of the incoming light; in addition the success probability is four times higher than for the resonant scattering scheme. But, as men-

tioned above, it is not always possible to drive Raman transitions , and it may be hard to achieve Raman transition which are independent of the nuclear spin state. For this reason we believe that the resonant scattering scheme is most promising in the particular case of NV-centers.

Finally we wish to add that the calculations we have performed here assume a specific model for the broadening (short correlation time for the noise). With other broadening mechanisms, e.g. slowly varying noise, these considerations will be different.

5.4 Entanglement swapping and purification

Using one of the procedures outlined above, electron spin entanglement can be generated between adjacent pairs of nodes. We now discuss a means to extend the entanglement to longer distances.

5.4.1 Swapping

After entangling nearest-neighbor electron spins, the electron spin state is mapped onto the auxiliary nuclear spin qubit for long-term storage using the hyperfine interaction. This operation leaves the electronic degree of freedom available to generate entanglement between unconnected nodes, as illustrated in Figure 5.3. By combining optical detection of individual electron spin states [91] and effective two-qubit operations associated with hyperfine coupling of electronic and nuclear spins [79], we may projectively measure all four Bell states in the electronic/nuclear manifold associated with each emitter. The outcomes of the Bell state measurements reveal the appro-

priate local rotations to obtain a singlet state in the remaining pair of nuclear spins, implementing a deterministic entanglement swap [116, 115]. By performing this procedure in parallel, and iterating the process for $N \propto \log_2(L/L_0)$ layers, we obtain the desired nuclear spin entanglement over distance L in a time $\propto L \log_2(L/L_0)$.

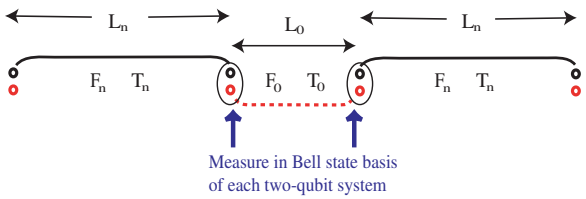

Figure 5.3: *Entanglement propagation by swapping. To generate an entangled nuclear spin pair (black) over the distance $L_{n+1} = 2L_n + L_0$, we first generate nuclear entanglement over the first and second pair of repeater stations which are distance L_n apart. The electron spin (red) is then used to generate entanglement between the middle stations, separated by distance L_0. Nuclear (electron) spin entanglement is illustrated by solid (dashed) lines. Entanglement swapping is performed by measuring in the Bell state basis of the two-qubit system.*

5.4.2 Purification

To extend entanglement to long distances in the presence of errors, active purification is required at each level of the repeater scheme. By performing local operations and measurements, it is possible to distill multiple entangled pairs with fidelity above some threshold F_{min} into a single entangled pair with higher purity[119, 120]. The purification algorithm we use is described in detail in Refs.[120, 56, 57, 135]. For clarity we will present it in a form appropriate to the system under consideration, which uses repeated generation of electron spin entangled pairs to purify a stored nuclear spin entangled pair. Specifically, an electron spin entangled pair between stations i and j is described by the density matrix diagonal components $\{a_e, b_e, c_e, d_e\}$ in the

Bell state basis $\{|\Psi_-\rangle, |\Phi_+\rangle, |\Phi_-\rangle, |\Psi_+\rangle\}$, where

$$|\Psi_\pm\rangle_{ij}^{(e)} = \frac{1}{\sqrt{2}}\left(|0_i 1_j\rangle \pm |1_i 0_j\rangle\right) \tag{5.30}$$

$$|\Phi_\pm\rangle_{ij}^{(e)} = \frac{1}{\sqrt{2}}\left(|0_i 0_j\rangle \pm |1_i 1_j\rangle\right). \tag{5.31}$$

We will refer to these diagonal elements as the "vector fidelity" $\mathcal{F}_e = \{a_e, b_e, c_e, d_e\}$, noting that the first element $(\mathcal{F}_e)_1 = a_e$ encodes the fidelity with respect to the desired singlet state. A nuclear spin entangled pair between those stations is described by a similar vector fidelity $\mathcal{F}_n = \{a_n, b_n, c_n, d_n\}$ in the nuclear Bell basis

$$|\Psi_\pm\rangle_{ij}^{(n)} = \frac{1}{\sqrt{2}}\left(|\downarrow_i\uparrow_j\rangle \pm |\uparrow_i\downarrow_j\rangle\right) \tag{5.32}$$

$$|\Phi_\pm\rangle_{ij}^{(n)} = \frac{1}{\sqrt{2}}\left(|\downarrow_i\downarrow_j\rangle \pm |\uparrow_i\uparrow_j\rangle\right). \tag{5.33}$$

The purification protocol calls for a local rotation of each spin system at both locations:

$$|0\rangle_{i,j} \rightarrow \frac{1}{\sqrt{2}}\left(|0\rangle_{i,j} + i\,|1\rangle_{i,j}\right) \tag{5.34}$$

$$|1\rangle_{i,j} \rightarrow \frac{1}{\sqrt{2}}\left(|1\rangle_{i,j} + i\,|0\rangle_{i,j}\right) \tag{5.35}$$

$$|\downarrow\rangle_{i,j} \rightarrow \frac{1}{\sqrt{2}}\left(|\downarrow\rangle_{i,j} + i\,|\uparrow\rangle_{i,j}\right) \tag{5.36}$$

$$|\uparrow\rangle_{i,j} \rightarrow \frac{1}{\sqrt{2}}\left(|\uparrow\rangle_{i,j} + i\,|\downarrow\rangle_{i,j}\right), \tag{5.37}$$

followed by a two-qubit gate at each location:

$$\begin{array}{rclrcl}
|\downarrow 0\rangle_i &\rightarrow& |\downarrow 0\rangle_i & |\downarrow 0\rangle_j &\rightarrow& |\downarrow 1\rangle_j \\
|\downarrow 1\rangle_i &\rightarrow& |\downarrow 1\rangle_i & |\downarrow 1\rangle_j &\rightarrow& |\downarrow 0\rangle_j \\
|\uparrow 0\rangle_i &\rightarrow& -|\uparrow 1\rangle_i & |\uparrow 0\rangle_j &\rightarrow& |\uparrow 0\rangle_j \\
|\uparrow 1\rangle_i &\rightarrow& -|\uparrow 0\rangle_i & |\uparrow 1\rangle_j &\rightarrow& |\uparrow 1\rangle_j .
\end{array} \tag{5.38}$$

After these operations, the electron spin is projectively measured at both locations. When the two electron spins are in the opposite state, the purification step succeeds, mapping the remaining nuclear spins to a diagonal state $\{a'_n, b'_n, c'_n, d'_n\}$ with $a'_n > a_n$.

For the particular entanglement protocol we considered in Sec. 5.2, the first to terms in Eq. 5.18 which we expect to be dominant, introduces phase errors of the form $\{f, 0, 0, 1-f\}$. This purification protocol above is therefore chosen so that it functions best for phase errors, but it can correct for any type of errors. To quantify the type of error associated with our entanglement generation scheme, we define a shape parameter υ such that the vector fidelity for entangled spin pairs between adjacent nodes is

$$\mathcal{F}_0 = \{F_0, (1-F_0)\upsilon, (1-F_0)\upsilon, (1-F_0)(1-2\upsilon)\}. \tag{5.39}$$

Note that $\upsilon \to 0$ corresponds to phase errors while $\upsilon \to 1/3$ corresponds to a Werner state with equal distribution of all error types. Note also that the assumption of diagonality imposes no restriction on the entangled states we generate, as any off-diagonal elements in their density matrices can be eliminated by performing random rotations (similar to the procedure for creating Werner states but without the symmetrization step)[135]. Furthermore, even without a randomization step, the average fidelity is determined by the diagonal elements [120].

5.4.3 Errors

In the presence of local errors in measurements and operations, the purification and swap procedures deviate from their ideal effect. To describe this we use the error model described in [57]. Measurement errors are quantified using a parameter η such

that measurement projects the system into the desired state with probability η and into the incorrect state with probability $1-\eta$. For example, a projective measurement of state $|0\rangle$ would be

$$P_0 = \eta \left|0\right\rangle \left\langle 0\right| + (1-\eta) \left|1\right\rangle \left\langle 1\right|. \tag{5.40}$$

Errors in local operations are accounted for in a similar manner. With some probability p, the correct operation is performed; otherwise one traces over the relevant degrees of freedom in the density matrix and multiplies by the identity matrix (for further details see[57] and references therein). For example, the action of a two qubit operation U_{ij} would become

$$U_{ij}\rho U_{ij}^{\dagger} \rightarrow p\ U_{ij}\rho U_{ij}^{\dagger} + \frac{1-p}{4} Tr_{ij}(\rho) \otimes \mathcal{I}_{ij} \tag{5.41}$$

In our calculations, we neglect errors in single qubit operations and focus on two-qubit errors, which are likely to yield the dominant contribution.

These errors determine the level of purification which is possible given infinitely many purification steps. They also determine how much the fidelity degrades during the entanglement swap procedure. Below we describe a repeater protocol which compared to the original proposal [56] reduces the required number of qubits at each repeater station at the expense of extra connection steps. Owing to these extra connection steps, our protocol is slightly more sensitive to local errors than the original scheme.

5.4.4 Nesting Scheme

Previous proposals for fault tolerant long distance quantum communication have required larger and larger numbers of qubits at each node as the communication

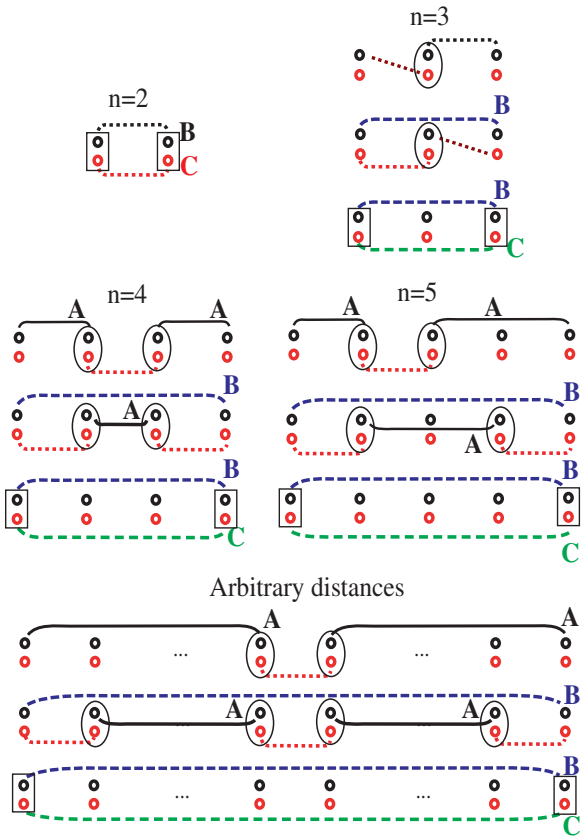

Figure 5.4: *Nesting scheme for generation and purification of entangled nuclear and electron spin pairs. In each node, the nuclear spin degree of freedom is represented by the upper (black) circle, while the electron degree of freedom is represented by the lower (red) circle. Entanglement between different nodes is represented by a line connecting them. Ovals represent entanglement swap steps, and rectangles represent entanglement purification steps. For $n = 2$ the B and C pairs may be directly generated. For $n \geq 3$, the first step illustrates how the B pair is generated, while the remaining two steps illustrate how the C pair is generated while storing the B pair. The arbitrary distance algorithm works for $n \geq 6$.*

distance is increased. Here we describe a nesting scheme which can be used to communicate over arbitrarily long distances while maintaining a constant requirement of only two qubits per node.

The scheme for nested entanglement purification is illustrated in Figure 5.4. For

clarity, we will label purified pairs by"A", pairs to be purified by "B", and auxiliary pairs used to perform purification by "C". Briefly, an entangled pair ("B") is stored in the nuclear spins while an auxiliary entangled pair ("C") is generated in the electron spins. The purification protocol described in [120, 57] is then performed by entangling the electron and nuclear spins via the hyperfine interaction, and subsequently measuring the electron spins. Comparison of the measurement outcomes reveals whether the purification step was successful, resulting in a new stored pair B with higher fidelity. After successfully repeating the procedure for m purification steps, (a technique is known as "entanglement pumping"), the stored pair becomes a purified ("A") pair, which can then be used to create B and C pairs over longer distances. We may thus generate and purify entanglement to arbitrary distances. This procedure is analogous to the proposal in Ref. [56], but avoids the increase in the number of qubits required for that proposal.

Mathematically, the scheme can be explained most easily using inductive arguments. Suppose that we have a means to create and purify entanglement over $2, 3, \cdots, n/2$ repeater stations ($(n+1)/2$ if n is odd), and that we know the vector fidelity $\mathcal{F}_A(n)$ and the time $\mathcal{T}_A(n)$ required for each distance. We can then determine the time required and the vector fidelity possible after purification over n repeater stations.

We begin by creating two purified nuclear spin A pairs over half the distance and connecting them via a central electron spin pair of vector fidelity $\mathcal{F}_0$. In the presence of local errors, this yields a nuclear spin B pair with vector fidelity

$$\mathcal{F}_B(n) = \mathcal{C}\left(\{\mathcal{F}_A(\frac{n}{2}), \mathcal{F}_0, \mathcal{F}_A(\frac{n'}{2})\}, \eta, p\right). \tag{5.42}$$

Here, $\mathcal{C}$ gives the vector fidelity obtained upon connecting the entangled pairs in the presence of local errors[135], and $n/2$ and $n'/2$ are understood to represent $(n-1)/2$ and $(n+1)/2$ when n is odd. The B pair is created in a time

$$\mathcal{T}_B(n) = \frac{3}{2}\mathcal{T}_A(\frac{n'}{2}) + T_0 + \frac{n'}{2}t_c, \tag{5.43}$$

where T_0 is the time required to generate nearest-neighbour entanglement, t_c is the classical communication time between adjacent stations, and the factor of $\frac{3}{2}$ arises from the average time required to obtain two copies of an A pair over distance $(n'/2)$ [2]. We neglect the time required for local operations and measurement since these times are short compared to T_0 and nt_c. Similarly, we can find the vector fidelity and time for the electron spin C pair

$$\begin{aligned} \mathcal{F}_C(n) &= \mathcal{C}(\{\mathcal{F}_0, \mathcal{F}_A(\frac{n}{2}-1), \mathcal{F}_0, \mathcal{F}_A(\frac{n'}{2}-1), \mathcal{F}_0\}, \eta, p) \\ \mathcal{T}_C(n) &= \frac{3}{2}\mathcal{T}_A(\frac{n'}{2}-1) + \frac{11}{6}T_0 + (n-2)t_c. \end{aligned} \tag{5.44}$$

After performing one purification step, we obtain a nuclear spin pair A_1, with vector fidelity determined by the purification function $\mathcal{P}$

$$\mathcal{F}_{A_1}(n) = \mathcal{P}(\mathcal{F}_B(n), \mathcal{F}_C(n), \eta, p). \tag{5.45}$$

On average, the time required to perform this single step is

$$\mathcal{T}_{A_1}(n) = \frac{(\mathcal{T}_B(n) + \mathcal{T}_C(n) + (n-1)t_c)}{P_S(\mathcal{F}_B(n), \mathcal{F}_C(n))}, \tag{5.46}$$

[2]For n Poisson processes with average success time τ, the probability that all n processes have succeeded in a time t is $(1-\exp(-t/\tau))^n$. Differentiating this cumulative distribution with respect to t gives the probability distribution for the time t required for n successes, $P(t,n) = (n/\tau)\exp(-t/\tau)(1-\exp(-t/\tau))^{n-1}$. The average time required for n successes is then $H_n = \sum_{m=1}^{n}\frac{\tau}{m}$. For two simultaneous Poisson processes, the average wait time for both to succeed is $3\tau/2$, whereas for three the average wait time is $11\tau/6$.

where P_S is the probability that the purification step succeeds.

After m successful purification steps, the vector fidelity of the nuclear spin A_m pair is

$$\mathcal{F}_{A_m}(n) = \mathcal{P}(\mathcal{F}_{A_{m-1}}(n), \mathcal{F}_C(n), \eta, p), \tag{5.47}$$

and the average time required for its creation is

$$\begin{aligned} \mathcal{T}_{A_m}(n) &= \frac{\left(\mathcal{T}_{A_{m-1}}(n) + \mathcal{T}_C(n) + (n-1)t_c\right)}{P_S(m)} && (5.48) \\ &= (\mathcal{T}_C(n) + (n-1)t_c) \sum_{n=1}^{m} \prod_{k=n}^{m} \left(\frac{1}{P_S(m)}\right) \\ &\quad + \mathcal{T}_B(n) \prod_{k=1}^{m} \left(\frac{1}{P_S(m)}\right), && (5.49) \end{aligned}$$

where $P_S(m) = P_S(\mathcal{F}_{A_{m-1}}(n), \mathcal{F}_C(n))$. If we stop purifying at some fixed number M of purification steps, then the desired vector fidelity and time over distance n are given by

$$\begin{aligned} \mathcal{F}_A(n) &= \mathcal{F}_{A_M}(n) && (5.50) \\ \mathcal{T}_A(n) &= \mathcal{T}_{A_M}(n). && (5.51) \end{aligned}$$

To complete the inductive argument, we must show that the protocol works for small distances. There are many schemes one can use to generate and purify entanglement over shorter distances, and one possibility is illustrated in Figure 5.4. In fact, once the physical parameters for an implementation are determined, it should be possible to optimise the few-node scheme to minimise the required time or maximise the resulting fidelity.

5.4.5 Fixed point analysis

As the number of purification steps increases $m \to \infty$, the fidelity of the resulting entangled pair saturates. This saturation value can be found using a fixed point analysis (as described in[57]) by solving for the vector fidelity $\mathcal{F}_A$ which is unchanged by further purification steps

$$\mathcal{F}_A = \mathcal{P}\left(\mathcal{F}_A, \mathcal{F}_C, \eta, p\right), \tag{5.52}$$

where we have explicitly included the local errors in the purification function $\mathcal{P}$. This yields a fixed point fidelity $\mathcal{F}_{FP}(\mathcal{F}_C, \eta, p)$ which is independent of $\mathcal{F}_A$. Since the vector fidelity $\mathcal{F}_{\mathcal{A}}$ has three independent parameters characterising the diagonal elements of the density matrix, one might miss the fixed point. However, as the number of purification steps increases our simulations do indeed approach the calculated fixed point. We therefore calculate the fixed point as a function of distance to find the upper bound on the fidelity which can be attained for given $\mathcal{F}_0, L/L_0, p$, and η.

5.4.6 Asymptotic Fidelity

As the distance increases $L \to \infty$, the fixed point fidelity can approach an asymptotic value F_∞. We can understand the existence of F_∞ and its value by examining the protocol as a function of nesting level. In particular, to generate entanglement over n repeater stations we operate at nesting level $i \sim \log_2 n$, where we obtain a purified pair

$$\mathcal{F}_A^{(i)} = \mathcal{F}_{FP}(\mathcal{F}_C^{(i)}, \eta, p), \tag{5.53}$$

where $\mathcal{F}_{FP}$ is the fixed point solution to Eq. (5.52), and $(\mathcal{F}_{FP})_1 = F_{FP}$ is the fixed point fidelity. We will then use this purified pair $\mathcal{F}_A^{(i)}$ to build up an auxiliary C pair on the next nesting level $i+1$. Since the fidelity over distance $n-1$ is greater than that over distance n, i.e. $(\mathcal{F}_A(n-1))_1 \gtrsim (\mathcal{F}_A(n))_1$, the auxiliary pair fidelity we obtain will be greater than or equal to the first component of

$$\mathcal{F}_C^{(i+1)} \sim C(\{\mathcal{F}_A^{(i)}, \mathcal{F}_A^{(i)}, \mathcal{F}_0, \mathcal{F}_0, \mathcal{F}_0\}, \eta, p), \tag{5.54}$$

where C is again the connection function. This auxiliary pair will then determine $\mathcal{F}_A^{(i+1)} = \mathcal{F}_{FP}(\mathcal{F}_C^{(i+1)}, \eta, p)$. When $\mathcal{F}_A^{(i+1)} = \mathcal{F}_A^{(i)}$, we have reached the asymptotic fidelity $F_\infty = (\mathcal{F}_A)_1$ (see Figure 5.5), which is given by the intersection of the purification curve Eq. (5.53) and the auxiliary pair creation curve Eq. (5.54).

As was the case for the fixed point analysis, we must account for all diagonal components of the density matrix in the Bell state basis (not just the fidelity a). Consequently the asymptotic fidelity represents an upper bound to which the system may converge in the manner indicated by our simulations. Finally, we should stress that our calculations have not incorporated loss due to the long but finite memory time in the nuclear spins. This loss increases with the total time required for repeater operation, and sets the upper limit on the distance over which our scheme could operate.

5.4.7 Results

The discussion of final fidelity may be summarized as follows: the fidelity obtained at the end of this nested purification procedure, $F(m, L, F_0, p, \eta)$, depends on the number of purification steps m, the distance L between the outer nodes, the initial

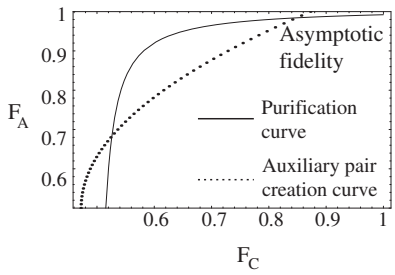

Figure 5.5: *Approach to asymptotic fidelity. The solid curve shows the purified fidelity obtained from the auxiliary pair, while the dotted curve corresponds to the auxiliary pair (constructed from two smaller purified pairs) on the next nesting level. The system moves between the curves at each nesting step, and the upper intercept of the two curves gives the asymptotic fidelity. For this calculation* $F_0 = p = \eta = 0.99$, *and* $\upsilon = 0$.

fidelity F_0 between adjacent nodes, and the reliability of measurements $\eta \leq 1$ and local two-qubit operations $p \leq 1$ required for entanglement purification and connection [57]. As the number of purification steps increases $m \to \infty$, the fidelity at a given distance L approaches a fixed point $F \to F_{FP}(L, F_0, p, \eta)$ at which additional purification steps yield no further benefit [57]. Finally, as L increases, the fidelity may approaches an asymptotic value $F_{FP} \to F_\infty(F_0, p, \eta)$. Figure 5.6a illustrates the efficiency of the purification protocol: for initial fidelities $F_0 \gtrsim 97\%$, three purification steps suffice to produce entanglement at large distances.

Figure 5.6b demonstrates that our scheme permits generation of high-fidelity, long distance entangled pairs in the presence of percent-level errors in polynomial time. Because solid-state devices allow fast operations and measurements, the overall time scale is set by the classical communication time between nodes. As an example, using a photon loss rate of ~ 0.2 dB/km, nodes separated by $L_0 \sim 20$ km (so that in the limit of good detectors the collection efficiency is $10^{-0.4} \sim 1/e$), an emission

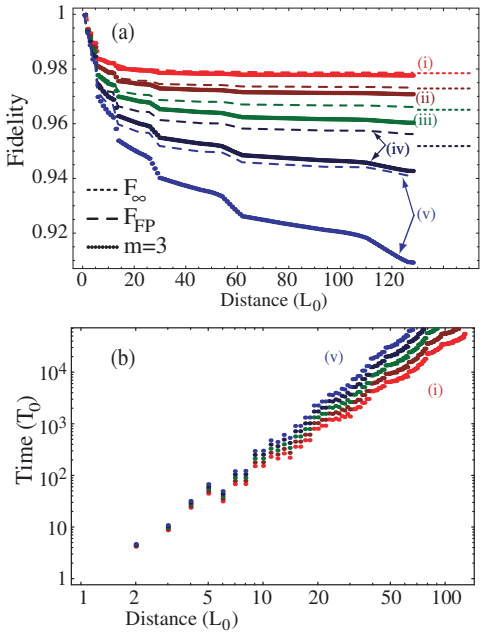

Figure 5.6: *(a) Fidelity scaling with distance. Points show results using 3 purification steps at each nesting level; dashed lines show the fixed point F_{FP} at each distance; dotted lines indicate the asymptotic fidelity F_∞. For (a) and (b), measurements and local two-qubit operations $\eta = p$ contain 0.5% errors. The initial fidelity F_0 is (i) 100% (ii) 99% (iii) 98% (iv) 97% (v) 96% with phase errors only. (b) Average time scaling with distance for m=3, given in units of $T_0 = (t_0 + t_c)/P$, the time required to generate entanglement between nearest neighbors, and L_0, the distance between nearest neighbors. Measurement and local operation times are neglected. Note that the axes are logarithmic, so time scales polynomially with distance.*

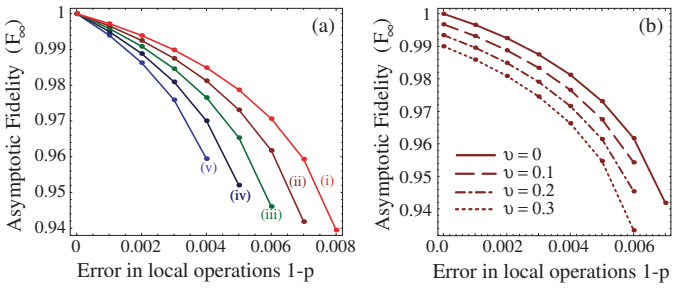

Figure 5.7: *(a) Long-distance asymptote dependence on initial fidelity F_0 of (i) 100% (ii) 99% (iii) 98% (iv) 97% (v) 96% with phase errors only. (b) Long-distance asymptote dependence on error type. For the calculations shown, $F_0 = 0.99$, and the shape parameter ranges from $\upsilon = 0$ to $\upsilon = 0.3$. In both (a) and (b) measurement errors are set equal to operational errors, $\eta = p$.*

probability $P_{\rm em} \sim 8\%$, and just one purification step at each nesting level, our scheme could potentially produce entangled pairs with fidelity $F \sim 0.8$ sufficient to violate Bell's inequalities over 1000 km in a few seconds. For comparison, under the same set of assumptions direct entanglement schemes would require $\sim 10^{10}$ years.

Fig. 5.7a shows that our scheme will operate in the presence of $1-p \lesssim 1\%$ errors in local operations and percent-level phase errors in initial entanglement fidelity. Other types of error are in principle possible, and we consider nonzero shape parameters v for the initial fidelity $\mathcal{F}_0$ in Eq. (5.39). The asymptotic fidelity shown in Fig. 5.7b indicates that, although the protocol we use is most effective for purifying phase errors, it also tolerates arbitrary errors.

5.4.8 Optimization

Once the parameters of the system are established, the protocol can be optimised to minimise the time required to generate some minimum fidelity F_{min} over a distance L. We can vary the number of repeater stations $\sim L/L_0$ and the number of purifi-

cation steps m (which need not be constant). We can also tailor the entanglement generation procedure by changing the emission probability P_{em} to find the optimum balance between initial infidelity $1 - F_0 \sim P_{em}$ and entanglement generation time $T_0 \propto 1/P_{em}$. Finally, one could use more advanced optimal control techniques to vary the details of the protocol itself. In particular, it should be possible to speed up the algorithm by working simultaneously on multiple nesting levels, beginning entanglement generation and connection on the next nesting level as soon as the interior nodes are free. Further speed-up may also be possible in the case when collection efficiency is very high by using coincidence detection in combination with e.g. time-bin encoding [55]. As noted previously such coincidence detection could also be advantageous for interferometric stability [129, 130, 131].

Ultimately, the speed of this protocol is limited by three factors: classical communication time between nodes, probabilistic entanglement generation, and sequential purification. Faster techniques will require more efficient entanglement generation or larger numbers of qubits at each node to allow simultaneous purification steps.

5.4.9 Comparison to other quantum repeater schemes

This scheme combines the advantages of two pioneering proposals for quantum repeaters [56, 32]. Early work showed that entanglement purification and swapping could be combined to permit efficient, fault-tolerant quantum communication over distances longer than an attenuation length [56]. This scheme incorporated error correction at the cost of increased physical resources, requiring nodes containing a number of qubits scaling at minimum logarithmically with distance [57]. Owing to

the difficulty of implementing even few-qubit quantum computation, implementation of this scheme remains a challenging goal. Our scheme is closely related to the original proposal with one key difference: by spatially rearranging the required physical resources, we can efficiently simulate their protocol while maintaining a constant requirement on qubits per node. This makes our scheme amenable to realistic physical implementation.

Another physical implementation for quantum repeaters uses atomic ensembles as a long-lived memory for photons[32]. Entanglement is generated by interfering Raman scattered light from two ensembles. The entanglement is probabilistically swapped using an EIT readout technique. This scheme elegantly avoids effects of the dominant photon loss error by conditioning success on photon detection. Our scheme primarily differs from this proposal in two ways: first, access to two-qubit operations between electron and nuclear spin permits deterministic entanglement swapping; second, the two-qubit nodes allow active correction of arbitrary errors.

5.5 Physical systems

We conclude with three specific examples for potential implementation of the presented method.

5.5.1 Implementation with NV centers

The NV center level structure illustrated in Fig. 5.2 allows implementation of all steps in the repeater protocol. The cycling transition from $|0\rangle$ to $|e\rangle$ is used for electron spin initialization by measurement, entanglement generation, and electron spin

state measurement. A series of ESR and NMR pulses can be used to perform arbitrary gates between the electron spin and an adjacent ^{13}C spin [79]. Consequently, nuclear spin state initialization and measurement is achieved by initializing the electron spin, mapping the nuclear spin state onto the electron spin, and subsequently measuring the electron spin. Entanglement propagation and purification can be implemented in NV centers by driving ESR and NMR transitions and using optical detection of the electron spin states. Once electron spin entanglement is established between nodes R_i and R_{i-1}, it can be transferred to the nuclear spins, leaving the electron degree of freedom free to generate entanglement between station R_i and R_{i+1}. Provided that we can reinitialize the electron spin without affecting the nuclear entanglement, we can perform the same probabilistic entanglement procedure. Note that ESR multiplexing is required to perform a $\pi/2$ pulse independent of the nuclear spin; this can be accomplished simply by applying two ESR pulses at the two transition frequencies.

We now consider the feasibility of implementing our repeater protocol using NV centers in diamond. Owing to the overlap of electron wavefunctions in the ground and excited states, most of the NV center optical emission goes into the phonon sidebands. Other color centers in diamond, for example the NE8 center [136, 137] may suffer less from this drawback. To enhance the relative strength of the zero-phonon line, it will be necessary to couple NV center to a cavity. For NV centers coupled to cavities with Purcell factors ~ 10 [42], we find that the dominant source of error is electron spin decoherence during the classical communication period. Using an emission probability $P_{\rm em} \sim 5\%$, a collection efficiency $\epsilon \sim 0.2$, and a classical communication time of $t_c \sim 70\mu$s over $L_0 \sim 20$ km, we find the fidelity of directly entangled pairs can

reach $F_0 \sim 97\%$ for electron spin coherence times in the range of a few milliseconds. Electron spin coherence times in the range of 100μs have been observed at room temperature and significant improvements are expected for high purity samples at low temperatures [138]. The large hyperfine splitting allows fast local operations between electron and nuclear spin degrees of freedom on a timescale $\sim$ 100ns [79] much shorter than the decoherence time, allowing $1 - p < 1\%$. Finally, cavity enhanced collection should significantly improve observed measurement efficiencies of $\eta \sim 80\%$ [79].

5.5.2 Alternative implementation: quantum dots

Our discussion thus far has attempted to remain general while exemplifying our proposal using NV centers. The basic idea of using two-qubit repeater stations should be applicable to a wide variety of systems featuring coupled electron and nuclear spins. To illustrate an alternative implementation, we consider doped self-assembled quantum dots whose electron spin is coupled to collective nuclear states in the lattice. Compared to NV centers, this system offers large oscillator strengths and the potential for Raman manipulation. Doped semiconductor quantum dots have been considered in a variety of quantum computing proposals and related technologies [139, 140]. The spin state of the dopant electron provides a natural qubit with relatively long coherence times. Assuming a high degree of nuclear spin polarization ($P_{\mathrm{n}} \gtrsim 0.95$) [141] and active ESR pulse correction, the electron spin dephasing time is expected to be 1 ms [142]. The spins of lattice nuclei in the quantum dot provide an additional, quasi-bosonic degree of freedom with extremely long coherence times ($\sim$ 1 s with active correction [143]). Such ensembles of nuclear spin have been considered for use as a

quantum memory [51] and, by taking advantage of the non-linearity of the Jaynes-Cummings Hamiltonian, as a fundamental qubit for a quantum computer [144].

Unlike the spin triplet state of the NV centers, the conduction band electron has two states, $|\uparrow\rangle$ and $|\downarrow\rangle$, corresponding to spin aligned and anti-aligned with an external magnetic field $B_{ext}||\hat{z}$. The quantum dot system also differs from NV centers in that it can be manipulated using Raman transitions: when the external field and growth direction are perpendicular (Voigt geometry), two allowed optical transitions to a trion state produce a lambda system; moving towards aligned field and growth directions (Faraday geometry) suppresses the"forbidden" transitions, as shown in Fig. 5.8a.

Electron spin coherence can thus be prepared via Raman transitions or by standard ESR setups, and changes in effective magnetic field can be accomplished by off-resonant, spin-dependent AC Stark shifts with σ_+ light.

Although optical transitions in doped quantum dots can exhibit homogeneous broadening $\Gamma \sim 100$ GHz$\sim 10 - 100\gamma$ [145], the corresponding error can be made negligible by sending the output from the cavity through a frequency filter with a linewidth of a few hundred MHz. [3] Moreover, we note that InAs quantum dots have been successfully coupled to microcavities with Purcell factors ~ 10 [42].

Whereas the NV center electron spin was coupled to a single nuclear impurity, the electron in a quantum dot couples to collective excitations of many thousands of nuclei. We briefly discuss this system; further details are given in Refs. [51, 146]. The

[3]For our entanglement generation scheme, such a filter will allow the desired narrow band of coherent light to pass through while rejecting the broad incoherent background. Consequently the filter will not decrease collection efficiency in the desired mode.

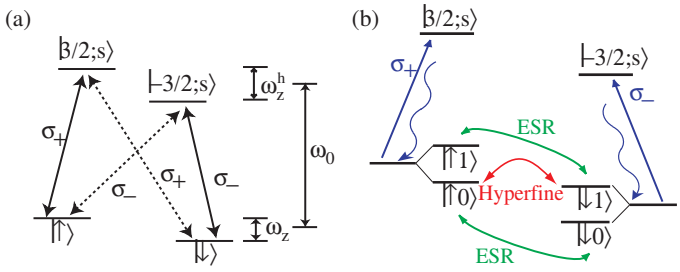

Figure 5.8: *(a) Level structure for single electron to trion transition in a single-electron doped III-V or II-VI quantum dot with external magnetic field in close to a Faraday geometry with Zeeman splitting ω_z, heavy-hole splitting ω_z^h and up to four optical fields of different frequency and polarization. Dashed lines indicate weak dipole moments due to small magnetic field mixing. The triplet two-electron states are not included due to a large ($> 1meV$) exchange energy allowing for complete suppression of their effects. (b) Electronic ($|\uparrow\rangle, |\downarrow\rangle$) and collective nuclear ($|0\rangle, |1\rangle$) states and their transitions for singly doped quantum dots in a polarized nuclear spin lattice.*

Hamiltonian governing this interaction is

$$H_{qd} = \omega_z \hat{S}_z + \hbar \sum_k \gamma_k \hat{I}_z^k + \hbar\Omega \sum_k \lambda_k \hat{\vec{S}} \cdot \hat{\vec{I}}^k, \tag{5.55}$$

where γ_k is the gyromagnetic ratio for nuclear spin $\hat{\vec{I}}^k$, the nuclear spin coupling amplitudes satisfy $\lambda_k \propto |\psi(r_k)|^2$, $\sum_k \lambda_k^2 = 1$, and $\Omega = A/\hbar \sum_k \lambda_k$ (A is the hyperfine interaction constant). By identifying collective nuclear spin operators, $\hat{\vec{A}} = \sum_k \lambda_k \hat{\vec{I}}$, the hyperfine term may be written $\hbar\Omega \hat{\vec{S}} \cdot \hat{\vec{A}}$. For simplicity we restrict the following discussion to the case of perfect nuclear polarization (so the initial state of all N_n nuclear spins in the quantum dot is $|0\rangle = |-I\rangle \otimes \ldots \otimes |-I\rangle$ for I-spins). Then an effective Jaynes-Cummings type Hamiltonian describes the system:

$$H_{qd}^{eff} = \hbar\omega_z^{eff} \hat{S}_z + \hbar\Omega/2(\hat{A}_+ \hat{S}_- + \hat{A}_- \hat{S}_+). \tag{5.56}$$

with corrections of order $\Omega/\sum_k \lambda_k \sim A/N_n$. The effective Zeeman splitting $\omega_z^{eff} = \omega_z - IA/\hbar$ is dominated by the field associated with the polarized nuclear spins; for

example, in GaAs quantum dots, this Overhauser shift is $IA/\hbar \sim 33$GHz. The large detuning ω_z^{eff} suppresses interactions which exchange energy between the electron and nuclear spins. By changing the effective magnetic field, we can shift the system into resonance $\omega_z^{eff} \to 0$ to drive Rabi oscillations between the electron spin and the collective nuclear state, see figure 5.8b. Pulsing the appropriate effective field permits a controllable map between the electron spin state and the collective nuclear degrees of freedom spanned by $|0\rangle$ and $|1\rangle = \hat{A}_+ |0\rangle$. In addition, more complicated sequences of electron-nuclear spin interaction and electron spin manipulation allow for arbitrary two qubit operations on $|\uparrow\rangle, |\downarrow\rangle$ and $|0\rangle, |1\rangle$ (see Ref. [144] and commentary therein).

Measurement and initialization proceed in much the same manner as described for NV centers. The state of the electron spin system can be read out by exciting a cycling transition with resonant σ_+ light, and measurement and ESR (or Raman transitions) can be employed to initialize the system in the desired state. As the effective Knight shift of the electron spin is negligible on the time scales of entanglement preparation, the collective nuclear state's coherence is unaffected by this process. Due to the improved selection rules and possibility of Raman transitions, it may be more effective to use the Raman entanglement generation scheme.

The nuclear state of the quantum dot can be prepared by cooling the nuclear spins using preparation of electron spin and manipulation of the effective magnetic field [147]. In practice, this leaves the nuclear system in a state $|\mathcal{D}\rangle$ with the same symmetry properties as the state $|0\rangle$ described above [146]. To date, 60% nuclear spin polarization has been achieved by optical pumping in GaAs quantum dots [141]. As was the case with NV centers, the nuclear spin state can be read out by preparing

the electron spin in the $|\downarrow\rangle$ state, mapping the nuclear state to the electron spin state, and measuring the electron spin state.

5.5.3 Atomic Physics Implementation

Compared to the solid state implementations we have considered so far, implementations in single trapped atoms or ions have the advantage that they typically have very little broadening of the optical transitions. Because atomic systems do not reside in a complicated many-body environment, their internal degrees of freedom can have very long coherence times. For most atomic systems, however, it is hard to identify a mechanism which allows one degree of freedom, e.g., the nuclear spin, to be decoupled while we probe some other degree of freedom, e.g., the electron spin. Below we describe a system which does fulfill this requirement, although practical considerations indicate implementation may be challenging.

We consider alkali-earth atoms, such as neutral magnesium, and chose an isotope with non-vanishing nuclear spin (^{25}Mg). The lowest lying states of magnesium are shown in Fig. 5.9 (electronic structure only). Instead of the electronic spin states we have considered so far, i.e., for NV centers and quantum dots, we will use states which differ both in spin and orbital angular momentum. The stable ground state $^1S_0$ will serve as state $|0\rangle$. In this state, the electronic degrees of freedom have neither spin nor orbital angular momentum and the nuclear spin is thus decoupled from the electronic state. The excited state $^3P_0^o$ (whose hyperfine interactions also vanish to leading order) will provide state $|1\rangle$. Note that the triplet-singlet transition from $^3P_0^o$ to the ground state is highly forbidden and this state has an extremely long lifetime,

but transitions between the two states can still be induced with a strong laser.

To create entanglement we couple the ground state to the excited state $^1P_1$ with a laser field and collect the scattered light. From this excited state the atom essentially always decays back into the ground state. If the driving is detuned much further than the hyperfine splitting in the excited state, the nuclear spin is also decoupled during this process. The nuclear spin can therefore by used to store information while we entangle the electronic state with another atom. Finally, to implement gates between the electronic and nuclear states one should, for instance, couple the $|0\rangle$ state to another state in the atom where there is a hyperfine interaction, for example using resonant excitation of the $^1P_1$ state.

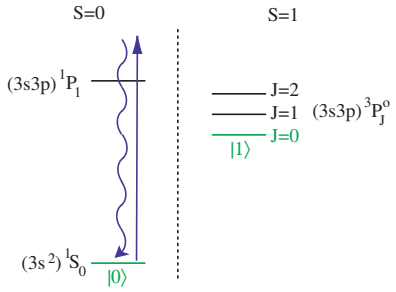

Figure 5.9: *Electronic level structure of atomic magnesium. The electronic ground state $^1S_0$ has vanishing spin and orbital angular momentum. In this state the nuclear spin therefore decouples from the electronic degrees of freedom. An entangling operation which is also insensitive to the nuclear degree of freedom can be achieved with lasers which are detuned much further than the hyperfine splitting in the $^1P_1$ level*

Finally, we note that all three physical implementations we suggest operate in the visible or near-IR, and will likely require high-efficiency frequency conversion to telecom wavelengths for low-loss photon transmission.

5.6 Conclusion

In conclusion, we propose a method for fault tolerant quantum communication over long distances requiring only probabilistic nearest-neighbor entanglement generation, two-qubits per node, and two-qubit operations. We compare several schemes for entanglement generation and discuss two solid-state systems and an atomic system which might be used to implement them. Potential applications include secure transmission of secret messages over intercontinental distances.

Chapter 6

Mesoscopic cavity quantum electrodynamics with quantum dots

6.1 Introduction

Recent progress in quantum control of atoms, ions, and photons has spurred interest in developing architectures for quantum information processing [148, 15, 149]. An intriguing question is whether similar techniques can be extended to control quantum properties of "artificial atoms" in a condensed matter environment. These tiny solid state devices, e.g. flux lines threading a superconducting loop, charges in cooper pair boxes, and single electron spins, exhibit quantum mechanical properties which can be manipulated by external currents and voltages [150, 151, 152, 153]. To realize their potential as highly tunable qubits, they must interact at a rate faster than the deco-

herence caused by the complex and noisy environment they inhabit. Strong coupling between qubits is therefore essential to achieve a high degree of control over quantum dynamics. For most systems a mechanism achieving the required coupling strength has only been proposed for nearby qubits [58], thus limiting the spatial extent of controllable interactions.

We describe a technique for coupling mesoscopic systems that can be millimeters apart. In our proposal, a strong interaction is obtained by linking charge qubits to quantized voltage oscillations in a transmission line resonator. We show that the capacitive coupling between charge degrees of freedom of the mesoscopic system and the superconducting resonator is formally analogous to cavity quantum electrodynamics (cavity QED) in atomic physics [27]. Such an interaction may be used for controllable coupling of distant mesoscopic qubits, thereby facilitating scalable quantum computing architectures. Furthermore, we have recently shown [60] that by combining the present approach with atom trapping above the resonator, these techniques may allow coupling between solid state and atomic qubits, thus opening a new avenue for quantum information research.

These new opportunities for qubit manipulation using microwave photons are made possible by the excellent coherence properties of high quality factor superconducting microstrip resonators originally developed for photon detection [154, 155]. With observed Q-factors exceeding 10^6 at 10 GHz, such resonators could permit on-chip storage of a microwave photon for more than 10 μs. Moreover, in contrast to the microwave cavities used in atomic cavity QED [156, 157, 158, 159], these 1D transmission line resonators have mode volumes far smaller than a cubic wavelength,

allowing a significantly stronger coupling to resonator modes. This combination of long coherence time and strong coupling makes microstrip resonators a promising technology for quantum manipulation.

In this chapter we outline several intriguing avenues for applications of these resonators in the context of quantum dot research. We first discuss a mechanism for strong coupling between spacially separated charge states in a mesoscopic system. We show in particular that the use of quantum dots may allow construction of novel quantum devices such as an on-chip double-dot microscopic maser [6, 156, 157, 158, 159]. Our discussion pertains to lithographically defined lateral double quantum dots [40], although the resonator coupling mechanism would apply equally to other mesoscopic systems.

Similar ideas for resonator mediated interactions have been developed in the context of superconducting qubits [160, 161, 162, 163]. Specifically, the strong-coupling mechanism analogous to that presented here has been proposed independently in [164]. Recently, a series of ground-breaking experiments has shown strong coupling between a Cooper-pair box and microwave photons in a resonator [43, 165, 166], and excited interest in coupling superconducting resonators to a variety of quantum systems [60, 167, 59].

Although coherence properties of charge states in quantum dots are likely worse than those of superconducting systems, quantum dots have two potential advantages: they are highly tunable, and the electrons they confine are not paired, allowing access to the electron spin. We show that the more stable spin degree of freedom may be accessed using techniques for quantum coherent manipulation initially developed

in atomic physics [168, 169]. In analogy to the use of Raman transitions in cavity quantum electrodynamics, the electron spin states can be coupled via a virtual charge state transition. Since the spin decoherence rate is far slower than the charge decoherence rate, the losses can thereby be greatly reduced. Finally, we explicitly address the effect of the resonator on radiative contributions to qubit decoherence, and demonstrate that the latter can be greatly suppressed.

Before proceeding, we also note important earlier work on cavity quantum electrodynamics with quantum dots in the optical regime [139], which differs qualitatively from the ideas discussed here.

6.2 Cavity QED with Charge States

6.2.1 The resonator-double dot interaction

We consider a single electron shared between two adjacent quantum dots whose energy eigenstates are tuned close to resonance with the fundamental mode of a nearby superconducting transmission line segment. The electron can occupy the left or right dot, states $|L\rangle$ and $|R\rangle$ respectively, and it tunnels between the dots at rate T (see Figure 6.1). A capacitive coupling C_c between the right dot and the resonator causes the electron charge state to interact with excitations in the transmission line. We assume that the dot is much smaller than the wavelength of the resonator excitation, so the interaction strength may be derived from the electrostatic potential energy of the system, $\hat{H}_{\rm Int} = e\hat{V}\upsilon|R\rangle\langle R|$, where e is the electron charge, $\hat{V}$ is the voltage on the resonator near the right dot, $\upsilon = C_c/(C_c + C_d)$, and C_d is the capacitance to ground

of the right dot.

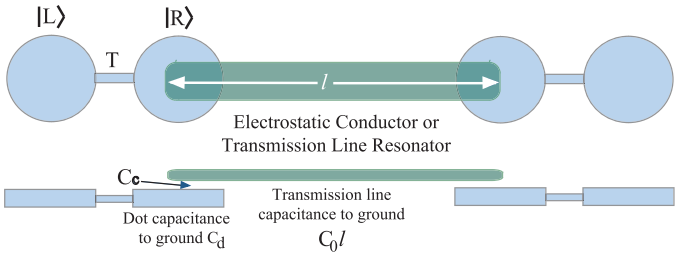

Figure 6.1: *Two double dots coupled by a conductor with capacitances as described in the text. Note that a transmission line resonator requires a nearby ground plane (not shown) to shield the system from radiative losses.*

A more useful form of the interaction Hamiltonian is found by rewriting this energy in a different basis. First, we express the left and right dot states $|L\rangle$ and $|R\rangle$ in terms of the double dot eigenstates. If the two dots are tunnel coupled with matrix element T and have a potential energy difference of Δ, then the double dot eigenstates are given by

$$|+\rangle = \sin\phi|L\rangle + \cos\phi|R\rangle \tag{6.1}$$

$$|-\rangle = \cos\phi|L\rangle - \sin\phi|R\rangle, \tag{6.2}$$

where $\tan\phi = -2T/(\Omega+\Delta)$ and $\Omega = \sqrt{4T^2+\Delta^2}$ is the splitting in frequency between the eigenstates $|+\rangle$ and $|-\rangle$. For notational simplicity, we represent the electron charge state in terms of Pauli spin matrices by defining raising and lowering operators $\Sigma_+ = \Sigma_-^\dagger = |+\rangle\langle-|$, so that $\Sigma_x = \Sigma_+ + \Sigma_-$, and so on.

Next, we express the voltage as an operator. A transmission line segment of length l, capacitance per unit length C_0 and characteristic impedance Z_0 has allowed wavevectors $k_n = \frac{(n+1)\pi}{l}$ and frequencies $\omega_n = \frac{k_n}{C_0 Z_0}$. Canonical quantization of the transmission line Hamiltonian allows the voltage to be written in terms of creation and

annihilation operators $\{\hat{a}_n^\dagger, \hat{a}_n\}$ for the modes k_n of the resonator. These excitations may be interpreted as microwave photons. With substitution of the quantized voltage at the end of the resonator,

$$\hat{V} = \sum_n \sqrt{\frac{\hbar\omega_n}{lC_0}} \left(\hat{a}_n + \hat{a}_n^\dagger\right), \tag{6.3}$$

the full Hamiltonian becomes

$$\hat{H} = \frac{\hbar\Omega}{2}\Sigma_z + \sum_n \hbar\omega_n \hat{a}_n^\dagger \hat{a}_n + \hbar(g_z^{(n)}\Sigma_z + g_x^{(n)}\Sigma_x)(\hat{a}_n^\dagger + \hat{a}_n). \tag{6.4}$$

The coupling constants, $g_x^{(n)} = g_0(T/\Omega)\sqrt{\omega_n/\omega_0}$ and $g_z^{(n)} = g_0(\Delta/2\Omega)\sqrt{\omega_n/\omega_0}$ scale as an overall coupling strength

$$g_0 = \omega_0 \upsilon \sqrt{\frac{2Z_0}{R_Q}} \tag{6.5}$$

where $R_Q = \frac{h}{e^2} \approx 26$ kOhm is the resistance quantum.

For $g_0 \ll \omega_0$ (which is guaranteed for low-impedance resonators $Z_0 \ll R_Q$) the Hamiltonian of Eq. (6.4) may be further simplified by neglecting all terms which do not conserve energy: If the dot is near resonance with the fundamental frequency, $\omega_0 = \frac{\pi}{lZ_0C_0} \approx \Omega$, we may neglect all other modes, and in the rotating wave approximation (RWA) the Hamiltonian reduces to

$$\hat{H} \approx \hat{H}_{\rm JC} = \frac{\hbar\Omega}{2}\Sigma_z + \hbar\omega_0 \hat{a}^\dagger \hat{a} + \hbar g_0 \frac{T}{\Omega}(\hat{a}^\dagger \Sigma_- + \hat{a}\Sigma_+). \tag{6.6}$$

The Jaynes-Cummings interaction described by Eq. (6.6) furnishes a direct analogy to a two-level atom coupled to a single mode field. A novel feature of the double dot system is that the parameters $\Omega(t)$ and $T(t)$ can be adjusted on fast time scales by varying the voltage applied to the metallic gates defining the quantum dots. Consequently the detuning $\Omega(t) - \omega_0$ and the effective coupling constants $\propto \frac{T(t)}{\Omega(t)}$ may be

controlled independently for double dots on either end of the resonator, each of which interacts with the resonator via the coupling described by Eq. (6.6).

To illustrate the strength of the resonator mediated interaction rate Tg_0/Ω, we compare it with a static interaction achieved by capacitively coupling spatially separated double dots through a conductor. By calculating the change in electrostatic energy of an electron in one double dot due to shifting the electron between dots in the second double dot, we find that the electrostatic interaction energy is $\Delta E \approx \upsilon^2 e^2/(C_0 l)$. If the nonresonant conductor and the transmission line have the same length l and capacitance to ground C_0, the two interaction rates may be compared directly:

$$\hbar g_0 = \frac{1}{\upsilon}\Delta E\sqrt{\frac{R_Q}{2Z_0}}. \tag{6.7}$$

Typically, $Z_0 = 50$ Ohms $\ll R_Q$ and careful fabrication permits a strong coupling capacitance, with $\upsilon \approx 0.28$ [170], so that $\hbar g_0 \approx 57\Delta E$. Hence a much stronger coupling can be achieved using the resonant interaction. For example, a wavelength $\lambda \approx 2$ mm in GaAs corresponds to a frequency of $\omega_0/2\pi \approx 50$ GHz, yielding an extremely large coupling constant $g_0/2\pi \approx 870$ MHz.

In atomic systems, the photon decay rate κ often limits coherent control. In the solid state, superconducting transmission line resonators developed for high speed circuitry and photon detection have been produced with Q-factors up to 10^6 [154, 155]; the photon decay rate $\approx \omega_0/Q$ can thus be very small. The limiting factor is the charge state dephasing rate γ_c. Inelastic transition rates [171] set a lower bound of a few hundred MHz, and initial observations of coherent charge oscillations reveal a dephasing time near 1 ns, limited by relatively hot (100 mK) electron temperatures

[46]. For our calculations, we make the conservative estimate $1/\gamma_c \approx 1$ ns, noting that the zero temperature value could be an order of magnitude slower. Regardless of the precise dephasing rate, quantum dot charge states would make rather poor qubits. Consequently for application to quantum information we must extend the strong charge state coupling to the spin degree of freedom, which decoheres on much longer timescales.

Nevertheless, initial demonstrations of cavity quantum electrodynamics may be possible using only the charge states. Stimulated emission of photons by a double quantum dot has previously been observed using external microwave radiation to enhance tunneling rates [40]. If the external source is replaced by the intracavity field of a microwave resonator, stimulated emission can exponentially amplify the field. For large enough coupling g_0, the double dot can potentially act as an on-chip maser.

6.2.2 The double dot microscopic maser

A double dot operated in the high-bias regime (see Figure 6.2) can convert electronic potential energy to microwave photons. By pumping electrons through the double dot, one might hope to induce a population inversion to amplify an applied microwave excitation. Note that such a device is based on a single emitter, and thus may have properties that differ significantly from those of conventional masers. In fact, the double dot device corresponds to a direct analogue of the microscopic maser (micro-maser) that has been extensively studied in atomic physics [6]. The micro-maser can be used for unique studies of quantum phenomena including generation of non-classical radiation fields and their non-trivial dynamics [156, 157, 158, 159].

In this chapter we will be interested only in the general feasibility of the on-chip micro-maser, and thus we analyze it semiclassically within a rate equation approximation. In this approximation, effects associated with quantum statistics of the generated field are disregarded. Such analysis does however provide a reasonable estimate for the threshold condition and general power.

The double dot system under consideration has left and right barriers which allow tunneling from the source and to the drain with strength Γ_L and Γ_R respectively, and one of the dots is capacitively coupled to a resonator as in Figure 6.1. By maintaining a potential energy difference between the two leads, a current is driven through the double dot, and each electron passing through the dot can stimulate emission of a photon into the resonator. To operate as a maser, however, the double dot must exhibit population inversion, which can only be achieved if electrons preferentially flow in through the excited state and leave via the ground state. Since finite tunnel coupling $T > 0$ is required in order to emit photons into the resonator, both the excited and ground states $|\pm\rangle$ must be partially delocalized. This allows electrons to tunnel directly from the source to the ground state and vice versa. Moreover inelastic decay processes limit how effectively the double dot can convert population inversion into photons. A careful treatment of pumping and decay rates is therefore needed to demonstrate maser action.

Our semiclassical analysis treats the double dot quantum mechanically, but assumes that the resonator excitations can be described by a coherent state. We use the density matrix formalism in the rotating wave approximation to derive equations governing the behavior of a double dot coupled to a coherent state of the resonator

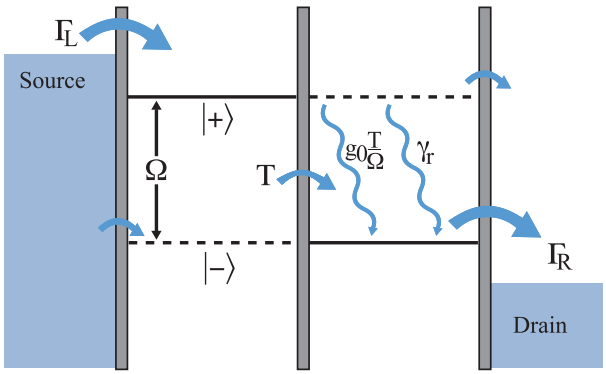

Figure 6.2: *The double dot configuration is illustrated in the charge eigenbasis,* $|+\rangle, |-\rangle$. *Electrons tunnel from the source into the left dot at rate* Γ_L *and from the right dot to the drain at rate* Γ_R. *For a finite detuning* Δ, *this pumping can lead to a population inversion. Decay from the excited* $|+\rangle$ *state to the ground* $|-\rangle$ *state occurs via photon emission into the resonator and also via phonon-mediated inelastic decay processes.*

$\hat{a}|\alpha\rangle = \alpha|\alpha\rangle$. From Eq. (6.6), one can show that the slowly varying components of the density matrix $\hat{\rho}$ in the eigenbasis $\{|+\rangle, |-\rangle\}$ evolve as

$$\begin{aligned} \dot{\rho}_{++} &= i\alpha\tfrac{g_0 T}{\Omega}\left(\rho_{+-} - \rho_{-+}\right) \\ \dot{\rho}_{+-} &= -i\delta\omega\rho_{+-} + i\alpha\tfrac{g_0 T}{\Omega}\left(\rho_{++} - \rho_{--}\right), \end{aligned} \tag{6.8}$$

where $\delta\omega = \Omega - \omega_0$, $\dot{\rho}_{--} = -\dot{\rho}_{++}$, and $\dot{\rho}_{-+} = (\dot{\rho}_{+-})^*$.

In addition to this coherent evolution, the density matrix components are affected by dephasing, decay, and coupling to the leads. In particular, the excited state population ρ_{++} increases at a rate $\Gamma_L|\langle +|L\rangle|^2(1 - \rho_{++} - \rho_{--})$ due to pumping from the source, while it decays at rate $\gamma_r + \Gamma_R|\langle +|R\rangle|^2$ due to relaxation to the ground state at rate γ_r and loss to the drain. Similarly, the ground state population ρ_{--} increases at a rate $\Gamma_L|\langle -|L\rangle|^2(1 - \rho_{++} - \rho_{--}) + \gamma_r\rho_{++}$, while losing population at rate $\Gamma_R|\langle -|R\rangle|^2\rho_{--}$. Note that our density matrix no longer satisfies $\mathrm{Tr}(\rho) = 1$ (since the electron can leave the double dot), and we have accounted for the large charging

energy by allowing at most one electron to inhabit the double dot [172].

The pumping and decay rates also contribute to reduction of the off-diagonal terms ρ_{+-}, ρ_{-+}. Inelastic decay contributes $\gamma_r/2$ to the charge dephasing rate γ_c. The coupling to the leads, however, enters in an asymmetric fashion because Γ_R causes direct lifetime broadening, whereas Γ_L only affects dephasing through virtual processes which allow the confined electron to scatter off electrons in the source. We consider the regime $\Gamma_R \approx \Gamma_L$, where these higher order processes can be neglected in comparison to lifetime broadening, and thereby find that the off-diagonal terms decay at a rate $\gamma_{tot} = (\gamma_r + \Gamma_R)/2 + \gamma_c$.

Taking all terms into account, the density matrix equations of motion are:

$$\begin{aligned}
\dot{\rho}_{++} &= i\alpha\tfrac{g_0 T}{\Omega}\left(\rho_{+-} - \rho_{-+}\right) - \left(\gamma_r + \Gamma_R\tfrac{\Omega-\Delta}{2\Omega}\right)\rho_{++} \\
&\quad + \Gamma_L\tfrac{\Omega+\Delta}{2\Omega}\left(1 - \rho_{++} - \rho_{--}\right) \\
\dot{\rho}_{--} &= i\alpha\tfrac{g_0 T}{\Omega}\left(\rho_{-+} - \rho_{+-}\right) - \Gamma_R\tfrac{\Omega+\Delta}{2\Omega}\rho_{--} + \gamma_r\rho_{++} \\
&\quad + \Gamma_L\tfrac{\Omega-\Delta}{2\Omega}\left(1 - \rho_{++} - \rho_{--}\right) \\
\dot{\rho}_{+-} &= -(\gamma_{tot} + i\delta\omega)\rho_{+-} + i\alpha\tfrac{g_0 T}{\Omega}\left(\rho_{++} - \rho_{--}\right)
\end{aligned} \tag{6.9}$$

where $\dot{\rho}_{-+} = (\dot{\rho}_{+-})^*$. In the steady state, the time derivatives vanish, and one may easily obtain the polarization $\mathrm{Im}[\rho_{+-}]$ and population inversion $\rho_{++} - \rho_{--}$.

Simulated emission processes increase the intracavity field. The amplitude of the coherent state, α, grows as $(g_0 T/\Omega)\mathrm{Im}[\rho_{+-}]$ while decaying at rate $\kappa\alpha$ due to the finite linewidth of the resonator. Expressed in terms of the effective emission rate, $G = (g_0 T/\Omega)^2\gamma_{tot}/(\gamma_{tot}^2 + \delta\omega^2)$, the field growth rate is $\dot{\alpha} = \alpha\left(G\left(\rho_{++} - \rho_{--}\right) - \kappa\right)$.

Substituting the steady state population inversion, we find the evolution equation for the microwave field:

$$\begin{aligned}\dot{\alpha} &= \left(\frac{2G\Omega\Gamma_L(\Delta\Gamma_R-\gamma_r\Omega)}{(\Gamma_R+2\Gamma_L)(\Omega^2(4G\alpha^2+\gamma_r)+2T^2\Gamma_R)+\Delta\Gamma_R(2\Delta\Gamma_L+\Omega\gamma_r)}\right)\alpha \\ &\quad -\kappa\alpha.\end{aligned} \tag{6.10}$$

This expression allows derivation of the threshold condition for maser operation, which corresponds to the requirement that the initial growth rate be greater than zero $(\dot{\alpha}/\alpha)\,|_{\alpha=0} > 0$. Due to saturation effects from the α^2 in the denominator of Eq. (6.10), the field α grows until $\dot{\alpha} = 0$. This steady state solution α_{ss} determines the number of generated photons, α_{ss}^2, which we identify as the double dot maser figure of merit because it quantifies the amplitude of the microwave field attained in the resonator.

The double dot maser cannot be made arbitrarily powerful by increasing the pumping power. Although increasing $\Gamma_{L,R}$ pumps more electrons through the double dot, opening up conduction to the leads speeds up the dephasing rate, which decreases the effective emission rate G. Consequently there is an optimal pumping rate which maximizes the steady state intracavity field.

To demonstrate the feasibility of building a double dot maser, we calculate the threshold current and maximum field α_{ss}^2 for a realistic set of parameters (see Figure 6.3). The threshold condition $\dot{\alpha} > 0$ can be satisfied even for a dot-resonator coupling rate of only $g_0/2\pi = 30$ MHz. For the calculations shown in Figure 6.3, we take $\Gamma_L = \Gamma_R = \Gamma$, and moderate values of Γ and g_0 yield typical resonator excitations of $|\alpha_{ss}|^2 \approx 1000$ photons. A weak coupling to a nearby transmission line can leak these excitations at a rate $1/\kappa \sim 1$ μs without significantly affecting the Q of the resonator, allowing emission of around 10^9 photons per second. The resulting

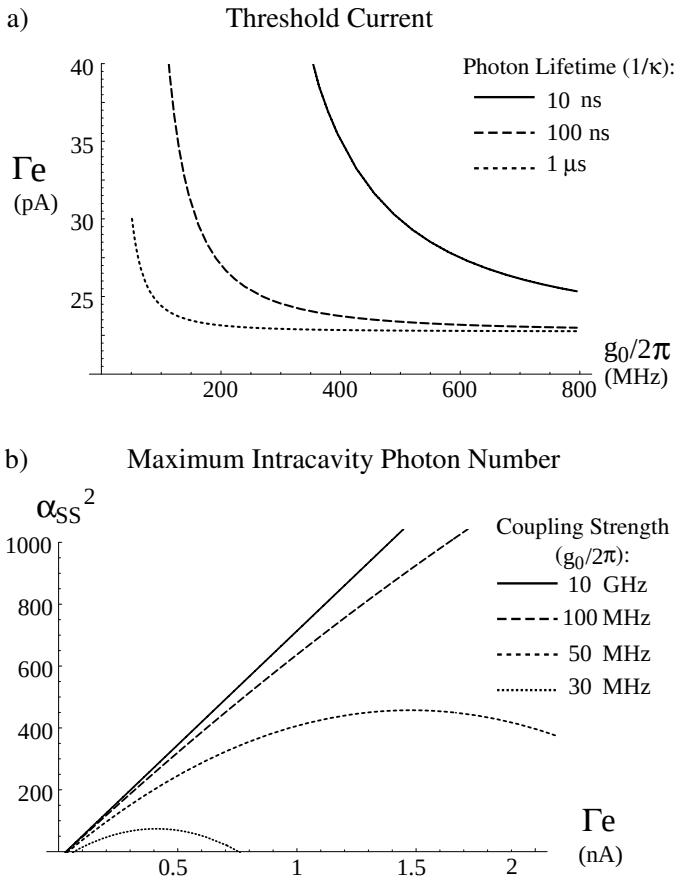

Figure 6.3: *a) The threshold pumping current* $e\Gamma$ *required for maser operation is shown as a function of dot-resonator coupling strength for three values of* κ*, the rate at which photons leak out of the resonator. b) The maximum number of photons produced in the resonator as a function of the pumping current* $e\Gamma$ *shows saturation due to* Γ*-induced dephasing. Note that the required coupling strength is low:* $g_0/2\pi \sim 100$ *MHz. The relevant parameters for these calculations are:* $\Gamma_L = \Gamma_R = \Gamma$*,* $\Delta/T = 2, \delta\omega = 0, 1/\gamma_c = 1$ *ns,* $1/\gamma_r = 10$ *ns, and in part b)* $1/\kappa = 1$ μs*.*

power at 30 GHz is around 20 fW. Although these fields are small, they could be detected by photon-assisted tunneling in another mesoscopic two-level system. For example, recent experiments on a superconductor-insulator-superconductor junction have shown a sub-fW sensitivity to microwave excitations at 25 GHz [173]. In conjunction with such sensitive microwave detectors, this on-chip coherent microwave source could provide a useful tool for high frequency spectroscopy of mesoscopic systems.

6.3 Cavity QED with Spin States

The spin state of an electron in a quantum dot has been suggested as a potential solid state qubit because it possesses good coherence properties [58]. While a quantitative value for the spin dephasing rate γ_s is unknown, a number of experiments indicate that it is significantly smaller than the charge dephasing rate. Experiments in bulk 2DEG find $1/\gamma_s = 100$ns [153], though the situation will be different for confined electrons. Spin relaxation times of over 50 μs [174, 171] indicate that the spin of an electron in a quantum dot can be well protected from its environment.

The spin does not couple directly to electromagnetic excitations in a resonator, but an indirect interaction is possible by entangling spin with charge. This technique is similar to Raman transitions in atomic systems, where long-lived hyperfine states interact via an intermediate short-lived excited state. In particular, by employing the analogue of a Raman transition, which only virtually populates charge state superpositions, we show below that quantum information can be transferred between the stable spin and photon states.

6.3.1 Three level systems in double dots

A technique based on Raman transitions requires a closed three level system incorporating both the charge and spin degrees of freedom (see Figure 6.4). We define the spin states $|\uparrow\rangle$ and $|\downarrow\rangle$ by applying a static in-plane magnetic field B_z, which splits them in energy by $\delta = g\mu_B B_z$ (6.2 GHz/Tesla for GaAs). The electron state is then represented by its charge and spin states $|\pm\rangle \otimes |\uparrow\downarrow\rangle$ which we abbreviate to $|\pm\uparrow\downarrow\rangle$. Since an electron in the orbital ground state $|-\rangle$ maintains its spin coherence over long times $\approx 1/\gamma_s$, we choose $|-\downarrow\rangle$ and $|-\uparrow\rangle$ as the two metastable states. The resonator couples $|-\uparrow\rangle$ to $|+\uparrow\rangle$; to complete the Raman transition, we need a mechanism which simultaneously flips the charge and spin state between $|+\uparrow\rangle$ and $|-\downarrow\rangle$. This can be accomplished with a local ESR (electron spin resonance) pulse $2\beta(t)\cos\nu t$ acting only on electrons in the left dot. By tuning the ESR carrier frequency ν close to the appropriate transition, $|-\downarrow\rangle \rightarrow |+\uparrow\rangle$, we need only consider the near-resonant terms of the local ESR Hamiltonian:

$$\hat{H}_{ESR} = \beta(t)\frac{T}{\Omega}(|+\uparrow\rangle\langle-\downarrow|e^{-i\nu t} + |-\downarrow\rangle\langle+\uparrow|e^{i\nu t}). \tag{6.11}$$

Choosing the ESR detuning $\Omega - \delta - \nu = \epsilon$ to match the resonator detuning $\Omega - \omega_0 = \epsilon$, we implement a far-off resonant Raman transition.

Several conditions must be met, however, in order to neglect the energy non-conserving processes as we did in Eq. (6.11). In particular, the ESR field must be sufficiently weak and sufficiently far detuned from resonance to satisfy the following three inequalities: $\beta \ll |\nu - \delta|$, $\beta \ll |\Omega + \delta - \nu|$, $(T/\Omega)^2 g_0\beta/\epsilon \ll \delta$. Physically, this means that the transition rates for undesired spin flips (e.g. $|+\uparrow\rangle$ and $|+\downarrow\rangle$) and the rate for Raman transitions between the wrong levels must both be small compared

to the energy detuning associated with each process. By going far off resonance, we also prevent the transition $|-\downarrow\rangle \rightarrow |+\downarrow\rangle$. Consequently, the system described by Eq. (6.11) and Eq. (6.6) is truncated to three states: $\{|-\uparrow,1\rangle, |-\downarrow,0\rangle, |+\uparrow,0\rangle\}$, where the final symbol indicates the number of excitations in the resonator. We have thus constructed a solid state analogue of the three-level atom of cavity quantum electrodynamics.

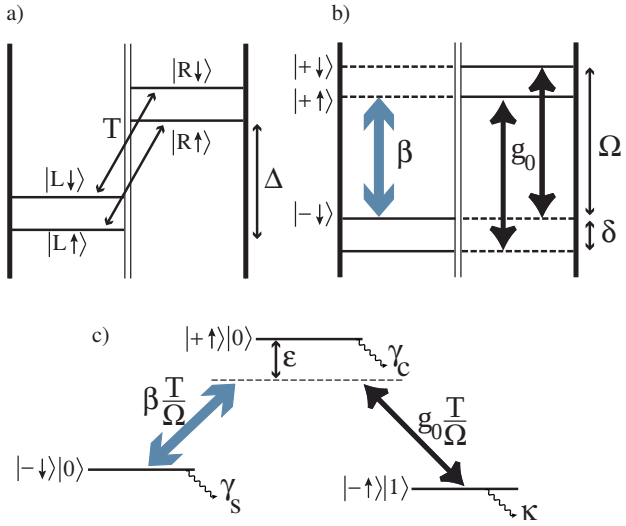

Figure 6.4: *a) An isolated double quantum dot has charge states detuned by Δ and tunnel coupled by T; the spin states are split by δ. b) In the double dot eigenbasis, an ESR pulse β applied locally to the left dot couples $|+\uparrow\rangle$ and $|-\downarrow\rangle$, while the resonator allows transitions between charge states accompanied by emission or absorption of a photon. c) The three level system has effective coupling strengths $\beta\frac{T}{\Omega}$ and $g_0\frac{T}{\Omega}$ and losses γ_c, γ_s, and κ due to charge, spin, and photon decoherence respectively. ESR and resonator frequencies $\nu = \Omega - \delta - \epsilon$ and $\omega_0 = \Omega - \epsilon$ respectively allow a resonant two photon transition between the spin levels.*

6.3.2 State transfer using a far-off-resonant Raman transition

The primary goal of the coupling mechanism is to allow interactions between spatially separated spin qubits. Since auxiliary adjacent spin qubits can accomplish conditional dynamics [58], long-distance state transfer is sufficient to attain this objective. In this section we present an analysis of the coupling rates and the loss of coherence associated with state transfer using a far-off-resonant Raman transition.

The two states $|-\uparrow,1\rangle$ and $|-\downarrow,0\rangle$ play the role of metastable atomic states, which are coupled via $|+\downarrow,0\rangle$, which acts as an intermediate excited state. For constant g_0 and β and large detuning ϵ, the metastable states are coupled at an effective transition rate $\chi = (T/\Omega)^2 g_0\beta/\epsilon$, and state transfer is achieved by pulsing T/Ω for a time $\tau = \pi/(2\chi)$.

Loss of coherence arises both from virtual population of the intermediate state and from dephasing of the spin and photon states. Virtual population of charge superpositions induces decoherence at a rate $\gamma_{\text{eff}} \approx (T/\Omega)^2 \left(P_\downarrow\beta^2 + P_\uparrow g_0^2\right)/\epsilon^2$ where $P_{\downarrow\uparrow}$ denotes the probability that the system is in the corresponding spin state. For β and g_0 of similar magnitude we approximate this decoherence rate by a time independent value $(T/\Omega)^2\langle\beta^2 + g_0^2\rangle/2\epsilon^2$. The metastable states decohere at rate γ_D, which is always less than the greater of γ_s and κ (strictly speaking, γ_D also depends on $P_{\uparrow\downarrow}$, but the dependence is weak since $\gamma_s \approx \kappa$). During the time required for state transfer, $\tau \approx \pi/2\chi$, the error probability is $p_{\text{error}} \approx \tau(\gamma_{\text{eff}} + \gamma_D)$. At optimal detuning

$$\epsilon \approx T/\Omega\sqrt{\gamma_c(\beta^2 + g_0^2)/2\gamma_D}, \tag{6.12}$$

the probability of error becomes

$$p_{\text{error}} \approx \sqrt{\gamma_c \gamma_D}\frac{\pi\Omega}{g_0 T}\sqrt{\frac{\beta^2 + g_0^2}{2\beta^2}}. \tag{6.13}$$

As a quantitative example of this technique, suppose $\Omega/2\pi = 2T/2\pi = 50$ GHz, $g_0/2\pi = 870$ MHz, and $1/\gamma_D$ is set by the expected spin dephasing time $\approx 1\mu$s (requiring a resonator quality factor $Q > 5 \cdot 10^4$). Using an ESR field $\beta/2\pi$ of 1 GHz, the far-off-resonant Raman transition accomplishes state transfer in around 100 ns with $p_{error} \sim 0.2$ for a detuning of $\epsilon/2\pi \approx 15$ GHz. These numbers easily satisfy the conditions on β which allow neglect of energy non-conserving processes. A high in-plane magnetic field B_z is not needed, since $\nu, \epsilon \gg \beta$, and $\chi/2\pi = 15$ MHz, so we merely require $B_z \gg 15$ mT (a low magnetic field is desirable because it presents fewer complications for the superconducting resonator design). We note that this example provides only a very rough estimate of expected error rates since they depends sensitively on the quantity of interest, the pulsing mechanism, and the values of γ_s and γ_c. Optimization of these variables could likely lead to significant improvements in fidelity.

6.3.3 Experimental Considerations

The proposed system fits into ongoing experimental efforts toward single spin initialization and readout [174]. Local ESR, however, has not yet been experimentally demonstrated, and will likely represent the most challenging element in our proposal. Nevertheless, a variety of tools are now being developed which may permit local spin manipulation. Consequently we now consider several strategies for achieving the simultaneous charge transition and spin flip required for our scheme.

One promising route to spin resonance is g-factor engineering [175]. In our proposal, even a static ESR interaction ($\nu = 0$) could be used to flip spins, provided that $\delta \gg \beta$. Modulation of one component of the g-factor tensor, e.g. g_{xx}, could thus turn on and off the effect of a static applied field B_x by modulating the Zeeman term $g_{xx}\mu_B B_x \sigma_x$ in the Hamiltonian. By making the electrodes small enough, this g-factor shift could be applied to a single dot. Although working near $\nu = 0$ will vastly reduce the heat load associated with ESR, the system will be more sensitive to low frequency fluctuations in the electromagnetic environment.

Alternately, high frequency anisotropic g-factor modulation can induce spin flips using a static magnetic field and microwave electric fields [41]. As in the case of static g-factor engineering, the electric field could be applied locally. The resulting ESR coupling strength depends on the voltage-induced change in anisotropic g-factor Δg_{xz} multiplied by the applied static field. If one can engineer $\Delta g_{xz} = 0.03$ (static g-factor engineering can induce $\Delta g_{zz} = 0.16$ [175]), a static magnetic field of 16 T would produce the desired local ESR strength. Operation at such large fields, however, would necessitate using a type II superconductor to construct the resonator. Since the flux-pinning mechanisms which allow high-field superconductivity also contribute to residual surface impedance, resonators constructed of type II materials would likely have lower quality factors.

Other strategies combine a global ESR pulse with some other mechanism that couples spin and charge, for example a spin-dependent tunneling rate. In this case, the charge eigenstates can be made different for the two spins, so that $\langle -_\downarrow | +_\uparrow \rangle = \eta \neq 0$ (here $|\pm_\sigma\rangle$ is the charge eigenbasis for an electron with spin σ). If the global

ESR strength is β_{global}, the coupling between $|+\uparrow\rangle$ and $|-\downarrow\rangle$ is $\eta\beta_{global}$ whereas the additional decoherence due to the slightly different charge distributions of $|-\uparrow\rangle$ and $|-\downarrow\rangle$ is only $\eta^2\gamma_c$. Sufficiently large β_{global} and small η permit state transfer with negligible contribution to dephasing.

6.4 Control of Low-Frequency Dephasing with a Resonator

Thus far we have assumed a single-mode resonator and included only energy-conserving processes. A more careful analysis incorporates the energy non-conserving terms of Eq. (6.4), which lead to corrections scaling as $g_{x,z}^2/\omega_n^2$. If the resonator has a minimum frequency $\omega_0 \gg g_0$, these terms are small and can be neglected. However, as the minimum frequency decreases, energy non-conserving terms may become important.

In an experimental implementation a major concern could be that coupling a double dot to a macroscopic resonator (which is in turn coupled to the environment) might drastically increase the charge decoherence rate. Consequently we examine the resonator modes more rigorously. Following [176, 177], we model the environment as a transmission line of length $L \to \infty$ capacitively coupled to the resonator, and diagonalize the resonator + transmission line system (see Figure 6.5a). The discrete mode operators $\hat{a}_n, \hat{a}_n^\dagger$ are replaced by the creation and annihilation operators $\hat{A}_k, \hat{A}_k^\dagger$ for the eigenmodes of the total infinite system, which have a continuous spectrum of modes. Since arbitrarily low frequencies are represented, the corrections $\propto (g_{x,z}^{(k)}/\omega_k)^2$

may no longer be negligible.

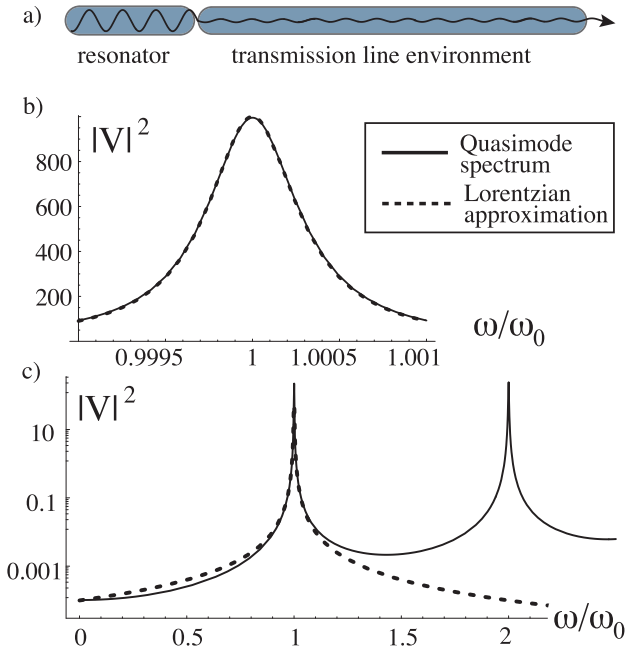

Figure 6.5: *a) Losses in the resonator may be modeled by a weak coupling to a semi-infinite transmission line. b) For a high-Q resonator, the quasimode voltage spectrum at $x = -l$ (solid) is well approximated near the fundamental mode by a Lorentzian (dashed) with half width ω_0/Q. c) A logarithmic plot of the same fit shows that the Lorentzian approximation provides an upper bound on the effects of dephasing due to low-frequency modes.*

If the double dot were coupled directly to a transmission line, the low-frequency dephasing would indeed pose a problem. However, the effect is mitigated because the resonator is only sensitive to environmental noise within ω_0/Q of the resonant frequency. For high quality factors, the resonator voltage spectrum at quasimode frequencies near and below the fundamental mode approaches a Lorentzian (see Figure 6.5),

$$|V_k|^2 \approx \frac{\hbar\omega_k}{2C_0L}\frac{Q\omega_0^2}{Q^2(\omega_k-\omega_0)^2+\omega_0^2}, \tag{6.14}$$

which vanishes as $\omega_k \to 0$. The coupling strength $g_{x,z}^{(k)}$ between the quantum dot and

the quasimode is proportional to this voltage, so the problematic coupling to low frequency modes is strongly suppressed.

To illustrate the suppression of decoherence, consider the dephasing effect of the term $\sum_k g_z^{(k)}(\hat{A}_k + \hat{A}_k^\dagger)\Sigma_z$ in the Hamiltonian of Eq. (6.4) in two situations: (a) the double dot is coupled directly to the environment, so A_k annihilates a mode of a semi-infinite transmission line, and (b) the double dot is coupled to a resonator which is in turn coupled to a transmission line environment, so A_k annihilates a quasimode of the resonator+transmission line system. To calculate dephasing, we start in the vacuum state for electromagnetic degrees of freedom and require that the coupling $g_z^{(k)}$ is gradually turned on and off with time dependence $f(t) = \int_{-\infty}^{\infty} e^{i\omega t}\tilde{f}(\omega)d\omega$. After tracing over the transmission line degrees of freedom, the component $|+\rangle\langle -|$ of the reduced charge state density matrix has decreased by $e^{-2\kappa_a}$ in case (a) and $e^{-2\kappa_b}$ in case (b) where

$$\kappa_a = \int_0^\infty \frac{LZ_0C_0}{\pi}|g_0\tilde{f}(\omega)|^2 d\omega \tag{6.15}$$

$$\kappa_b = \int_0^\infty \frac{LZ_0C_0}{\pi}\frac{Q\omega_0^2|g_0\tilde{f}(\omega)|^2}{Q^2(\omega-\omega_0)^2+\omega_0^2}d\omega. \tag{6.16}$$

Assuming a slowly varying $f(t)$ and a high-Q cavity, examination of Eq. (15,16) directly yields

$$\frac{\kappa_b}{\kappa_a} \approx \frac{1}{Q} \tag{6.17}$$

i.e. the low-frequency dephasing of the qubit is greatly suppressed. This result indicates that in situations where the double dot dephasing is dominated by coupling to electromagnetic modes of the transmission line, a resonator provides good protection from low-frequency dephasing.

6.5 Conclusion

In this chapter we describe how effects familiar from atomic cavity quantum electrodynamics may be observed in highly tunable solid state devices. Quantum dot charge states are limited by a fast decoherence rate, but a solid state maser may nonetheless demonstrate coherent interactions between a double dot and a resonator. For quantum information systems, lower decoherence rates are required, and we have illustrated how a long-range interaction between long-lived spin states may be implemented with only virtual population of intermediate charge states. This system represents an opportunity to manipulate electron spins and charges with a level of control usually associated with atomic physics, and illustrates how techniques pioneered quantum optics can find application in a solid state context.

On a broader level, our work also demonstrates how a high-quality resonator can serve as a quantum coherent data bus between qubits. Such a data bus could provide an interaction between different types of quantum systems. Cooper pair boxes [43], Rydberg atoms [60], or even molecules [167, 59] could thereby interact with electron spins. If sufficiently strong coupling mechanisms can be found, these artificial atoms and microwave resonators could have an important role to play as tunable, integrable, and scalable coherent quantum systems.

Chapter 7

Conclusion and outlook

7.1 The quantum network

Single quantum systems provide a fertile ground for exploring fundamental questions regarding their interactions with a complex environment, and present an opportunity for engineering quantum devices. Many applications in quantum information science, however, require a vast number of interconnected quantum systems. Quantum states of light present a natural link, allowing strong interactions between quantum states of matter separated by macroscopic distances. The concept which emerges from these considerations is a quantum network, where nodes comprised of a few controllable quantum bits are linked by photonic channels.

The research presented in this thesis takes a few different approaches toward realizing such a quantum network. Electrons confined to double quantum dots could potentially interact over long distances via microwave photons. However, the charge and spin dephasing times in typical semiconductors are very short, limiting applica-

tions with current materials. Spin degrees of freedom associated with defect centers present a particularly promising route, and the bulk of this thesis has been devoted to experimental and theoretical investigation of nitrogen-vacancy centers in diamond. Although many aspects of this vision remain speculative, it appears feasible that we may one day construct a quantum network from optically linked NV centers.

7.2 Quantum registers

Each node in a quantum network is formed by a quantum register consisting of two or more qubits, which must satisfy the following two requirements: First, one must be able to manipulate each qubit and perform gates between qubits within the register, exemplified by a quantum memory operation. In effect, each register must function as a few-qubit quantum computer. The second requirement is that one must also be able to entangle one qubit in the register (e.g. the electron spin) with another qubit in a different register, without affecting the rest of the original register (e.g. several nuclear spins). If one could deterministically generate high-fidelity entanglement between registers, this requirement would also be satisfied, but deterministic entanglement generation has proved difficult to accomplish. Relying on probabilistic entanglement means that the nuclear spins must survive many attempts to entangle the electron spin with a remote register.

These two requirements present a delicate balancing act. The qubits composing the register must interact strongly enough to function as a quantum computer, but weakly enough that they can be isolated during entanglement generation. Alternately, it must be possible to turn the interactions on and off. Trapped ions offer a potential

solution to both requirements, since ions interact strongly when confined to the same trap, but weakly when isolated in separate traps. Solid-state devices such as quantum dots, whose interaction parameters can be determined by applied voltages, may also satisfy these constraints. In the case of NV centers in diamond, we contend with dipole-dipole interactions between spins localized to fixed lattice sites, which cannot be switched on and off. The two requirements can nevertheless be simultaneously satisfied by switching the magnetic field on and off. In zero magnetic field, photons emitted on the $m_s = 0$ transition should carry no information about the nuclear spin state, allowing remote entanglement of the electron spin without touching the nuclear spins.

7.3 Towards quantum registers in diamond

The experimental work described in Chapters 2-4 lays the groundwork for development of a quantum register composed of coupled electron and nuclear spins in diamond. Nevertheless, several advances in materials engineering and spectroscopy will be required to develop the nitrogen-vacancy center into a viable candidate as a quantum register.

In the experiments presented in this thesis, operations on the nuclear spins are done entirely by driving the electron spin and allowing the nuclear spin to precess freely along the two magnetic field orientations associated with the $m_s = 0$ and $m_s = 1$ manifolds. This limits the fidelity of operation to the degree of g-tensor enhancement by the electron spin. By driving the nuclear spin transitions directly with RF excitation at the hyperfine interaction frequency $\omega_{j,1}$, we could greatly reduce

the amount of time required to manipulate the nuclear spin.

The fidelity of operations between electron and nuclear spins can be further improved by using isotope engineered diamond samples. Currently, the quantum register operations are limited by undesired coupling to the native ^{14}N nuclear spin (I = 1) and coupling to the spin bath of ^{13}C nuclear spins. For example, by implanting ^{15}N [97] into pure ^{12}C diamond one could engineer NV centers with a native $I = 1/2$ nuclear spin while eliminating the dominant dephasing mechanism (coupling to the ^{13}C spin bath). Multiple nuclear spins would require working with ^{15}N implanted in reduced-concentration ^{13}C samples, and searching long enough to find an NV center with a nearby ^{13}C, or implanting ^{13}C along with ^{15}N.

Currently there has been no experimental investigation into entangling the electron spin of an NV center with an outgoing photon, but recent optical spectroscopy [78, 94] indicates that it may be possible. In particular, measurements of the linewidth of the optical transitions suggest that the emitted photons are very nearly radiatively broadened, substantially reducing the difficulty of spin-photon entanglement. Practically, it may be necessary to incorporate a cavity to enhance the percentage of fluorescence emitted into the zero phonon line and increase collection efficiency. Special filtering techniques, above-band excitation, or two-photon transitions may be required to separate a laser used for excitation from the fluorescence. Nevertheless, there does not appear to be a fundamental roadblock to spin-photon entanglement.

It also appears feasible to perform entanglment operations without touching the quantum state of a nearby nuclear spin. In particular, because the nuclear spin does not dephase significantly under optical excitation (within the $m_s = 0$ manifold), by

exciting only the $m_s = 0$ transition it should be possible to entangle the state of the electron spin with the presence or absence of a photon, as described in detail in Chapter 5. Although the population in the $m_s = 1$ state will induce a phase on the nuclear spin, by repeating the procedure after an electron spin π pulse, this phase can be echoed away.

7.4 Conclusion

In conclusion, this thesis presents several ideas developed in the context of solid state quantum information science. In particular, it explores in detail an avenue towards implementing a quantum network using the nitrogen-vacancy center in diamond, and applying it to long-distance quantum communication. This type of quantum network may also have applications in quantum computing using teleportation-based gates [37], indicating its potential as a powerful and versatile tool for quantum information science.

Appendix A

Symmetry of the NV center

A.1 A brief exposition on symmetries, groups, and quantum numbers

The quantum numbers associated with atomic orbitals arise from the rotational invariance of the Hamiltonian which governs them. Similarly, an arbitrary symmetry of any Hamiltonian constrains the structure of its eigenstates. For example, suppose that the Hamiltonian of a system is invariant under the unitary operation $\hat{U}_a$, i.e. $\hat{U}_a \hat{H} \hat{U}_a{}^\dagger = \hat{H}$. Any solution to the Schroedinger equation,

$$\hat{H} \left|\psi_n\right\rangle = E_n \left|\psi_n\right\rangle , \tag{A.1}$$

must also satisfy

$$\hat{U}_a \hat{H} \hat{U}_a{}^\dagger \left|\psi_n\right\rangle = E_n \left|\psi_n\right\rangle \tag{A.2}$$

or, multiplying from the left by $\hat{U}_a{}^\dagger$,

$$\hat{H} \left(\hat{U}_a{}^\dagger \left|\psi_n\right\rangle\right) = E_n \left(\hat{U}_a{}^\dagger \left|\psi_n\right\rangle\right) . \tag{A.3}$$

This implies that the state under the symmetry transformation, $\hat{U_a}^\dagger |\psi\rangle_n$, must have the same energy E_n as the original state $|\psi_n\rangle$ [178].

Generally, there can be more than one symmetry operator for the system, and the set of operators $\{\hat{U_k}\}$ satisfying $\hat{U_k}\hat{H}\hat{U_k}^\dagger = \hat{H}$ is known as the symmetry group of the Hamiltonian. This set can easily be seen to be a group, since the system is invariant under the identity and also under any pair of symmetry transformations.

The symmetry properties reveal the structure of the degenerate energy levels of the system. One can obtain the members of a degenerate energy level by finding a single solution $|\psi_n\rangle$ and applying all of the members of the symmetry group to it: $\{\hat{U_k}^\dagger |\psi_n\rangle\}$. In general, however, the resulting set of states may contain duplicates. The set of distinct, degenerate states $\left|\psi_n^{(k)}\right\rangle$ are related to each other by a set of matrices $M_{k,l}$ (where $\left|\psi_n^{(k)}\right\rangle = \sum_l M_{k,l} \left|\psi_n^{(l)}\right\rangle$) which are an irreducible representation of the symmetry group[1]. Although abstract, these notions are important because they give us a means to classify the energy levels of the system according to how the states within those energy levels transform under symmetry operations.

A.2 C_{3V} symmetry

The NV center has a natural axis formed by the line connecting the nitrogen and vacancy sites (referred to as the NV axis). By examining the locations of the nearest-neighbor carbon atoms (see Fig. 2.1b), one can see that the diamond lattice

[1]The set $\{M\}$ are a representation of the group of symmetry operations if there exists a homeomorphism $T : U \to M$, i.e. a mapping which preserves multiplication: $U_a U_b = U_c \Rightarrow T(U_a)T_(U_b) = T(U_c)$. The representation $\{M\}$ is irreducible if it cannot be broken up into the direct sum of two or more representations (see e.g. [178] for greater detail)

surrounding the NV center is invariant under rotations by $2\pi n/3$ around the NV axis (represented by C_3 and C_3^{-1}). It is also invariant under reflections in a plane containing the NV axis and any of the three nearest-neighbor carbon atoms, (represented by R_1, R_2, and R_3). Together with the identity operation I, this set of operations $\{I, C_3, C_3^{-1}, R_1, R_2, R_3\}$ forms the symmetry group of the NV center, which is denoted C_{3v} [61].

There are three irreducible representations of the C_{3v} group, which are labelled A_1, A_2, and E according to Mulliken notation. A_1 and A_2 are one-dimensional representations: A_1 is simply the identity 1, while A_2 represents the rotations $\{I, C_3, C_3^{-1}\}$ by 1 and the reflections $\{R_1, R_2, R_3\}$ by -1. Energy levels of the NV center which correspond to these representations are nondegenerate, and the eigenstate associated with them transforms into itself under any of the symmetry operations, picking up a factor of -1 under reflections if it transforms as A_2. The remaining irreducible representation, E, is two-dimensional, which means that it corresponds to a degenerate energy level with two eigenstates that transform into each other as [178, 61][2]

$$T^{(E)}(I) = \begin{pmatrix} 1 & 0 \\ 0 & 1 \end{pmatrix} \quad T^{(E)}(C_3) = \begin{pmatrix} -\frac{1}{2} & -\frac{\sqrt{3}}{2} \\ \frac{\sqrt{3}}{2} & -\frac{1}{2} \end{pmatrix} \quad T^{(E)}(C_3^{-1}) = \begin{pmatrix} -\frac{1}{2} & \frac{\sqrt{3}}{2} \\ -\frac{\sqrt{3}}{2} & -\frac{1}{2} \end{pmatrix} \tag{A.4}$$

$$T^{(E)}(R_1) = \begin{pmatrix} 1 & 0 \\ 0 & -1 \end{pmatrix} \quad T^{(E)}(R_2) = \begin{pmatrix} -\frac{1}{2} & -\frac{\sqrt{3}}{2} \\ -\frac{\sqrt{3}}{2} & \frac{1}{2} \end{pmatrix} \quad T^{(E)}(R_3) = \begin{pmatrix} -\frac{1}{2} & \frac{\sqrt{3}}{2} \\ \frac{\sqrt{3}}{2} & \frac{1}{2} \end{pmatrix}.$$

Some understanding of allowed transitions between energy eigenstates of a system can be gained from symmetry considerations. A transition is dipole-allowed if there is overlap between the final state $|\psi\rangle_f$ and the initial state, acted upon by the

[2]There are, of course, many possible ways to write these matrices related by unitary transformations.

dipole operator $\hat{d}\,|\psi\rangle_i$. Symmetry can forbid the transition, however, if there is no component of $\hat{d}\,|\psi\rangle_i$ which belongs to the same representation as $|\psi\rangle_f$. To find these symmetry-forbidden transitions, we will need to write the dipole operator $\hat{d}$ in terms of operators which transform according to the irreducible representations above. For C_{3v} symmetry, the position operator $\hat{z}$ (along the NV axis) transforms as A_1, while $\{\hat{x}, \hat{y}\}$ transform as E. Consequently, if $|\psi\rangle_i$ belongs to the representation D, $\hat{d}\,|\psi\rangle_i$ will have some components which transform as $A_1 \otimes D = D$, and some which transform as $E \otimes D$. If none of the components transform as $|\psi\rangle_f$, then the transition is forbidden.

Using the direct products for the C_{3v} representations (where D could be A_1, A_2, or E),

$$A_1 \otimes D = D \quad A_2 \otimes A_2 = A_1 \quad E \otimes A_1 = E \quad E \otimes A_2 = E \tag{A.5}$$
$$E \otimes E = A_1 + A_2 + E,$$

we find that all transitions are dipole allowed except those which begin in A_1 and end in A_2 or vice versa.

Any additional degrees of freedom, such as spin, will change the structure of the eigenstates. For example, suppose we begin with an orbital level which transforms according to irreducible representation D, and consider what happens to this energy level if it is a spin triplet. Spin is an axial vector, so S_z transforms according to A_2, while S_x and S_y transform according to E. Consequently, the S_z component of the orbital level will transform as $D \otimes A_2$, and the S_x, S_y components will transform as $D \otimes E$, possibly splitting into three nondegenerate (or only accidentally degenerate) levels if $D = E$. In the literature, the S_z states are often referred to as $m_s = 0$ states,

while appropriate superpositions of $\{S_x, S_y\}$ are referred to as $m_s = \pm 1$. Although the orbital-and-spin levels may have considerably different symmetry properties from the initial orbital level, it is important to remember that the dipole operator acts only on the spatial degrees of freedom, so the selection rules are determined by the orbital transitions. In particular, this means that unless the spin states are mixed by some perturbation, the optical transitions should preserve the spin state.

Appendix B

Spin-dependent optical transitions in the NV center at rooom temperature

All of our measurements on the NV center electron spin have made use of optical spin polarization and detection. In Chapter 2, we presented a model for the mechanism underlying optical spin polarization and spin-dependent fluorescence. In this appendix, we discuss this model in greater detail, and compare its predictions to our experimental data.

B.1 Measurement of the electron spin polarization rate

To test the predictions of our model for the NV center, we have measured the rate at which green light polarizes the electron spin into the $m_s = 0$ state, as shown in Fig. B.1. The polarization rate is measured by first initializing the electron spin into $m_s = 0$ and then driving it into the $m_s = 1$ state with a microwave π pulse. A variable duration green pulse is then sent onto the sample, partially repolarizing the electron spin into a mixture of $m_s = 0$ and $m_s = 1$. Finally, the spin is measured by illuminating it again, counting the number of photons during a 300 ns "signal" counting period, and comparing that number to the number of photons obtained 1μs later during the "reference" counting period. Most of our data is taken under the same conditions as in Fig. B.1, i.e. with a green power $\sim 320\mu$W incident on the sample. Under these conditions, the electron spin polarizes into the $m_s = 0$ state with a $1/e$ time scale of ~ 150ns. This timescale determines the length of our signal and reference counting intervals, since we want those time intervals to be long enough to catch all of the differential emission, but not much longer than the polarization time. Note also that the waiting time between the signal and reference counting intervals, 1000 ns, is long enough that the spin has completely repolarized for the reference interval.

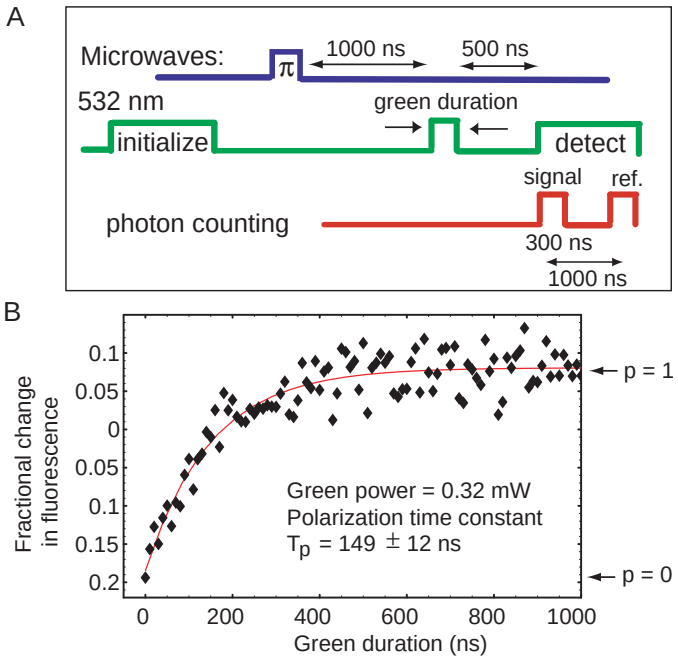

Figure B.1: *Measurement of the electron spin polarization rate under optical excitation. (A) Experimental procedure. (B) Sample data set for 0.32 mW green power, showing a characteristic polarization time of about 150 ns.*

B.2 Rate equation model

By measuring the electron spin polarization rate as a function of green power, we can test the suggested explanation of optical spin polarization and detection illustrated in Fig. 2.7. We will model the NV center by a five-level system, corresponding to two ground states $|1\rangle$ and $|2\rangle$, with $m_s = 0$ or $m_s = \pm 1$, two excited states $|3\rangle$ and $|4\rangle$ with $m_s = 0$ or $m_s = \pm 1$, and $|5\rangle$, the metastable singlet state. Since optical coherences decay quickly on the timescale of the dynamics in which we are interested, we can use a system of rate equations to model the optical transitions and only keep track of the population ρ_{ii} in each of the five levels.

The rate equations for the five-level model are

$$\rho'_{11} = -R_{\rm up}(1+\epsilon)\rho_{11} + \gamma\left(\rho_{33}+\epsilon\rho_{44}\right) + R_{\rm down}\left(\rho_{33}+\epsilon\rho_{44}\right) + \Gamma_D\rho_{55} \quad \text{(B.1)}$$

$$\rho'_{22} = -R_{\rm up}(1+\epsilon)\rho_{22} + \gamma\left(\rho_{44}+\epsilon\rho_{33}\right) + R_{\rm down}\left(\rho_{44}+\epsilon\rho_{33}\right) \quad \text{(B.2)}$$

$$\rho'_{33} = R_{\rm up}\left(\rho_{11}+\epsilon\rho_{22}\right) - \gamma(1+\epsilon)\rho_{33} - R_{\rm down}(1+\epsilon)\rho_{33} - k_{35}\rho_{33} + k_{53}\rho_{55} \quad \text{(B.3)}$$

$$\rho'_{44} = R_{\rm up}\left(\rho_{22}+\epsilon\rho_{11}\right) - \gamma(1+\epsilon)\rho_{44} - R_{\rm down}(1+\epsilon)\rho_{44} - k_{45}\rho_{44} + k_{54}\rho_{55} \quad \text{(B.4)}$$

$$\rho'_{55} = k_{35}\rho_{33} - k_{53}\rho_{55} + k_{45}\rho_{44} - k_{54}\rho_{55} - \Gamma_D\rho_{55}. \quad \text{(B.5)}$$

The parameters used in the equations are

$R_{\rm up}$ = Transition rate from ground to excited state induced by green excitation

$R_{\rm down}$ = Transition rate from excited to ground state induced by green excitation

ϵ = Small fraction of spin − non − conserving transitions

γ = Spontaneous decay rate

Γ_D = Spontaneous deshelving rate to $m_s = 0$ ground state $|1\rangle$

k_{35} = Shelving rate from $m_s = 0$ excited state $|3\rangle$

k_{45} = Γ_S = Shelving rate from $m_s = 1$ excited state $|4\rangle$

k_{53} = Deshelving rate to $m_s = 0$ excited state $|3\rangle$

k_{54} = Deshelving rate to $m_s = 1$ excited state $|4\rangle$.

The up- and down- transition rates are kept separate because the 532nm light excites a vibronic sideband which quickly decays via phonon emission to a different optically excited state which is not resonant with the green laser. In fact, for the simulations

shown below, we consider only upwards pumping $R_{\text{up}} = R$, with $R_{\text{down}} \approx 0$. For simplicity, only a single parameter ϵ describes the degree to which the optical transitions do not conserve spin, assuming that there is no difference in spin character between vibronic sideband excitation and emission. The spontaneous decay happens on a timescale of 12 ns or $\approx (2\pi)13$ MHz. Spontaneous deshelving to the $m_s = 0$ state is expected to occur on a timescale of 100 ns to 1μ s, from observations of increased fluorescence after a short delay following polarization [63]. The shelving rates are believed to be different for the different spin projections $k_{35} \ll k_{45}$. Finally, there may be a deshelving process $k_{53} \sim k_{54}$ [73, 84]. In particular, [63] calculates the following values for the rate equation parameters, which are used for the simulations shown in Fig. B.2A:

$$\begin{aligned} \epsilon\gamma &= 1.5 * 10^6 \text{s}^{-1} \\ \gamma &= 77 * 10^6 \text{s}^{-1} \\ \Gamma_D &= 3.3 * 10^6 \text{s}^{-1} \\ k_{45} &= 30 * 10^6 \text{s}^{-1} \\ k_{35} &= k_{53} = k_{54} = 0 \end{aligned}$$

B.3 Comparison to experimental data

The rate equations with the parameters given above are used to model the fluorescence observed from the NV center in our experiments. Initially, we assume that the population starts out in a mixture of $|1\rangle$ and $|2\rangle$ with populations $\rho_{11}(0) = \frac{1}{3}, \rho_{22}(0) = \frac{2}{3}$, as would be expected at room temperature. The simulations then follow the exper-

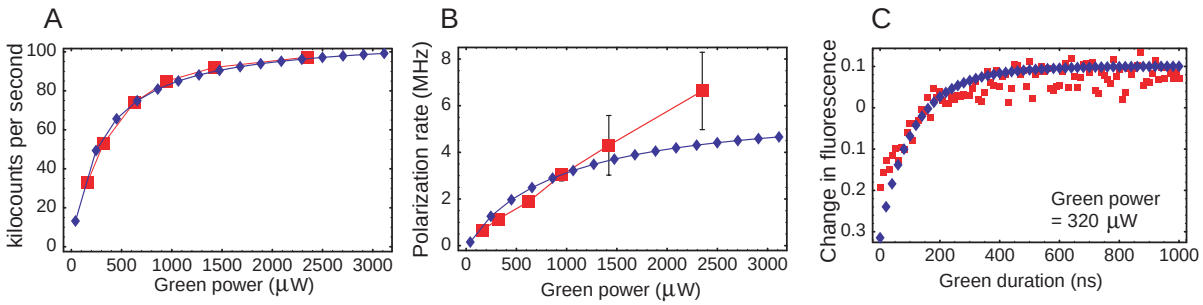

Figure B.2: *Comparison of simulations and experimental data for electron spin polarization. In all cases, blue diamonds show simulation results obtained using rate equation parameters from [63], and red squares show experimental data, both obtained using the pulse sequence shown in Fig. B.1A. (A) Steady-state fluorescence as a function of green power is used to calibrate units of R. (B) The electron spin polarization rate as a function of green excitation power R, using the calibration from (i) to convert from R to μW. (C) A sample curve showing the measured electron spin polarization rate as a function of green duration. The discrepancy at short times may arise from the finite switching time ∼ 50 ns for the AOM controlling the green laser.*

imental procedure (as shown, for example, in Fig. B.1A), and numerically integrate the rate equations through different intervals when the green light is switched on and off. Microwave excitation is assumed to be on resonance with the $|1\rangle \rightarrow |2\rangle$ transition, and effects of hyperfine structure are not included. The observed signal is calculated as the integral of the excited state population during the 300 ns signal counting period, while the reference counts are found by integrating the excited state population during the 300ns reference counting period which comes 1μs later:

$$\text{signal} = \gamma \int_{\text{sig}} (\rho_{33}(t) + \rho_{44}(t))\, dt \tag{B.6}$$

$$\text{reference} = \gamma \int_{\text{ref}} (\rho_{33}(t) + \rho_{44}(t))\, dt \tag{B.7}$$

$$\text{change in fluorescence} = \frac{\text{signal} - \text{reference}}{\text{reference}}. \tag{B.8}$$

In order to calibrate R relative to the measured green power (in μW), we compare the measured and calculated saturation curves (see Fig. B.2A), assuming that R is linear

in the green power. Once this calibration is performed, we can compare the simulated electron spin polarization rates to the measured ones, as shown in Fig. B.2B. Each point on the curves in Fig. B.2B comes from fitting an experimental data set and a simulation data set to an exponential decay. A sample polarization curve is shown in Fig. B.2C.

The rate equation parameters given in [63] provide a reasonable fit to our experimental data, as shown in Fig. B.2A. However, the observed electron spin polarization rate is nearly linear in green power, whereas the parameters from [63] predict a saturation effect. Because of the large experimental error bars at short switching times (arising from finite AOM response time and discrete pulsing intervals), we cannot rule out the model suggested by [63], although our results do suggest that there is another parameter in the rate equations which depends on the green power. For example, we can obtain a much better fit to our data by modifying a single parameter k_{45}, the shelving rate, so that it has a weak linear dependence on the green power. Nevertheless, the model proposed in [63] provides a reasonable agreement with our data, offers intuition for the underlying processes, and gives a plausible explanation for the observed optical spin polarization and spin-dependent fluorescence.

Using this model, we predict that we should be able to observe a $\sim 40\%$ change in fluorescence when we drive Rabi nutations (see Fig. B.3), which is close to the experimentally observed contrast of $20 - 40\%$. Furthermore, we can also investigate the degree of spin polarization obtained under optical excitation. According to this model, an initialization sequence consisting of 2μs illumination at 320μW power followed by a 1μs dark interval results in a preparation fidelity of $\sim 92\%$. This imperfect

polarization reduces the contrast by a factor of ~ 0.85, as shown in Fig. B.3. This

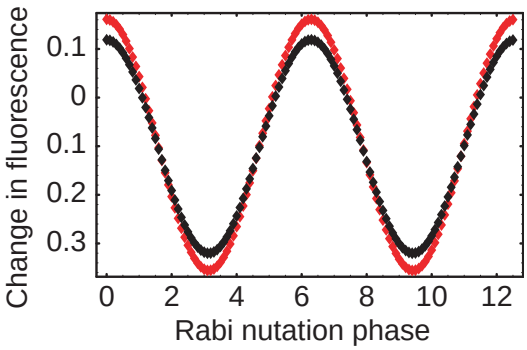

Figure B.3: *Expected Rabi nutation contrast in the rate equation model for perfect initial polarization (red) and the polarization predicted from the rate equations with parameters from [63] (black).*

model indicates that our assumption of perfect electron spin polarization is not entirely correct. However, other data [48] shows that the polarization is nearly perfect, indicating that the model parameters from [63] do not describe their system well. In fact, setting $\epsilon = 0$ results in perfect spin polarization (eliminating the difference between the two curves in Fig. B.3), but does not affect the degree to which the simulations shown in Fig. B.2 match the experimental data. It is possible that the some of the rate parameters vary from NV center to NV center, depending on the local crystal field.

The exact mechanism and degree of spin polarization thus remains an open question. These simulations serve to show that using the model from [63] our assumption of perfect polarization introduces only a small error $\sim 8\%$ in the fidelities we calculate.

Appendix C

The effect of shelving on probabilistic entanglement generation

In addition to the error arising from photon loss, we must consider what happens if the NV center shelves into the optically inactive metastable singlet state. This photo-bleaching is a detectable error, so it does not affect the fidelity of entanglement generation or measurement described in Chapter 5. However, it can increase the time required for these operations. Fluorescence correlation experiments are consistent with assigning a metastable singlet structure to the shelving state, which is coupled strongly to the $M_s = \pm 1$ excited states but only weakly to the $M_s = 0$ excited state (see Figure 5.2), [84]. We need to account for the possibility that our NV center bleaches during entanglement generation, requiring us to start over. During each attempt we resonantly excite the $M_s = 0$ transition with some probability P_{em} (see

Eq. 5.13). To quantify the population lost to $|W\rangle$ we will consider a model where the $M_s = \pm 1$ excited states decay to the shelving state at rate Γ_S. The oscillator strength for the $M_s = \pm 1$ optical transitions are unknown, so we will assume that the Rabi frequencies on the $M_s = \pm 1$ transitions are Ω'.

During one attempt at entanglement generation, the probability to end up in the shelving state is

$$P_W \sim \Gamma_S \frac{\Omega'^2}{\Delta_1^2} t_0, \tag{C.1}$$

where Δ_1 is the detuning from the $M_s = \pm 1$ optical transition. (The excited state energies are strongly inhomogeneously broadened, so Δ_1 is not precisely known; this detuning should be controllable using strain or applied electric fields.) On average, a large number of attempts $\sim 4/P_{\rm em}\epsilon$ are required for successful entanglement generation. Consequently the total probability for the system to end up in the shelving state during entanglement generation is

$$P_W \sim 4\Gamma_S \frac{\Omega'^2}{\Delta_1^2} \frac{\gamma}{\Omega^2 \epsilon} \sim 4 \frac{\Gamma_S \gamma}{\Delta_1^2 \epsilon} \frac{\mu'^2}{\mu^2}, \tag{C.2}$$

where $\mu(\mu')$ is the oscillator strength for the $M_s = 0(\pm 1)$ transition. The precise values of these parameters are unknown, but we can estimate their order of magnitude: $\Gamma_S \sim 1 - 10$ MHz, $\gamma + \Gamma \sim 100$ MHz, $\Delta_1 \sim 1$ GHz, $\mu' \sim \mu$, yielding

$$P_W \sim \frac{4(10^{-3} - 10^{-4})}{\epsilon}. \tag{C.3}$$

If this error rate is too large, we can also check for photo-bleaching at intervals during the entanglement procedure.

The shelving state poses a similar problem during measurement. In this case, the $M_s = 0$ transition is strongly illuminated so that at least one photon reaches the

detectors: $P_{\rm em} \sim 1/\epsilon$. Under the same illumination, any population in $|1\rangle$ will end up in the shelving state with probability

$$P_W \sim P_{\rm ex}\frac{\Gamma_S\gamma}{\Delta_1^2}\frac{\mu'^2}{\mu^2} \sim \frac{\Gamma_S\gamma}{\Delta_1^2\epsilon}\frac{\mu'^2}{\mu^2} \sim \frac{(10^{-3}-10^{-4})}{\epsilon}, \tag{C.4}$$

Note that the measurement fidelity is unaffected by photo-bleaching if we verify that the center is optically active by observing fluorescence either directly from the $|0\rangle$ state or after applying a multiplexed ESR pulse to the $|1\rangle$ states. Ultimately, in this model the only effect of the shelving state is to reduce the success rate for entanglement generation and measurement by of order a few percent. Finally, we should note that the effect of the shelving state on the nuclear spin state is currently not known, and could potentially complicate the sequence of operations necessary upon detection of a shelving event.

Bibliography

[1] P.T.H. Fisk. Trapped-ion and trapped-atom microwave frequency standards. *Rep. Prog. Phys.*, 60:761, 1997.

[2] D. Meschede and A. Rauschenbeutel. Atom interferometry. *Physica Scripta*, 74:C15, 2006.

[3] D.P. DiVincenzo. Quantum computation. *Science*, 270:255, 1995.

[4] D. Bouwmeester, A. K. Ekert, and A. Zeilinger (Eds.). *The physics of quantum information: quantum cryptography, quantum teleportation, quantum computation*. Springer-Verlag, NY, 2000.

[5] M. O. Scully and M. S. Zubairy. *Quantum Optics*. Cambridge University Press, Cambridge, UK, 1997.

[6] P. Meystre and M. Sargent. *Elements of Quantum Optics, 3rd Ed.* Springer, NY, 1999.

[7] C. Langer *et al.* Long-lived qubit memory using atomic ions. *Phys. Rev. Lett.*, 95:060502, 2005.

[8] W.D. Phillips. Laser cooling and trapping of neutral atoms. *Rev. Mod. Phys.*, 70:721, 1998.

[9] S. Chu. The manipulation of neutral atoms. *Rev. Mod. Phys.*, 70:685, 1998.

[10] C.N. Cohen-Tannoudji. Manipulating atoms with photons. *Rev. Mod. Phys.*, 70:707, 1998.

[11] P.S. Jessen *et al.* Observation of quantized motion of rb atoms in an optical-field. *Phys. Rev. Lett.*, 69:49, 1992.

[12] C. Monroe *et al.* Resolved-side-band raman cooling of a bound atom to the 3d zero-point energy. *Phys. Rev. Lett.*, 75:4011, 1995.

[13] D.J. Wineland *et al.* Quantum information processing with trapped ions. *Phil. Trans. Royal Soc. London A*, 361:1349, 2003.

[14] A. Sørensen and K. Mølmer. Quantum computation with ions in thermal motion. *Phys. Rev. Lett.*, 82:1971, 1999.

[15] D. Liebfried *et al.* Experimental demonstration of a robust, high-fidelity geometric two ion-qubit phase gate. *Nature*, 422:412, 2003.

[16] D. Phillips, M. Fleischhauer, A. Mair, R. Waslworth, and M. D. Lukin. Storage of light in atomic vapor. *Phys. Rev. Lett.*, 86:783, 2001.

[17] J. Chiaverini *et al.* Implementation of the semiclassical quantum fourier transform in a scalable system. *Science*, 308:997, 2005.

[18] M.D. Barrett *et al.* Deterministic quantum teleportation of atomic qubits. *Nature*, 429:737, 2004.

[19] M. Riebe *et al.* Deterministic quantum teleportation with atoms. *Nature*, 429:734, 2004.

[20] H. Haffner *et al.* Scalable multiparticle entanglement of trapped ions. *Nature*, 438:643, 2005.

[21] D. Leibfried *et al.* . Creation of a six-atom 'schrodinger cat' state. *Nature*, 438:639, 2005.

[22] D. Jaksch, J.I. Cirac, P. Zoller, S.L. Rolston, R. Côté, and M.D. Lukin. Fast quantum gates for neutral atoms. *Phys. Rev. Lett.*, 85:2208, 2000.

[23] M.D. Lukin, M. Fleischhauer, R. Côté, L.M. Duan, D.Jaksch, J.I. Cirac, and P. Zoller. Dipole blockade and quantum information processing in mesoscopic atomic ensembles. *Phys. Rev. Lett.*, 87:037901, 2001.

[24] J. I. Cirac, P. Zoller, H. Mabuchi, and H. J. Kimble. Quantum state transfer and entanglement distribution among distant nodes in a quantum network. *Phys. Rev. Lett.*, 78:3221, 1997.

[25] J. McKeever *et al.* Deterministic generation of single photons from one atom trapped in a cavity. *Science*, 303:1992, 2004.

[26] T. Aoki *et al.* Observation of strong coupling between one atom and a monolithic microresonator. *Nature*, 443:671, 2006.

[27] J.M. Raimond, M. Brune, and S. Haroche. Colloquium: Manipulating quantum entanglement with atoms and photons in a cavity. *Rev. Mod. Phys.*, 73:565, 2001.

[28] H. Walther, B.T.H. Varcoe, B.G. Englert, and T. Becker. Cavity quantum electrodynamics. *Rep. Prog. Phys*, 69:1325, 2006.

[29] M. D. Lukin and M. Fleischhauer. Dark-state polaritons in electromagnetically induced transparency. *Phys. Rev. Lett.*, 84:5094, 2000.

[30] M. Eisaman *et al.* Electromagnetically induced transparency with tunable single-photon pulses. *Nature*, 438:837, 2005.

[31] C. Cabrillo, J.I. Cirac, P. Garcia-Fernandez, and P. Zoller. Creation of entangled states of distant atoms by interference. *Phys. Rev. A*, 59:1025, 1999.

[32] L. M. Duan, M. D. Lukin, J. I. Cirac, and P. Zoller. Long-distance quantum communication with atomic ensembles and linear optics. *Nature*, 414:413, 2001.

[33] C.W. Chou *et al.* Measurement-induced entanglement for excitation stored in remote atomic ensembles. *Nature*, 438:828, 2005.

[34] B.B. Blinov *et al.* Observation of entanglement between a single trapped atom and a single photon. *Nature*, 428:153, 2004.

[35] M.J. Madsen *et al.* . Ultrafast coherent excitation of a trapped ion qubit for fast gates and photon frequency qubits. *Phys. Rev. Lett.*, 97:040505, 2006.

[36] P. Maunz *et al.* Quantum interference of photon pairs from two trapped atomic ions. *eprint: quant-ph/0608047*, 2006.

[37] D. Gottesman and I.L. Chuang. Demonstrating the viability of universal quantum computation using teleportation and single-qubit operations. *Nature*, 402:390, 2006.

[38] L.M. Duan, B.B. Blinov, D.L. Moehring, and C. Monroe. Scalable trapped ion quantum computation with a probabilistic ion-photon mapping. *Quant. Inf. Comp.*, 4:165, 2004.

[39] L.M. Duan *et al.* Probabilistic quantum gates between remote atoms through interference of optical frequency qubits. *Phys. Rev. A*, 73:062324, 2006.

[40] W.G. van der Wiel *et al.* Electron transport through double quantum dots. *Rev. Mod. Phys.*, 75:1, 2003.

[41] Y.K. Kato, R.C. Myers, D.C. Driscoll, A.C. Gossard, J. Levy, and D.D. Awschalom. Gigahertz electron spin manipulation using voltage-controlled g-tensor modulation. *Science*, 299:1201, 2003.

[42] C. Santori *et al.* Indistinguishable photons from a single-photon device. *Nature*, 419:594, 2002.

[43] A. Wallraff *et al.* Strong coupling of a single photon to a superconducting qubit using circuit quantum electrodynamics. *Nature*, 431:162, 2004.

[44] D. Gammon *et al.* Electron and nuclear spin interactions in the optical spectra of single gaas quantum dots. *Phys. Rev. Lett.*, 86:5176, 2001.

[45] A. Badolato *et al.* Deterministic coupling of single quantum dots to single nanocavity modes. *Science*, 308:1158, 2006.

[46] T. Hayashi, T. Fujisawa, H.D. Cheong, Y.H. Jeong, and Y. Hirayama. Coherent manipulation of electronic states in a double quantum dot. *Phys. Rev. Lett.*, 91:226804, 2003.

[47] J. R. Petta *et al.* Coherent manipulation of coupled electron spins in semiconductor quantum dots. *Science*, 309:2180, 2005.

[48] T. Gaebel *et al.* Room-temperature coherent coupling of single spins in diamond. *Nature Physics*, 2:408, 2006.

[49] B.E. Kane. A silicon-based nuclear spin quantum computer. *Nature*, 393:133, 1998.

[50] T.D. Ladd *et al.* Coherence time of decoupled nuclear spins in silicon. *Phys. Rev. B*, 71:014401, 2005.

[51] J. M. Taylor, C. M. Marcus, and M. D. Lukin. Long-lived memory for mesoscopic quantum bits. *Phys. Rev. Lett.*, 90:206803, 2003.

[52] J. Schliemann, A. Khaetskii, and D. Loss. Electron spin dynamics in quantum dots and related nanostructures due to hypertine interaction with nuclei. *J. Phys.: Cond. Matter*, 15:R1809, 2003.

[53] W. Yao, Renbao Liu, and L. J. Sham. Theory of electron spin decoherence by interacting nuclear spins in a quantum dot. *e-print:cond-mat/0508441*, 2005.

[54] N. Shenvi, R. de Sousa, and K. B. Whaley. Universal scaling of hyperfine-induced electron spin echo decay. *Phys. Rev. B*, 71:224411, 2005.

[55] N. Gisin, G. Riborty, W. Tittel, and H. Zbinden. Quantum cryptography. *Rev. Mod. Phys*, 74:145, 2002.

[56] H. J. Briegel, W. Dur, J. I. Cirac, and P. Zoller. Quantum repeaters: The role of imperfect local operations in quantum communication. *Phys. Rev. Lett.*, 81:5932, 1998.

[57] W. Dur, H. J. Briegel, J. I. Cirac, and P. Zoller. Quantum repeaters based on entanglement purification. *Phys. Rev. A.*, 59:169, 1999.

[58] D. Loss and D. P. DiVincenzo. Quantum computation with quantum dots. *Phys. Rev. A*, 57:120, 1998.

[59] A. Andre *et al.* A coherent all-electrical interface between polar molecules and mesoscopic superconducting resonators. *Nature Physics*, 2:636, 2006.

[60] A.S. Sorensen, C.H. van der Wal, L. Childress, and M.D. Lukin. Capacitive coupling of atomic systems to mesoscopic conductors. *Phys. Rev. Lett.*, 92:063601, 2004.

[61] A. Lenef and S.C. Rand. Electronic structure of the n-v center in diamond: Theory. *Phys. Rev. B*, 53:13441, 1996.

[62] J.P.D Martin. Fine structure of excited e-3 state in nitrogen-vacancy centre of diamond. *J. Lumin.*, 81:237, 1999.

[63] N.B. Manson, J.P. Harrison, and M.J. Sellars. The nitrogen-vacancy center in diamond re-visited. *eprint:cond-mat/0601360*, 2006.

[64] T. Gaebel *et al.* Photochromism in single nitrogen-vacancy defect in diamond. *Appl. Phys. B-Lasers and Optics*, 82:243, 2006.

[65] Y. Mita. Change of absorption spectra of type-ib diamond with heavy neutron irradiation. *Phys. Rev. B*, 53:11360, 1996.

[66] J.P. Goss *et al.* Comment on "electronic structure of the n-v center in diamond: Theory". *Phys. Rev. B*, 56:16031, 1997.

[67] G. Davies and M.F. Hamer. Optical studies of the 1.945 ev vibronic band in diamond. *Proc. Royal. Soc. London A*, 348:285, 1976.

[68] N.R.S Reddy, N.B. Manson, and E.R. Krausz. 2-laser spectral hole burning in a color center in diamond. *J. Lumin.*, 38:46, 1987.

[69] D.A Redman, S. Brown, R.H. Sands, and S.C. Rand. Spin dynamics and electronic states of nv centers in diamond by epr and four-wave-mixing spectroscopy. *Phys. Rev. Lett.*, 67:3420, 1991.

[70] J.H.H Loubser and J.A. van Wyk. Electron spin resonance in the study of diamond. *Rep. Prog. Phys.*, 41:1201, 1978.

[71] E. van Oort, N.B. Manson, and M. Glasbeek. Optically detected spin coherence of the diamond n-v centre in its triplet ground state. *J. Phys. C: Solid State Phys.*, 21:4385, 1988.

[72] N.B. Manson, X.-F. He, and P.T.H. Fisk. Raman heterodyne detected electron-nuclear-double-resonance measurements of the nitrogen-vacancy center in diamond. *Opt. Lett.*, 15:1094, 1990.

[73] A. Drabenstedt *et. al.* Low-temperature microscopy and spectroscopy on single defect centers in diamond. *Phys. Rev. B*, 60:11503, 1999.

[74] F. Jelezko *et al.* Spectroscopy of single n-v centers in diamond. *Single Mol.*, 2:255, 2001.

[75] A. Gruber *et al.* Scanning confocal optical microscopy and magnetic resonance on single defect centers. *Science*, 276:2012, 1997.

[76] C. Kurtsiefer, S. Mayer, P. Zarda, and H. Weinfurter. Stable solid-state source of single photons. *Phys. Rev. Lett.*, 85:290, 2000.

[77] A. Beveratos *et al.* Nonclassical radiation from diamond nanocrystals. *Phys. Rev. A*, 64:061802(R), 2001.

[78] Ph. Tamarat *et al.* Stark shift control of single optical centers in diamond. *Phys. Rev. Lett.*, 97:083002, 2006.

[79] F. Jelezko *et al.* Observation of coherent oscillation of a single nuclear spin and realization of a two-qubit conditional quantum gate. *Phys. Rev. Lett.*, 93:130501, 2004.

[80] R. J. Epstein, F. Mendoza, Y. K. Kato, and D. D. Awschalom. Anisotropic interactions of a single spin and dark-spin spectroscopy in diamond. *Nature Physics*, 1:94, 2005.

[81] X.-F. He, N.B. Manson, and P.T.H. Fisk. Paramagnetic resonance of photoexcited n-v defects in diamond. i, level anticrossing in the ^{3}a ground state. *Phys. Rev. B*, 47:8809, 1993.

[82] A. Beveratos, R. Brouri, J.P. Poizat, and P. Grangier. Bunching and antibunching from single nv color centers in diamond. *eprint: quant-ph/0010044*, 2000.

[83] A.P. Nizotzev, S.Y. Kilin, C. Tietz, F. Jelezko, and J. Wrachtrup. Modeling fluorescence of single nitrogen-vacancy defect centers in diamond. *Physica B-Cond. Matt.*, 308:608, 2001.

[84] A.P. Nizotzev *et al.* Spin-selective low temperature spectroscopy on single molecules with a triplet-triplet optical transition: Application to the nv defect center in diamond. *Optics and Spectroscopy*, 94:848, 2003.

[85] A. Beveratos *et al.* Single photon quantum cryptography. *Phys. Rev. Lett.*, 89:187901, 2002.

[86] R. Alleaume, F. Treussart, G. Messin, Y. Demeige, J.F. Roch andA. Beveratos, R. Brouri, J.P. Poizat, and P. Grangier. Experimental open air quantum key distribution with a single photon source. *eprint: quant-ph/0402110*, 2004.

[87] F. Jelezko *et al.* Single spin states in a defect center resolved by optical spectroscopy. *App. Phys. Lett.*, 81:2160, 2002.

[88] A.T. Collins, M.F. Thomaz, and M.I.B. Jorge. Luminescence decay time of the 1.945 ev centre in type ib diamond. *J. Phys. C.: Solid State Phys.*, 16:2177, 1983.

[89] J.H.H Loubser and J.A. van Wyk. *Diamond Research*, 1:11, 1977.

[90] J. Harrison, M.J. Sellars, and N.B. Manson. Optical spin polarisation of the n-v centre in diamond. *J. Lumin.*, 107:245, 2004.

[91] F. Jelezko, T. Gaebel, I. Popa, A. Gruber, and J. Wrachtrup. Observation of coherent oscillations in a single electron spin. *Phys. Rev. Lett.*, 92:076401, 2004.

[92] J. Wrachtrup and F. Jelezko. Quantum information processing in diamond. *J. Phys.: Condens. Matter*, 18:S807, 2006.

[93] C. Santori *et al.* Coherent population trapping in diamond n-v centers at zero magnetic field. *eprint:cond-mat/0602573*, 2006.

[94] C. Santori *et al.* Coherent population trapping with a single spin in diamond. *eprint: quant-ph/0607147*, 2006.

[95] E. van Oort, P. Stroomer, and M. Glasbeek. Low-field optically detected magnetic resonance of a coupled triplet-doublet defect pair in diamond. *Phys. Rev. B*, 42:8605, 1990.

[96] L. Childress, J.M. Taylor, A.S. Sørensen, and M.D. Lukin. Fault-tolerant quantum communication based on solid-state photon emitters. *Phys. Rev. Lett.*, 96:070504, 2006.

[97] J.R. Rabeau *et al.* Implantation of labelled single nitrogen vacancy centers in diamond using n-15. *App. Phys. Lett.*, 88:023113, 2006.

[98] F.T. Charnock and T.A Kennedy. Combined optical and microwave approach for performing quantum spin operations on the nitrogen-vacancy center in diamond. *Phys. Rev. B*, 64:041201(R), 2001.

[99] X.-F. He, N.B. Manson, and P.T.H. Fisk. Paramagnetic resonance of photoexcited n-v defects in diamond. ii, hyperfine interaction with the n-14 nucleus. *Phys. Rev. B*, 47:8816, 1993.

[100] M. Gaudin. *La function d'Onde de Bethe*. Masson, Paris, 1983.

[101] R.G. Clark *et al.* Progress in silicon-based quantum computing. *Phil. Trans. Royal Soc. A*, 361:1451, 2003.

[102] L. Childress, J.M. Taylor, A.S. Sørensen, and M.D. Lukin. Fault-tolerant quantum repeaters with minimal physical resources and implementations based on single-photon emitters. *Phys. Rev. A*, 72:052330, 2005.

[103] P. van Loock *et al.* Hybrid quantum repeater using bright coherent light. *Phys. Rev. Lett.*, 96:240501, 2006.

[104] A. Schweiger and G. Jeschke. *Principles of pulse electron paramagnetic resonance*. Oxford University Press, Oxford, UK, 2001.

[105] E.L. Hahn. Spin echoes. *Phys. Rev.*, 80:580, 1950.

[106] C.P. Slichter. *Principles of magnetic resonance*. Springer-Verlag, NY, 1990.

[107] F. Jelezko and J. Wrachtrup. Read-out of single spins by optical spectroscopy. *J. Phys.: Condens. Matter*, 16:R1089, 2004.

[108] L. G. Rowan, E. L. Hahn, and W. B. Mims. Electron-spin-echo envelope modulation. *Phys. Rev.*, 137:A61, 1965.

[109] L. Childress and M.V. Gurudev Dutt *et al. Published online September 14 2006; 10.1126/science.1131871 (Science Express Reports)*, 2006. Supplementary online material for "Coherent Dynamics of Coupled Electron and Nuclear Spin Qubits in Diamond".

[110] Y. Makhlin, G. Schon, and A. Shnirman. Quantum-state engineering with josephson-junction devices. *Rev. Mod. Phys.*, 73:357, 2001.

[111] F. H. L. Koppens *et al.* Control and detection of singlet-triplet mixing in a random nuclear field. *Science*, 309:1346, 2005.

[112] M. Atature *et al.* Quantum-dot spin-state preparation with near-unity fidelity. *Science*, 312:551, 2006.

[113] L. Childress and M.V. Gurudev Dutt *et al.* Coherent dynamics of coupled electron and nuclear spin qubits in diamond. *Published online September 14 2006; 10.1126/science.1131871 (Science Express Reports)*, 2006.

[114] G. Brassard, N. Lutkenhaus, T. More, and B.C. Sanders. Limitations on practical quantum cryptography. *Phys. Rev. Lett.*, 85:1330, 2000.

[115] M. Zukowski *et al.* "event-ready-detectors" bell experiment via entanglement swapping. *Phys. Rev. Lett.*, 71:4287, 1993.

[116] C.H. Bennett *et al.* Teleporting an unknown quantum state via dual classical and einstein-podolsky-rosen channels. *Phys. Rev. Lett.*, 70:1895, 1993.

[117] D. Bouwmeester *et al.* Experimental quantum teleportation. *Nature*, 390:575, 1997.

[118] A. Ekert. Quantum cryptography based on bell's theorem. *Phys. Rev. Lett.*, 67:661, 1991.

[119] C. Bennett *et al.* Purification of noisy entanglement and faithful teleportation via noisy channels. *Phys. Rev. Lett.*, 76:722, 1996.

[120] D. Deutsch *et al.* Quantum privacy amplification and the security of quantum cryptography over noisy channels. *Phys. Rev. Lett.*, 77:2818, 1996.

[121] S. J. van Enk, J. I. Cirac, and P. Zoller. Photonic channels for quantum communication. *Science*, 279:205, 1998.

[122] S. Bose *et al.* Proposal for teleportation of an atomic state via cavity decay. *Phys. Rev. Lett.*, 83:5158, 1999.

[123] J. Ye, D. W. Vernooy, and H. J. Kimble. Trapping of single atoms in cavity qed. *Phys. Rev. Lett.*, 83:4987, 1999.

[124] P. Michler *et al.* A quantum dot single-photon turnstile device. *Science*, 290:2282, 2000.

[125] D.E. Browne, M.B. Plenio, and S.F. Huelga. Robust creation of entanglement between ions in spatially separate cavities. *Phys. Rev. Lett.*, 91:067901, 2003.

[126] J. Ye *et al.* Delivery of high-stability optical and microwave frequency standards over an optical fiber network. *J. Opt. Soc. Am. B*, 20:1459, 2003.

[127] K.W. Holman, D.D. Hudson, J. Ye, and D.J. Jones. Remote transfer of a high-stability and ultralow-jitter timing signal. *Opt. Lett.*, 30:1225, 2005.

[128] A. Muller *et al.* "plug and play" systems for quantum cryptography". *Appl. Phys. Lett.*, 70:793, 1997.

[129] C. Simon and W.T.M. Irvine. Robust long-distance entanglement and a loophole-free bell test with ions and photons. *Phys. Rev. Lett.*, 91:110405, 2003.

[130] A. Sørensen and K. Mølmer. Error-free quantum communication through noisy channels. *Phys. Rev. A*, 58:2745, 1998.

[131] S.J. van Enk, J.I. Cirac, and P. Zoller. Ideal quantum communication over noisy channels: a quantum optical implementation. *Phys. Rev. Lett.*, 78:4293, 1997.

[132] K. Mølmer, Y. Castin, and J. Dalibard. Monte-carlo wave-function method in quantum optics. *J. Opt. Soc. Am. B*, 10:524, 1993.

[133] A.S. Sørensen and K. Mølmer. Probabilistic generation of entanglement in optical cavities. *Phys. Rev. Lett.*, 90:127903, 2003.

[134] S.D. Barrett and P. Kok. Efficient high-fidelity quantum computation using matter qubits and linear optics. *Phys. Rev. A*, 71:060310(R), 2005.

[135] W. Dur. Quantum communication over long distances using quantum repeaters. *Masters Thesis*, 1998.

[136] T. Gaebel *et al.* Stable single-photon source in the near infrared. *New Journal of Physics*, 6:98, 2004.

[137] S. Kilin. Private communication.

[138] T.A. Kennedy, J.S. Colton, J.E. Butler, R.C. Linares, and P.J. Doering. Long coherence times at 300k for nitrogen-vacancy center spins in diamond grown by chemical vapor deposition. *App. Phys. Lett.*, 83:4190, 2003.

[139] A. Imamoglu *et al.* Quantum information processing using quantum dot spins and cavity qed. *Phys. Rev. Lett.*, 83:4204, 1999.

[140] E. Pazy, E. Biolatti, T. Calarco, I. D'Amico, P. Zanardi, F. Rossi, and P. Zoller. Spin-based optical quantum gates via Pauli blocking in semiconductor quantum dots. *Europhys. Lett.*, 62:175, 2003.

[141] A. S. Bracker *et al.* Optical pumping of electronic and nuclear spin in single charge-tunable quantum dots. *e-print:cond-mat/0408466*, 2004.

[142] V.N. Golovach, A. Khaetskii, and D. Loss. Phonon-induced decay of the electron spin in quantum dots. *eprint: cond-mat/0310655*, 2003.

[143] C. Ramanathan *et al.* Nmr quantum information processing. *eprint: quant-ph/0408166*, 2004.

[144] J. M. Taylor *et al.* Quantum information processing using localized ensembles of nuclear spins. *e-print: cond-mat/0407640*, 2004.

[145] A. Kiraz *et al.* Photon correlation spectroscopy of a single quantum dot. *Phys. Rev. B*, 65:161303(R), 2002.

[146] J. M. Taylor, A. Imamoglu, and M.D. Lukin. Controlling a mesoscopic spin environment by quantum bit manipulation. *Phys. Rev. Lett.*, 91:246802, 2003.

[147] A. Imamoglu *et al.* Optical pumping of quantum-dot nuclear spins. *Phys. Rev. Lett.*, 91:017402, 2003.

[148] B. DeMarco *et al.* Experimental demonstration of a controlled-not wave-packet gate. *Phys. Rev. Lett.*, 89:267901, 2002.

[149] A. Rauschenbeutel *et al.* Coherent operation of a tunable quantum phase gate in cavity qed. *Phys. Rev. Lett.*, 83:5166, 1999.

[150] D. Vion *et al.* Manipulating the quantum state of an electrical circuit. *Science*, 296:886, 2002.

[151] Y. Yu *et al.* Coherent temporal oscillations of macroscopic quantum states in a josephson junction. *Science*, 296:889, 2002.

[152] Y. Nakamura *et al.* Coherent control of macroscopic quantum states in a single-cooper-pair box. *Nature*, 398:786, 1999.

[153] V.N. Golovach and D. Loss. Electron spins in artificial atoms and molecules for quantum computing. *Semiconductor Sci. Tech.*, 17:355, 2002. and references therein.

[154] B.A. Mazin *et al. AIP Conf. Proc.*, 605:309, 2001.

[155] B.A. Mazin *et al. Proc. SPIE*, 4849:283, 2002.

[156] A. Rauschenbeutel *et al.* Step-by-step engineered multiparticle entanglement. *Science*, 288:2024, 2000.

[157] G. Nogues *et al.* Seeing a single photon without destroying it. *Nature*, 400:239, 1999.

[158] B.T.H. Varcoe *et al.* Preparing pure photon number states of the radiation field. *Nature*, 403:743, 2000.

[159] S. Brattke, B.T.H. Varcoe, and H. Walther. Generation of photon number states on demand via cavity quantum electrodynamics. *Phys. Rev. Lett.*, 86:3534, 2001.

[160] O. Buisson and F.W.J. Hekking. Entangled states in a josephson charge qubit coupled to a superconducting resonator. *eprint: cond-mat/0008275*, 2000.

[161] A. Yu Smirnov and A.M. Zagoskin. Quantum entanglement of flux qubits via a resonator. *eprint: cond-mat/0207214*, 2002.

[162] F. Plastina and G. Falci. Communicating josephson qubits. *eprint: cond-mat/0206586*, 2002.

[163] A. Blais, A. Maassen van den Brink, and A.M. Zagoskin. Tunable coupling of superconducting qubits. *Phys. Rev. Lett.*, 90:127901, 2003.

[164] A. Blais, R.S. Huang, A. Wallraff, S.M. Girvin, and R.J. Schoelkopf. Cavity quantum electrodynamics for superconducting electrical circuits: An architecture for quantum computation. *Phys. Rev. A*, 69:062320, 2004.

[165] D.I. Schuster *et al.* ac stark shift and dephasing of a superconducting qubit strongly coupled to a cavity field. *Phys. Rev. Lett.*, 94:123602, 2005.

[166] A. Wallraff *et al.* Approaching unit visibility for control of a superconducting qubit with dispersive readout. *Phys. Rev. Lett.*, 95:060501, 2005.

[167] P. Rabl *et al.* Hybrid quantum processors: Molecular ensembles as quantum memory for solid state circuits. *Phys. Rev. Lett.*, 97:033003, 2006.

[168] K. Bergmann, H. Theuer, and B.W. Shore. Coherent population transfer among quantum states of atoms and molecules. *Rev. Mod. Phys.*, 70:1003, 1998.

[169] T. Pellizzari, S. A. Gardiner, J. I. Cirac, and P. Zoller. Decoherence, continuous observation, and quantum computing: A cavity qed model. *Phys. Rev. Lett.*, 75:3788, 1995.

[170] I. Chan, R.M. Westervelt, K.D. Maranowski, and A.C. Gossard. Strongly capacitively coupled quantum dots. *Appl. Phys. Lett.*, 80:1818, 2002.

[171] T. Fujisawa *et al.* Allowed and forbidden transitions in artificial hydrogen and helium atoms. *Nature*, 419:278, 2002.

[172] T.H. Stoof and Yu.V. Nazarov. Time-dependent resonant tunneling via two discrete states. *Phys. Rev. B*, 53:1050, 1996.

[173] R. Deblock, E. Onac, L. Gurevich, and L.P. Kouwenhoven. Detection of quantum noise from an electrically driven two-level system. *Science*, 301:203, 2003.

[174] L.M.K. Vandersypen, R. Hanson, L.H. Willems van Beveren, J.M. Elzerman, J.S. Greidanus, S. De Franceschi, and L.P. Kouwenhoven. Quantum computing with electron spins in quantum dots. *eprint: quant-ph/0207059*, 2002. published in "Quantum Computing and Quantum Bits in Mesoscopic Systems", Kluwer Academic Plenum Publishers.

[175] G. Salis *et al.* Electrical control of spin coherence in semiconductor nanostructures. *Nature*, 414:6864, 2001.

[176] R. Lang, M.O. Scully, and Jr. W.E. Lamb. Why is laser line so narrow questionable - theory of single-quasimode laser operation. *Phys. Rev. A*, 7:1788, 1973.

[177] J. Gea-Banacloche *et al.* Treatment of the spectrum of squeezing based on the modes of the universe. i. theory and a physical picture. *Phys. Rev. A*, 41:369, 2000.

[178] Y. Onodera T. Inui, Y. Tanabe. *Group Theory and its Applications in Physics.* Springer-Verlag, NY, 1976.